Alma Mater Studiorum - Università di Bologna

DOTTORATO DI RICERCA IN

CHIMICA

Ciclo 33

Settore Concorsuale: 03/A2 - MODELLI E METODOLOGIE PER LE SCIENZE CHIMICHE

Settore Scientifico Disciplinare: CHIM/02 - CHIMICA FISICA

NANOCARBON-SUPPORTED ELECTROCATALYSTS FOR THE ALKALINE WATER SPLITTING AND FUEL CELLS

Presentata da: Meng Liu

Coordinatore Dottorato

Domenica Tonelli

Supervisore

Francesco Paolucci

Co-supervisore

Giovanni Valenti

Esame finale anno 2021

Abstract

Electrocatalysts play a significant role in the processes of electrochemical energy conversion. This thesis focuses on the preparation of carbon-supported nanomaterials and their application as electrocatalysts for alkaline water electrocatalysis and fuel cell. A general synthetic route was developed, i.e., species intercalate into carbon layers of graphite forming graphite intercalation compound, followed by dispersion producing graphenide solution, which then as reduction agent reacts with different metal sources generating the final materials.

The first metal precursor used was non-noble metal iron salt, which generated iron (oxide) nanoparticles finely dispersed on carbon layers in the final composite materials. Meanwhile, graphite starting materials differing in carbon layer size were utilized, which would diversify corresponding graphenide solutions, and further produce various nanomaterials. The characterization results showed that iron (oxide) nanoparticles varying in size were obtained, and the size was determined by the starting graphite material. It was found that they were electrocatalytically active for oxygen reactions. In particular, the one with small iron (oxide) nanoparticles showed excellent electrocatalytic activity for both oxygen reduction reaction (ORR) and oxygen evolution reaction (OER).

Afterwards, the metal precursor was tuned from non-noble metal salt to noble metal salt. It was confirmed that carbon-supported Rh, Pt, and RhPt (oxide) nanoparticle composite materials were also successfully obtained from the reaction between graphenide solution and corresponding noble metal precursor. The electrochemical measurements showed that the prepared noble metal-based nanomaterials were quite effective for hydrogen evolution reaction (HER) electrocatalysis, and the Rh sample could also display excellent electrocatalytic property towards OER.

Moreover, by this synthetic approach carbon-supported noble metal Pt and non-noble metal nickel (Ni)

composite material was also prepared. Therefore, the utilization efficiency of noble metal could be improved. The prepared NiPt sample displayed a property close to benchmark HER electrocatalyst.

Table of contents

Chapter 1 Introduction

Developing a sustainable energy system meanwhile protecting our environment is one of the most crucial challenges faced by human beings today.[1] According to the International Energy Agency, the majority of global energy in 2018 was provided by fossil fuels, e.g., 31.6% oil, 26.9% coal, and 22.8% natural gas (Figure 1). However, fossil fuels are non-renewable, and the consumption of fossil fuels emits carbon dioxide into the atmosphere, causing environmental issues. Therefore, it is intensely expected to reduce the reliance on fossil fuels, and turn our attention to renewable and clean energy sources, such as solar, wind, tidal, and geothermal. The fact is that these alternatives are generally dispersed and inherently intermittent.[2] Thus, to make the best use of them, highly efficient energy storage and conversion systems are needed.

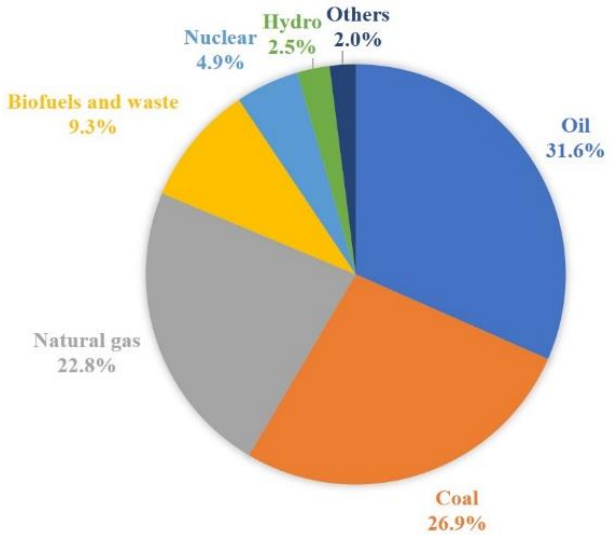

Figure 1 Global share of total energy supply by source, 2018. The data is from the International Energy Agency, Key World Energy Statistics 2020.

Hydrogen (H_2) is an excellent energy carrier and a promising candidate for future low-carbon energy sources. However, the majority of H_2 currently is produced by steam reforming of fossil resources, which suffers from low conversion rate, and also is not environment-friendly. Instead, water

electrolysis is an efficient and clean technique for H_2 production. Therefore, a sustainable energy conversion system is using excess electricity from renewable energy sources to produce H_2 by water electrolysis, and regenerating electricity by H_2 fuel cells (Figure 2).

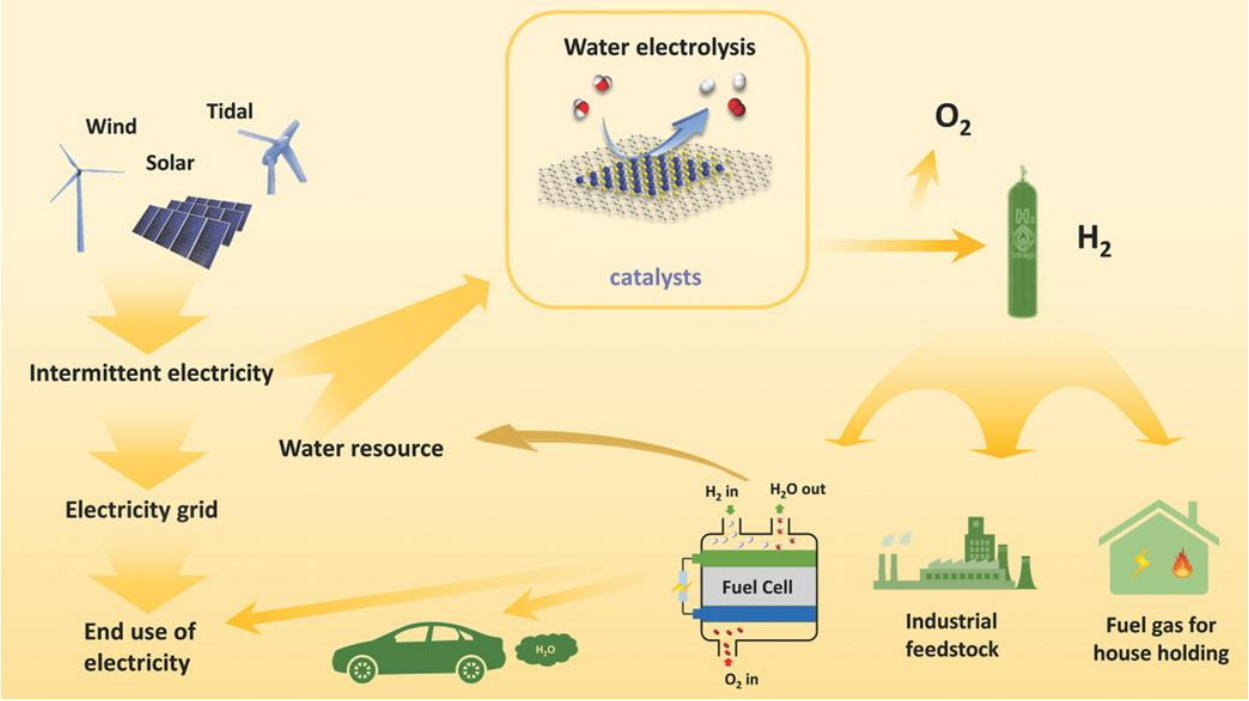

Figure 2 A sustainable pathway for the production and utilization of hydrogen energy. Reprinted with permission from reference [3]. Copyright © 2018 WILEY-VCH Verlag GmbH & Co. KGaA, Weinheim

1.1 Water electrolysis

Water can be dissociated into its elemental components, i.e., hydrogen and oxygen, according to:

$$H_2O\ (l) \rightarrow H_2\ (g) + 1/2O_2\ (g) \qquad \Delta G = +237.2\ kJ\ mol^{-1}\ (25\ ^oC,\ 1\ atm)$$

As the Gibbs free energy change (ΔG) of water dissociation is positive, the reaction is nonspontaneous at standard conditions of temperature and pressure.[4] However, it can be driven by providing external energy, for example electricity, and the corresponding process is known as water electrolysis or electrochemical water splitting.

Depending on the electrolyte used, water electrolysis generally can be divided into three types: alkaline water electrolysis (AWE), polymer electrolyte membrane water electrolysis (PEMWE), and solid oxide electrolysis (SOE).[5,6] A comparation of them was shown in Figure 3.

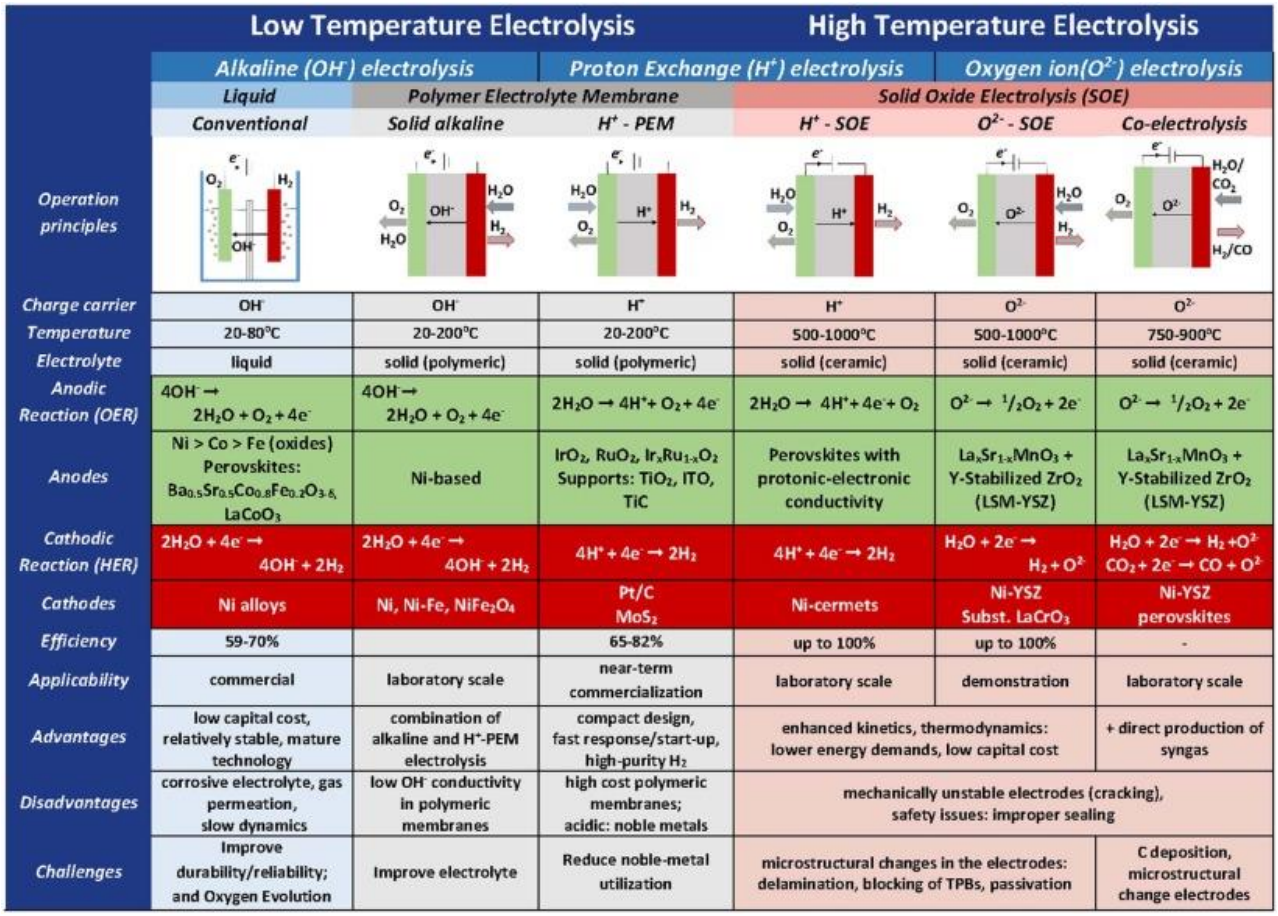

Figure 3 The typical characteristics of the main electrolysis technologies. Reprinted with permission from reference [7]. Copyright © 2016 Published by Elsevier Ltd.

SOE typically is performed at temperatures above 500 °C with water in the form of steam, and utilizes O^{2-} conductors. AWE and PEMWE operate at significantly lower temperature (typically below 100 °C, where water is liquid). For AWE, the two electrodes are immersed in a liquid alkaline electrolyte (commonly potassium hydroxide), and a diaphragm, which is permeable for OH^-, separates the produced O_2 and H_2. For PEMWE, polymer electrolyte plays the role of gas separator. Alkaline electrolysis is well established as the most applied commercial technology, with the main advantages

of low cost (thanks to the use of non-noble electrodes), and long-term stability. In contrast, for PEMWE, the corrosion issue of many metals at acidic condition confines the choice of catalysts to some noble metal-based materials, which, together with the high cost of polymeric membranes, challenges its commercialization.[8]

1.1.1 Hydrogen evolution reaction (HER)

HER mechanism

HER occurs at the cathode of a water electrolyzer by the reduction of protons (in acidic medium) or water molecules (in alkaline medium). It is a two-electron transfer reaction, which may proceed through either the Volmer-Heyrovsky or the Volmer-Tafel mechanism.[9,10]

At acidic condition ($2H^+ + 2e^- \rightarrow H_2$):

	$H^+ + e^- + M \rightarrow M\text{-}H$	Volmer step
followed by either	$H^+ + e^- + M\text{-}H \rightarrow H_2 + M$	Heyrovsky step
or	$2M\text{-}H \rightarrow H_2 + 2M$	Tafel step

At alkaline condition ($2H_2O + 2e^- \rightarrow H_2 + 2OH^-$):

	$H_2O + e^- + M \rightarrow M\text{-}H + OH^-$	Volmer step
followed by either	$H_2O + e^- + M\text{-}H \rightarrow H_2 + OH^- + M$	Heyrovsky step
or	$2M\text{-}H \rightarrow H_2 + 2M$	Tafel step

where M indicates an active site, and M-H represents an adsorbed hydrogen atom.

Take HER at alkaline condition (also shown in Figure 4) for example: in the first step (Volmer step), a H_2O molecular combines with an electron at an active site (M) forming an adsorbed hydrogen atom (M-H) intermediate. Then, another H_2O molecular reacts with a second electron at the same position of the M-H intermediate generating H_2 (Heyrovsky step), or two M-H in the vicinity combine together generating H_2 (Tafel step).

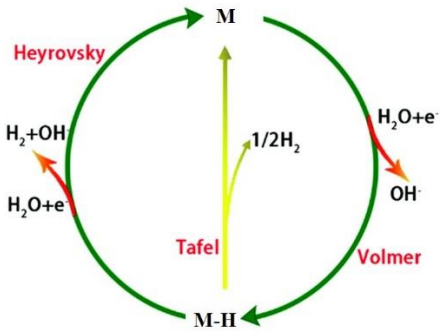

Figure 4 Elemental steps for HER at alkaline condition. M represents the active site. Reprinted with permission from reference [8]. Copyright © The Royal Society of Chemistry 2020.

Descriptor for HER activity

For HER, the overall reaction rate is significantly determined by the hydrogen adsorption free energy, ΔG_H.[11] If hydrogen is weakly bonded to the catalyst surface, the reaction will be limited by the adsorption (Volmer) step, while if the binding is too strong, the desorption (Heyrovsky/Tafel) step will limit the reaction rate. The rate-limiting step can be assessed by the Tafel slope, and slope values of 120, 40, and 30 mV dec^{-1} correspond to the Volmer, Heyrovsky, and Tafel step limitations, respectively. A volcano-type relationship between the HER exchange current density and ΔG_H has been widely reported, where Pt shows as the most active catalyst (Figure 5).

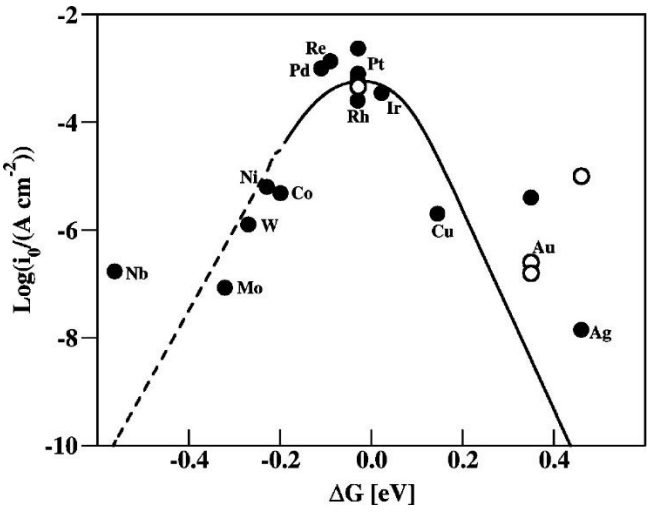

Figure 5 The measured exchange current density plotted against the calculated free energy of H adsorption at U = 0 V. Single crystal data are indicated by open symbols. The metals on the left side have high H coverage, while the metals on the right side have low H coverage. Reprinted with permission from reference [12]. Copyright © 2010 American Chemical Society.

Electrocatalysts for HER

Although the Pt group metals have shown excellent electrocatalytic activities for HER, the high cost and scarcity hinder their widespread application. Different approaches have been explored in order to improve the utilization efficiencies of these noble metals, such as controlling the size and shape,[13–18] incorporating with transition metals,[19–28] and using supporting materials[29–35].

Meanwhile, many efforts have been made in exploring non-noble transition metal-based (Fe, Co, Ni, Cu, Mo, W, etc.) nanomaterials, including pure metals and their alloys, oxides, nitrides, chalcogenides, phosphides, carbides, and borides, and some of them show comparable HER activities to those of benchmarking Pt-based materials.[36–48] Besides, there are also some works on metal-free catalysts for HER, which mainly are focused on graphene and g-C_3N_4 with element doping.[49,50]

1.1.2 Oxygen evolution reaction (OER)

OER mechanism

Oxygen evolution reaction (OER) occurs at the anode of a water electrolyzer. It involves a four-electron transfer, and thus suffers from sluggish kinetics compared with HER.[51,52] The mechanisms for OER are shown as below and in Figure 6:

At acidic condition ($2H_2O \rightarrow 4e^- + O_2 + 4H^+$):

$$H_2O + M \rightarrow e^- + M\text{-}OH + H^+$$

$$M\text{-}OH \rightarrow e^- + M\text{-}O + H^+$$

followed by either $H_2O + M\text{-}O \rightarrow e^- + M\text{-}OOH + H^+$

$$M\text{-}OOH \rightarrow e^- + O_2 + H^+ + M$$

or $2M\text{-}O \rightarrow O_2 + 2M$

At alkaline condition ($4OH^- \rightarrow 4e^- + O_2 + 2H_2O$):

$$OH^- + M \rightarrow e^- + M\text{-}OH$$

$$OH^- + M\text{-}OH \rightarrow e^- + M\text{-}O + H_2O$$

followed by either $OH^- + M\text{-}O \rightarrow e^- + M\text{-}OOH$

$$OH^- + M\text{-}OOH \rightarrow e^- + O_2 + H_2O + M$$

or $2M\text{-}O \rightarrow O_2 + 2M$

where M indicates an active site, and M-OH, M-O, and M-OOH represent adsorbed intermediates.

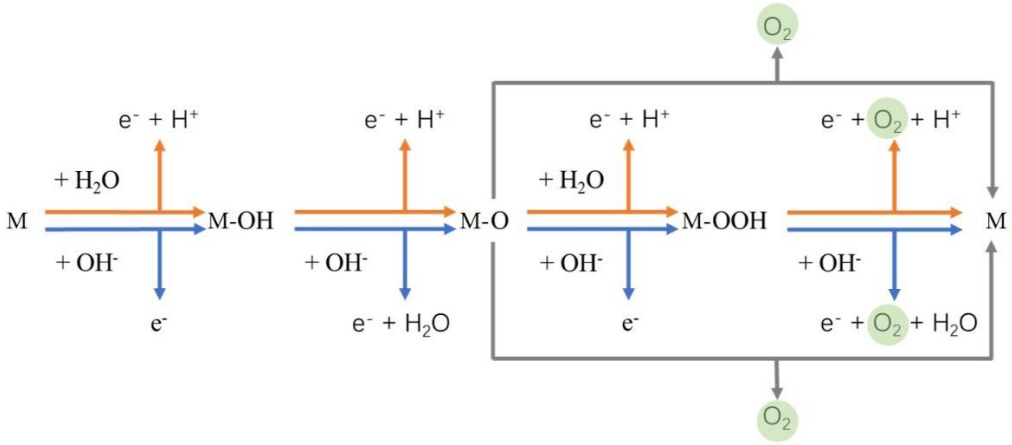

Figure 6 OER mechanisms at acidic (orange route) and alkaline (blue route) conditions. The grey lines indicate the combination of two adjacent M-O intermediates to generate oxygen. (M indicates an active site.)

Take OER at alkaline condition for example: firstly, a OH^- loses an electron forming M-OH intermediate on the electrode surface. Another OH^- diffuses to the M-OH, and loses an electron forming M-O intermediate. Then, a third OH^- moves to the M-O, and loses an electron generating M-OOH intermediate, followed by a fourth OH^- diffusing to the M-OOH and losing an electron generating O_2. Or two adjacent M-O combines together generating O_2.

Descriptor for OER activity

Similar to HER, there is also a widely accepted activity descriptor for determining the free energy diagram and describing the OER activity, which is $\Delta G_{M\text{-}O} - \Delta G_{M\text{-}OH}$. A volcano-type plot was constructed over a wide variety of metal oxide surfaces (Figure 7),[53] which indicates that RuO_2 is a suitable electrocatalyst for OER.

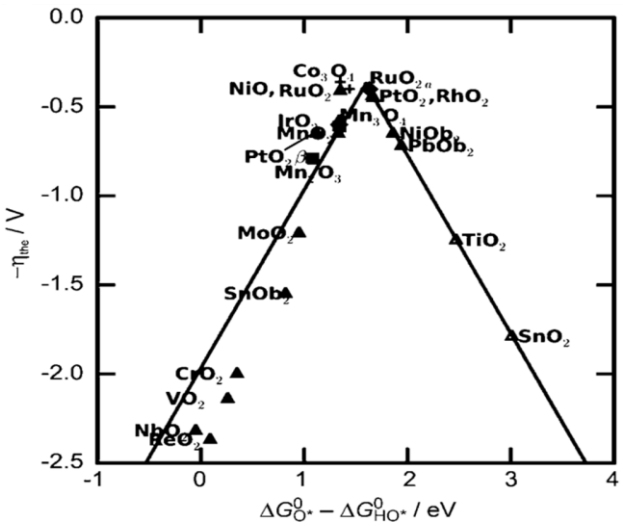

Figure 7 Activity trends towards OER for rutile, anatase, Co_3O_4, and Mn_xO_y oxides. The negative values of theoretical overpotential were plotted against the standard free energy of ΔG^0_{O*} - ΔG^0_{HO*} step. Reprinted with permission from reference [53]. Copyright © 2011 WILEY-VCH Verlag GmbH & Co. KGaA, Weinheim

Electrocatalysts for OER

Generally, RuO_2 and IrO_2 are considered as benchmark electrocatalysts for OER owing to their high activity.[54] However, both of them could be oxidized under high anodic potential, and thus dissolve into solution during OER.[55] Also, since they are made of noble metals, it is not economic for large scale application.

Other metal oxide materials, including the perovskite family (ABO_3, A = alkaline-earth and/or rare-earth metal, B = transition metal),[56–58] the spinel family (AB_2O_4, A = alkaline-earth and/or transition metal, B = group thirteen element and/or transition metal),[59,60] and the layer structure-type family, including $M(OH)_2$ and MOOH (M = Ni, Co, Fe, and Mn),[61–65] have been revealed to display excellent activities towards OER. Non-oxide materials, such as metal chalcogenides and pnictides,[66–73] have also been investigated for OER.

1.2 Hydrogen fuel cell and oxygen reduction reaction (ORR)

Hydrogen fuel cell

A hydrogen fuel cell is a device that converts chemical energy of hydrogen fuel into electrical energy with water as the only product. Figure 8 shows the working principle of a hydrogen fuel cell, where the electrons released by hydrogen (oxidation) pass through the external circuit, and are consumed by oxygen (reduction), while H^+ or OH^- is transferred across the electrolyte. The electric current between anode and cathode supplies power for users.

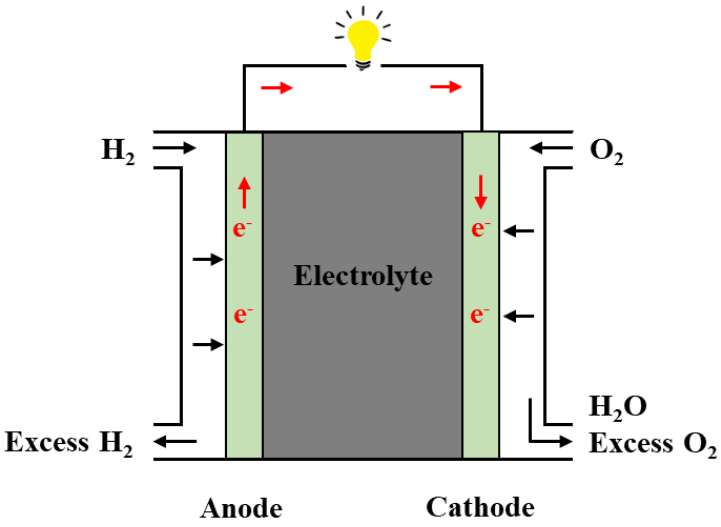

Figure 8 Scheme of a hydrogen fuel cell

The overall reaction occurring inside a hydrogen fuel cell is:[74]

$$H_2 + 1/2O_2 \rightarrow H_2O \qquad \Delta E = 1.23\ V$$

where ΔE is the theoretical open circuit voltage.

At the anode and cathode, hydrogen oxidation reaction (HOR) and oxygen reduction reaction (ORR) take place, respectively (Table 1).

Table 1 Electrode reactions for a hydrogen fuel cell

	in acidic medium	in alkaline medium
Anode	$H_2 \rightarrow 2e^- + 2H^+$	$H_2 + 2OH^- \rightarrow 2e^- + 2H_2O$
Cathode	$1/2O_2 + 2e^- + 2H^+ \rightarrow H_2O$	$1/2O_2 + 2e^- + H_2O \rightarrow 2OH^-$

Depending on the electrolyte used, there are generally two types of fuel cell: one is acidic fuel cell, in which the electrolyte conducts protons, while the other is alkaline fuel cell, where the electrolyte transfers hydroxide ions. Compared to acidic fuel cells, alkaline fuel cells have some advantages: a) reaction kinetics are fast at alkaline condition, which can reduce or remove the need for noble metal based catalysts, such as Pt-based materials,[75] b) corrosion issues can be minimized at alkaline condition. Therefore, alkaline fuel cells have been considered as the next generation of fuel cell technology, and great efforts have been made for their development. However, there are still some challenges with alkaline fuel cells. For example, they possess relatively low ionic conductivities, insufficient stabilities, and fuel crossover problem, etc.

The output voltage of a hydrogen fuel cell theoretically is 1.23 V, but in fact the value is much lower than that, mainly due to the slow kinetics of ORR at the cathode compared with HOR at the anode. Therefore, the exploration of effective ORR electrocatalysts is crucial for the development of hydrogen fuel cell technology.

ORR mechanism

ORR generally involves either an efficient four-electron pathway producing H_2O (in acidic medium) / OH^- (in alkaline medium), which is desirable for a hydron fuel cell, or a two-electron pathway producing H_2O_2 (in acidic medium) / HO_2^- (in alkaline medium) followed by further reduction or

decomposition.[76] (For ORR by four-electron pathway, it can be considered as the reverse process of OER.) The detailed mechanisms of ORR are:

At acidic condition:

	$4e^-$ Pathway ($O_2 + 4e^- + 4H^+ \rightarrow 2H_2O$)	$2e^-$ Pathway ($O_2 + 2e^- + 2H^+ \rightarrow H_2O_2$)
either	$O_2 + e^- + H^+ + M \rightarrow M\text{-}OOH$	$O_2 + e^- + H^+ + M \rightarrow M\text{-}OOH$
	$M\text{-}OOH + e^- + H^+ \rightarrow H_2O + M\text{-}O$	$M\text{-}OOH + e^- + H^+ \rightarrow H_2O_2 + M$
or	$O_2 + 2M \rightarrow 2M\text{-}O$	
followed by	$M\text{-}O + e^- + H^+ \rightarrow M\text{-}OH$	
	$M\text{-}OH + e^- + H^+ \rightarrow H_2O + M$	

At alkaline condition:

	$4e^-$ Pathway ($O_2 + 4e^- + 2H_2O \rightarrow 4OH^-$)	$2e^-$ Pathway ($O_2 + 2e^- + H_2O \rightarrow HO_2^- + OH^-$)
either	$O_2 + e^- + H_2O + M \rightarrow M\text{-}OOH + OH^-$	$O_2 + e^- + H_2O + M \rightarrow M\text{-}OOH + OH^-$
	$M\text{-}OOH + e^- \rightarrow OH^- + M\text{-}O$	$M\text{-}OOH + e^- \rightarrow HO_2^- + M$
or	$O_2 + 2M \rightarrow 2M\text{-}O$	
followed by	$M\text{-}O + e^- + H_2O \rightarrow M\text{-}OH + OH^-$	
	$M\text{-}OH + e^- \rightarrow OH^- + M$	

where M indicates an active site, and M-OOH, M-O, and M-OH represent adsorbed intermediates.

Descriptor for ORR activity

A volcano-type plot of ORR activity versus the oxygen binding energy (ΔE_O) has been constructed on various metal surfaces (Figure 9).[77] If the oxygen binding is too strong (left branch), the activity will be limited by the removal of M-O or M-OH, whereas if the binding is too weak (right branch), the activity will be limited by the O_2 adsorption and subsequent formation of M-O. A desirable ORR catalyst should bind oxygen neither too strongly nor too weakly, such as Pt.

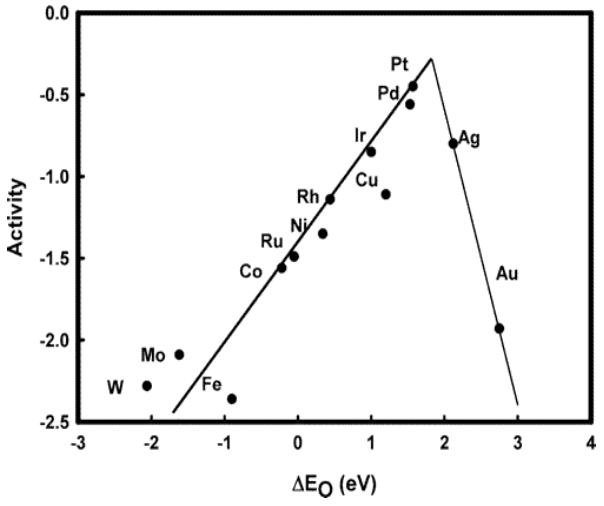

Figure 9 Trends in ORR activity plotted as a function of the oxygen binding energy. Reprinted with permission from reference[77]. Copyright © 2004 American Chemical Society

Electrocatalysts for ORR

For Pt-based ORR electrocatalysts, many strategies have been adopted to increase their intrinsic activities and active sites, such as alloying, controlling the particle size, and constructing well-defined shapes (core-shell structures, nano frames, nano cages, etc.).[78–82]

Non-noble transition metal compounds, such as non-noble transition metal oxides, nitrides, carbides, and phosphides, have been attractive towards ORR.[83–90] Besides, a wide range of carbon-based materials, such as carbon nanotubes, graphene, carbon quantum dots, carbon cages, and carbons

derived from metal-organic frameworks, have also been investigated as electrocatalysts for ORR.[91–96] Recently, single atom-based materials with metal active sites dispersed on supports at atomic level are emerging as highly effective ORR electrocatalysts.[97–101]

1.3 Strategies for designing electrocatalysts

In general, there are two major strategies to improve activities of electrocatalysts, i.e., increasing intrinsic activity and increasing number of active sites (Figure 10).

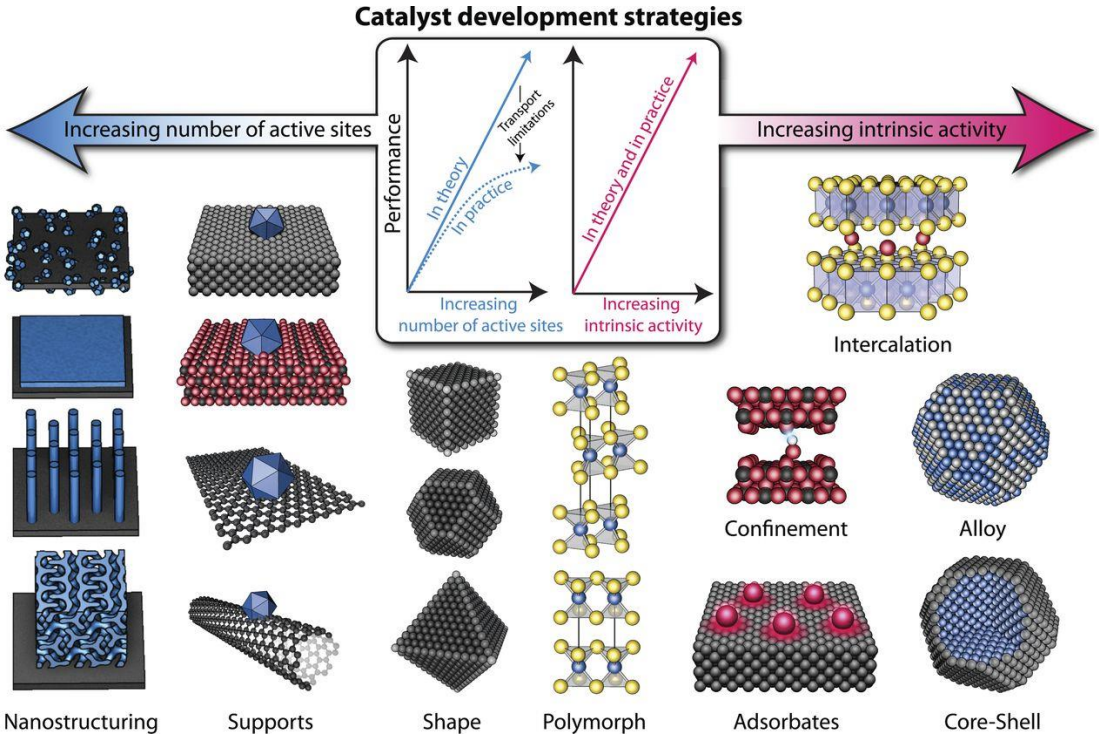

Figure 10 Catalyst development strategies. Schematic of various catalyst development strategies, which aim to increase the number of active sites and/or increase the intrinsic activity of each active site. Reprinted with permission from reference [102]. Copyright © 2017, American Association for the Advancement of Science

For the former strategy, it can be conducted by heteroatom doping, strain engineering, or alloying. Heteroatoms doping could modulate structural and electrical properties of catalysts. For instance, it

has been found that the incorporation of even a trace amount of Fe into a Ni-containing compound could dramatically enhance the OER activity.[103] Heteroatoms normally can be introduced either using heteroatom enriched precursors or by post-treatment of the product with heteroatom sources. Strain engineering is another method for tailoring the electronic structures and catalytic activities of materials. Shao-Horn and coworkers demonstrated that epitaxial strain could tune the activity of oxygen electrocatalysis at alkaline condition.[104] Besides, alloying another element into the lattice of a given monometallic metal is also assumed to be able to improve the electrocatalytic activity. For example, a series of transition metal alloys, such as NiFe, NiCo, and MnCo, were found to show better electrocatalytic activities than their monometallic counterparts with enhanced binding with the reaction intermediates.[105]

To increase number of active sites, methods can be fabricating nano morphologies or porous structures. Various types of nanostructured catalysts have been investigated, including nanoparticles, nanosheets, nanorods, nanowires, etc.[8] Porous structures provide catalysts with better electrolyte permeability, and make the pathways of mass and electron transport short, accelerating the reaction. In general, porous structures can be obtained by means of: a) external template method (hard or soft template), b) self-template method with the aid of porous precursors, such as metal-organic frameworks, c) dealloying, and d) hybridizing with porous substrates, such as Ni foam.

In recent years, various catalyst support materials have been proposed and studied, particularly nanostructured carbon materials, such as graphene, carbon nanotubes, and carbon nanofibers. Graphene consists of bidimensional and one-atom-thick carbon layer, which displays outstanding physicochemical properties, such as an extremely large specific surface area (2630 $m^2 g^{-1}$), and a very high mobility of charge carriers (about 200 000 $cm^2 V^{-1} s^{-1}$).[106] These features of graphene are much

superior to conventional graphitic carbon, which normally shows a specific surface area about 250 m^2 g^{-1}, and mobility of charge carriers about 6000 cm^2 V^{-1} s^{-1}. The very large specific surface area would render an excellent dispersion of the active sites, and a facile mass transport of reactants and products. The high mobility of charge carriers would significantly decrease ohmic drops.[107] Graphene displays extraordinary chemical and electrochemical stability over wide potential range, and can withstand harsh electrolyte environment that is generally encountered in electrocatalytic processes. For instance, in order to achieve efficient operation of water electrolysis, a strong acid or base solution is required for increasing the ionic conductivity, and minimizing the pH gradient because of proton consumption and production at the cathode and anode electrode, respectively.[108] Moreover, defect engineering and chemical doping in graphene supply an additional degree of freedom for tailoring the anchoring sites for catalysts dispersion, which provides a rich playground for exploring synthetic strategies and tuning metal-support interactions.[109] These all make graphene an attractive supporting substrate for various nanostructured catalysts.

Carbon nanotubes (CNTs), consisting of graphitic basal planes that are rolled together in cylindrical form, have high surface area, excellent electrical conductivity, special electronic properties, and good thermal and chemical stability, indicating that they are also suitable supports for electrocatalysts.[110] For instance, Davodi and coworkers introduced multiwall carbon nanotubes functionalized with nitrogen-rich emeraldine salt as a promising catalyst support to improve the electrocatalytic activity of magnetic maghemite (γ-Fe_2O_3) nanoparticles for water splitting.[111] Valenti et al. reported co-axial heterostructures integrating palladium/titanium dioxide with CNTs as efficient electrocatalysts for hydrogen evolution reaction.[112]

1.4 Structure of this thesis

This PhD project focuses on the exploration of nanomaterials as electrocatalysts for water electrolysis and fuel cells in alkaline solution. Figure 11 shows a preview of the contents that will be present in the following chapters.

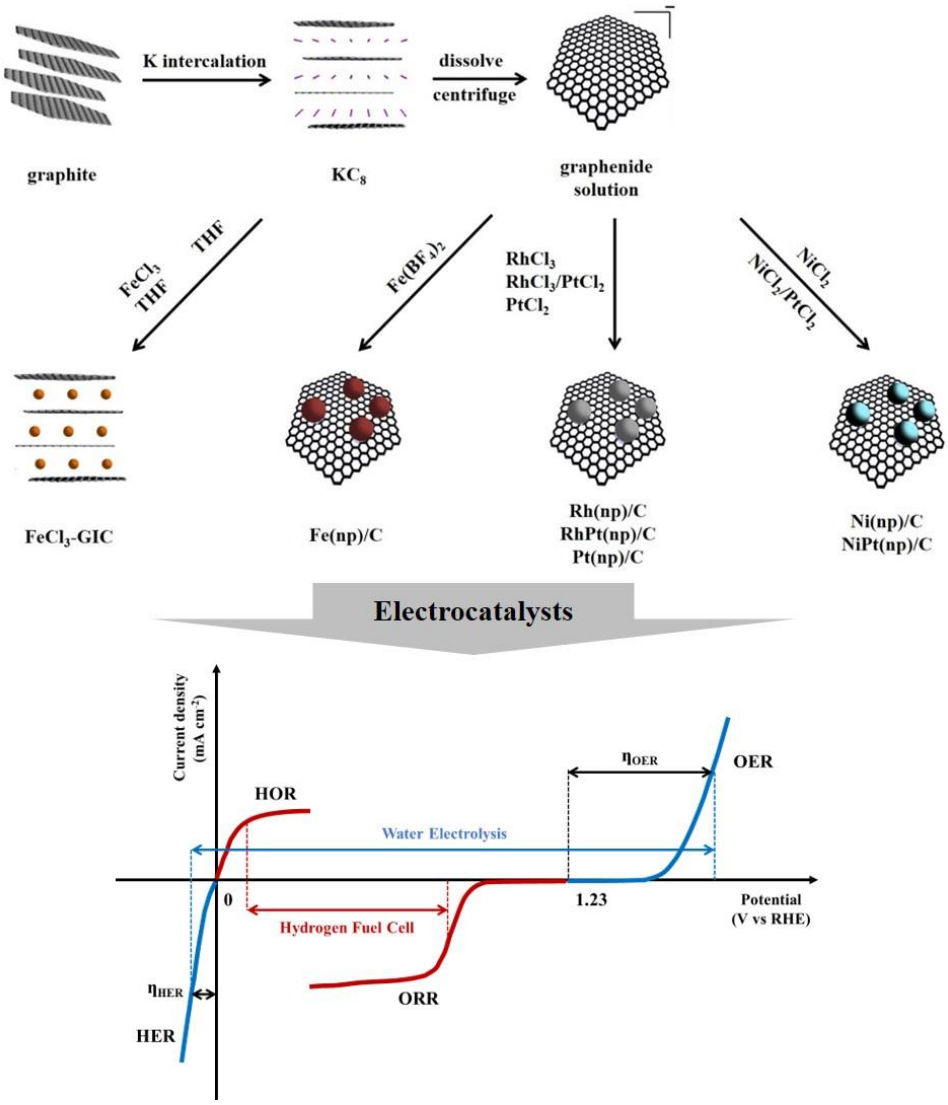

Figure 11 Scheme of this PhD project including synthesis of nanomaterials and their application in electrocatalysis.

This thesis is organized in the following sequence:

Chapter 1 introduces energy conversion-involving electrochemical technologies, i.e., water electrolysis and hydrogen fuel cell, and the fundamentals of corresponding electrode reactions,

specially HER, OER, and ORR. General strategies of designing electrocatalysts for these reactions are also described.

Chapter 2 involves a facile method of preparing iron inclusion compound, and its electrocatalytic activity towards OER and ORR at alkaline condition is shown.

In Chapter 3, a synthetic route of carbon-supported iron oxide nanoparticles composite materials is developed and optimized by investigating the experimental factor of starting graphite materials. The electrocatalytic activities of the prepared materials for OER and ORR at alkaline condition are studied, and the effect of catalyst size on electrocatalytic performance is discussed.

Chapter 4 focuses on generalizing the synthetic route by tunning the metal precursors from non-noble metal to noble metal. The electrocatalytic performance of the obtained noble metal-based nanomaterials for water electrocatalysis in alkaline medium is examined.

Chapter 5 shows further generalization of the synthetic route by combining non-noble metal with noble metal. The electrocatalytic performance for HER at alkaline condition is investigated.

And the conclusion.

Chapter 2 Iron inclusion compound as electrocatalyst for oxygen reactions

2.1 Introduction

Graphite intercalation compounds (GICs) are a class of materials generated by inserting atomic or molecular species (called intercalants) between carbon layers in a graphite host material.[113] A variety of substances, such as alkali metals, sulfuric acid, and transition metal chlorides, can be used as intercalants.[114–116] Based on the orientation of electron transfer between intercalant and graphite, GICs can be divided into donor GICs and acceptor GICs.[117] For donor GICs, such as K-GIC, Li-GIC, and Cs-GIC, electrons are transferred from intercalants to carbon atoms of graphite during the intercalation process. For acceptor GICs, such as $FeCl_3$-GIC, H_2SO_4-GIC, and $NiCl_2$-GIC, electrons are transferred in the opposite orientation. GICs can be obtained by intercalation from liquid phase, vapor phase, or by electrochemical process.[118,119] One of the common processes involves molten salt method, which is conducted by sealing metal salt with graphite in a glass tube reactor under an ambient or chlorine atmosphere, which is carried out at temperatures from 350 ºC to 500 ºC.[117]

GICs have been studied for battery and electrode materials, chemical catalysis and catalytic applications, conductivity and other applications.[113] To the author's knowledge, very few works on these compounds has been done towards electrocatalysis. Zhao and coworkers synthesized GIC ($FeCl_3$) by mixing graphite and iron chloride in a pressurized vessel under an inert atmosphere, and placed in an oven at 380 °C for 12 h. For electrocatalysis of ORR in 0.1 M NaOH solution, the prepared GIC showed an onset potential of 0.73 V (vs reversible hydrogen electrode, RHE) and a mixed electron pathway with an electron transfer number of 2.5 at 0.5 V (vs RHE).[120]

In this chapter, iron inclusion compound (FeIC) was prepared by a facile synthesis, which allows to obtain product on a gram scale readily, and the catalytic activities for ORR and OER in alkaline solution were investigated.

2.2 Synthesis of material

Iron inclusion compound was synthesized by first generating the potassium intercalation compound KC_8 (Figure 12). Afterwards, the intercalation compound was exposed to tetrahydrofuran (THF), where the ternary intercalation compound $KC_{24}(THF)_x$ was formed, in agreement to previous works.[121] This ternary intercalation compound was then exposed to $FeCl_3$ dissolved in THF forming iron inclusion compound (FeIC) similar to the works of Schäfer-Stahl et al.[122] (Details were attached to the Appendix)

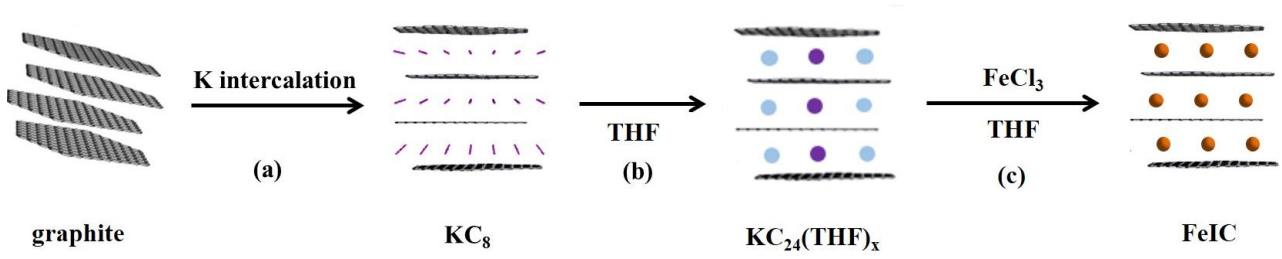

Figure 12 Scheme of synthesis of iron inclusion compound.

2.3 Results and discussion

Electrochemical measurements

The electrocatalytic ORR activity of the prepared FeIC was measured using a rotating ring disk electrode (RRDE) in O_2 saturated 0.1 M KOH electrolyte. RRDE technique is introduced in appendix 1. As shown in Figure 13, FeIC displayed an onset potential of 0.76 V (vs RHE). And ORR went

through a mixed (four- and two-) electron transfer pathway with an electron transfer number of 2.8 at 0.45 V (vs RHE). The results were similar to the literature (Table 2).

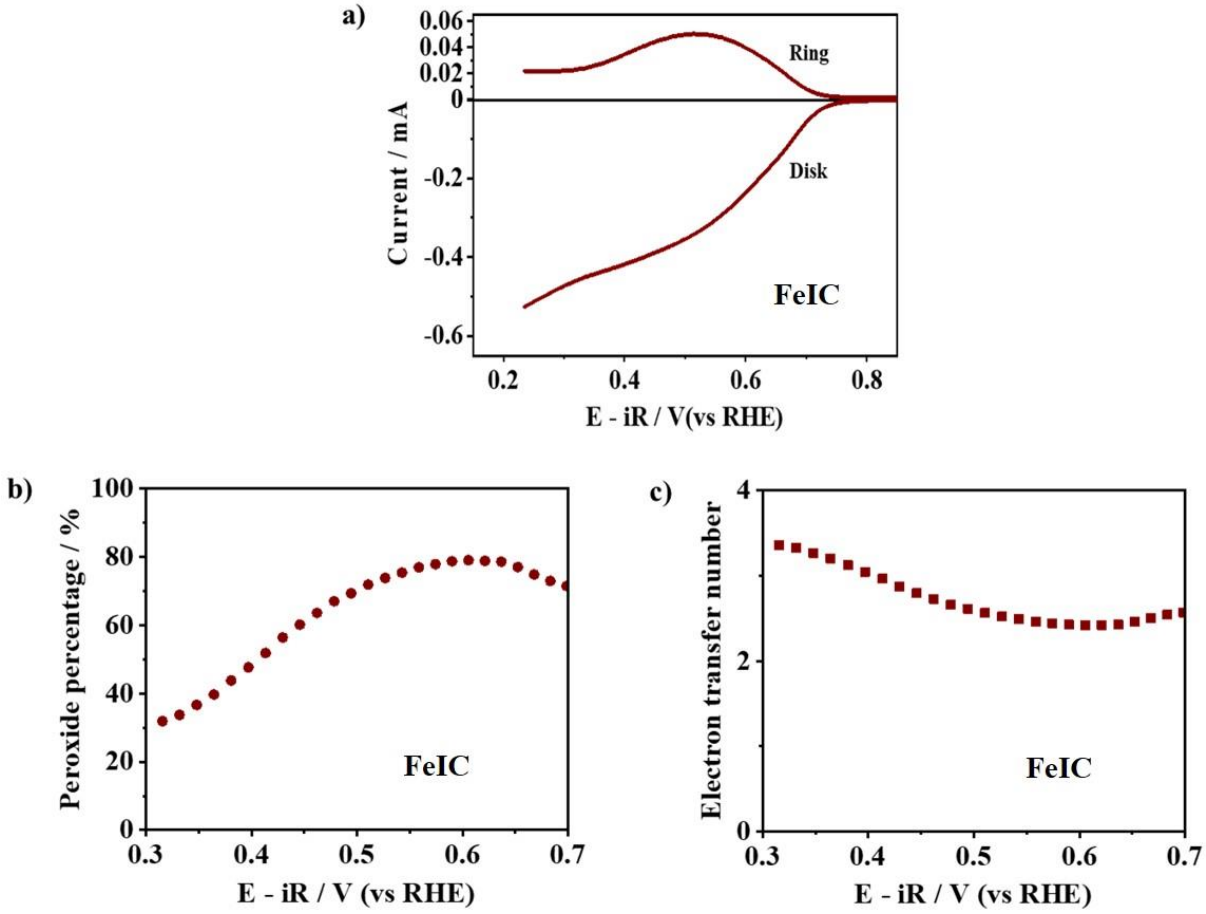

Figure 13 ORR performance of FeIC: (a) LSV curves from RRDE measurement under a rotation speed of 1600 rpm at a scan rate of 10 mV s^{-1} in an O_2 saturated 0.1 M KOH electrolyte. (b) the percentage of HO_2^- generated during ORR, and (c) electron transfer number against electrode potential.

The electrocatalytic activity of FeIC towards OER was examined in an Ar saturated 0.1 M aqueous KOH solution using a rotating disk electrode (RDE) in order to remove oxygen generated on the electrode surface. As shown in Figure 14, FeIC exhibited an onset potential of 1.69 V (vs RHE). To reach a current density of 5 mA cm^{-2}, an overpotential of 605 mV was required.

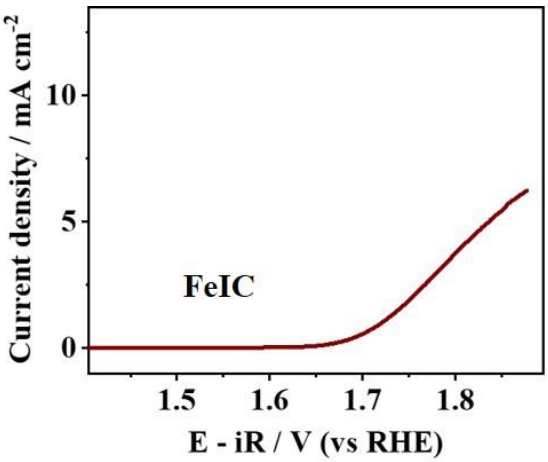

Figure 14 OER performance of FeIC. LSV curve from RDE measurement a scan rate of 10 mV s^{-1} under a rotation speed of 1600 rpm in Ar saturated 0.1 M aqueous KOH solution. Catalyst loading was 0.42 mg cm_{geo}^{-2}.

Table 2 Electrocatalytic performance of FeIC for ORR (and OER) in alkaline medium.

Catalyst	Electrolyte pH	Loading amount (mg cm_{geo}^{-2})	ORR Onset potential (V vs RHE)	ORR n at 0.45 V (vs RHE)	OER overpotential at 5 mA cm^{-2}	Ref.
graphite	13	0.6	0.70	2.0	-	[120]
GIC($FeCl_3$)	13	0.6	0.73	2.6	-	[120]
FeIC	13	0.42	0.76	2.8	605	This work

As shown above, an iron inclusion compound was prepared. The process of preparation was facile, and could be a promising way to obtain relatively large amount of electrocatalysts for ORR and OER.

Chapter 3 Carbon-supported iron oxide nanoparticles with varying size for electrocatalysis of oxygen reactions

3.1 Introduction

Electrochemical energy conversion and storage systems, such as water electrolyzers and fuel cells, have many advantages over traditional fossil fuel combustion, including high energy density, enhanced overall efficiency, and significant reduction of carbon dioxide emission.[123] Oxygen reduction reaction (ORR) and oxygen evolution reaction (OER) are important electrochemical reactions associated with fuel cells and water electrolyzers, respectively. Noble metal-based materials are generally considered as benchmark electrocatalysts for these oxygen-involving reactions, i.e., Pt for ORR, IrO_2 and RuO_2 for OER. However, the scarcity and high cost of noble metals limit their large-scale applications. Therefore, exploring non-noble metal-based electrocatalysts with high activities and stabilities is of great importance for developing these energy systems.

Non-noble transition metal oxides (TMOs) are attractive alternative catalysts thanks to several prominent advantages, such as multiple valence states and high abundance.[124] Various nanoscale TMOs, such as nanoneedle, nanocage, nanowire, and nanocube, have been reported as electrocatalysts.[125–128] Catalysts at nano scale would own improved surface area to volume ratio, and therefore more catalytic active sites would potentially be accessible for the reaction.

However, TMOs often suffer from inferior electrical conductivity, which would significantly affect their electrocatalytic activities due to lowered rates of electron transfer between catalyst surface and electrolyte.[129] For instance, a four-electron transfer process of ORR is preferred to generate water. But,

a less efficient two-electron transfer process may occur producing hydrogen peroxide intermediate, followed by another two-electron transfer process to generate water. To increase the conductivity, one way is adding dopants to the catalyst structure. The distribution of electron can be tuned by means of inserting atoms into vacancies and distorting the lattice structure.[130] Another way is combining TMOs with other highly electrically conductive materials, such as carbon-based supports. Porous carbon, carbon nanotube, graphene, etc., have been used for supporting TMOs.[131–133] For instance, Liang and co-workers have reported a hybrid material consisting of Co_3O_4 nanocrystals grown on reduced graphene oxide, which exhibited higher ORR activity than the Co_3O_4 alone.[134] Moreover, synergetic chemical coupling effects may exist between these nanocrystals and carbon supports, improving the catalytic activity.[135]

This chapter focuses on the synthesis of caron supported iron oxide nanoparticles composite materials and their applications as oxygen catalysts for electrochemical water splitting and fuel cells in alkaline medium. In particular, the effect of catalyst size on the electrocatalytic performance was investigated. It was reported with permission from: F. Hof, M. Liu, G. Valenti, E. Picheau, F. Paolucci, and A. Pénicaud. Size Control of Nanographene Supported Iron Oxide Nanoparticles Enhances Their Electrocatalytic Performance for the Oxygen Reduction and Oxygen Evolution Reactions. J. Phys. Chem. C, 2019, 123, 20774-20780.

3.2 Synthesis of materials

The synthetic route was shown in Figure 15. Firstly, the starting carbon material was intercalated with metal potassium under inert gas condition, forming KC_8 intercalation compound. Graphenide solution was then obtained upon dissolving KC_8 in anhydrous tetrahydrofuran (THF). The final composite material was prepared based on the reaction between graphenide solution and iron salt. (Details of synthesis are shown in Appendix.) The graphenide solution was composed of negatively charged carbon layers, which worked as reduction agent when mixed with iron salt.

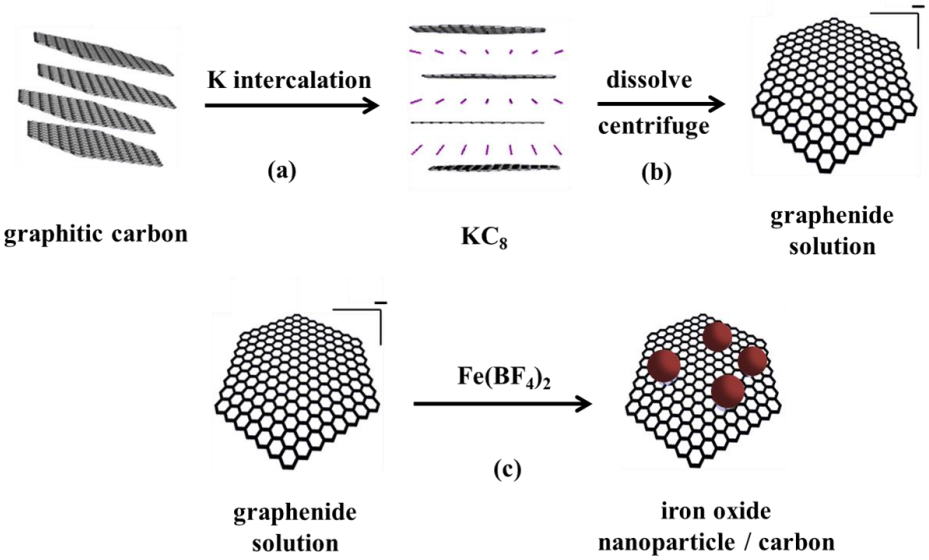

Figure 15 Scheme of synthetic route of iron oxide nanoparticle supported on carbon composite material

In particular, various graphite starting materials were used, including flake graphite, micro graphite, and graphitic nano carbon (Figure 16). Accordingly, graphenide solutions varying in carbon layer size would be obtained after K intercalations. Finally, composite materials differing in size were assumed to be prepared, denoted as l-Fe(np)/C (large size), m-Fe(np)/C (medium size), and s-Fe(np)/C (small size), respectively. “np” refers to nanoparticle.

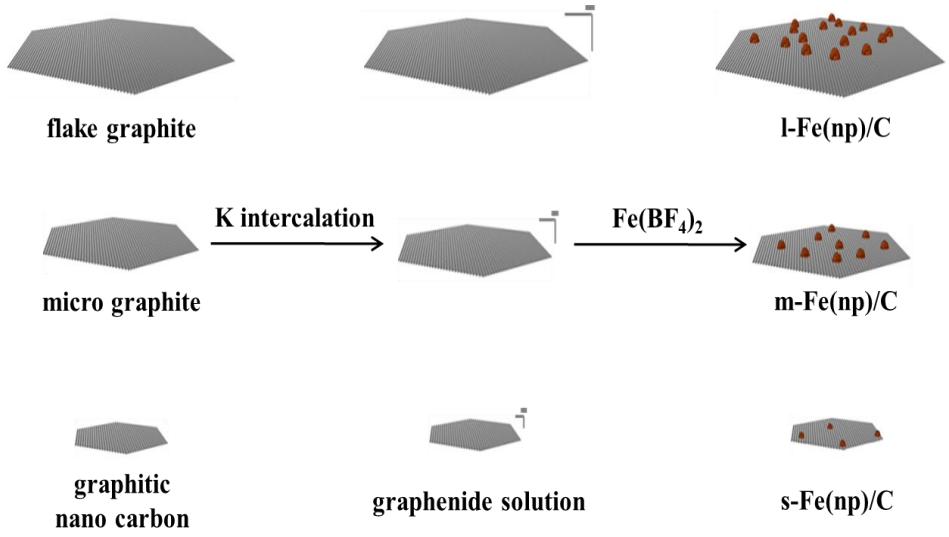

Figure 16 Scheme of synthesis of iron oxide nanoparticle with varying size / carbon composite materials, l-Fe(np)/C, m-Fe(np)/C, and s-Fe(np)/C, respectively.

3.3 Results and discussion

Physical characterizations

The structures, morphologies, and compositions of the prepared Fe(np)/Cs materials were characterized by means of X-ray diffraction (XRD), X-ray photoelectron spectroscopy (XPS), Transmission electron microscopy (TEM), and Thermogravimetric analysis (TGA).

The crystal structures of the prepared Fe(np)/C composite materials were demonstrated by XRD patterns. As shown in Figure 17, the diffraction peak positions were well matched with the maghemite γ-Fe_2O_3. The diffraction peaks at 30.1°, 35.7°, and 43.4° corresponded to the (220), (311), and (400) planes, respectively.[136] It was assumed that metallic nanoparticles initially were formed as graphenide solution reacted with $Fe(BF_4)_2$, and the following work up step and air exposure caused oxidation so that iron oxides were detected in the final composite materials.

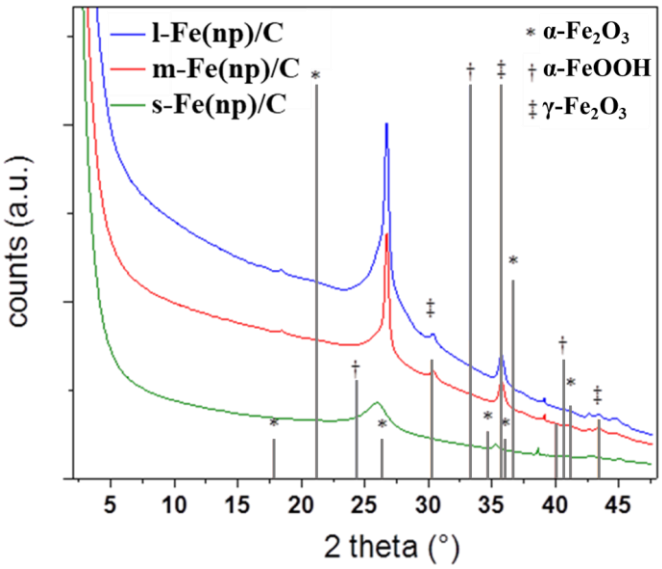

Figure 17 XRD patterns of the prepared Fe(np)/C composite materials comparing with the most likely iron oxide phases.

Also, peaks related to carbon, iron, and oxygen were detected from the XPS survey scan of the Fe(np)/C composite materials. From the performed fits in the Fe 2p XPS regions (Figure 18), it can be seen that iron (III) oxide/hydroxide species predominantly present in each of the Fe(np)/C composite material.[137] And the shapes of the peaks were quite similar, so the ratio between iron (III) oxide and iron (III) hydroxide wound not much differ from each other.

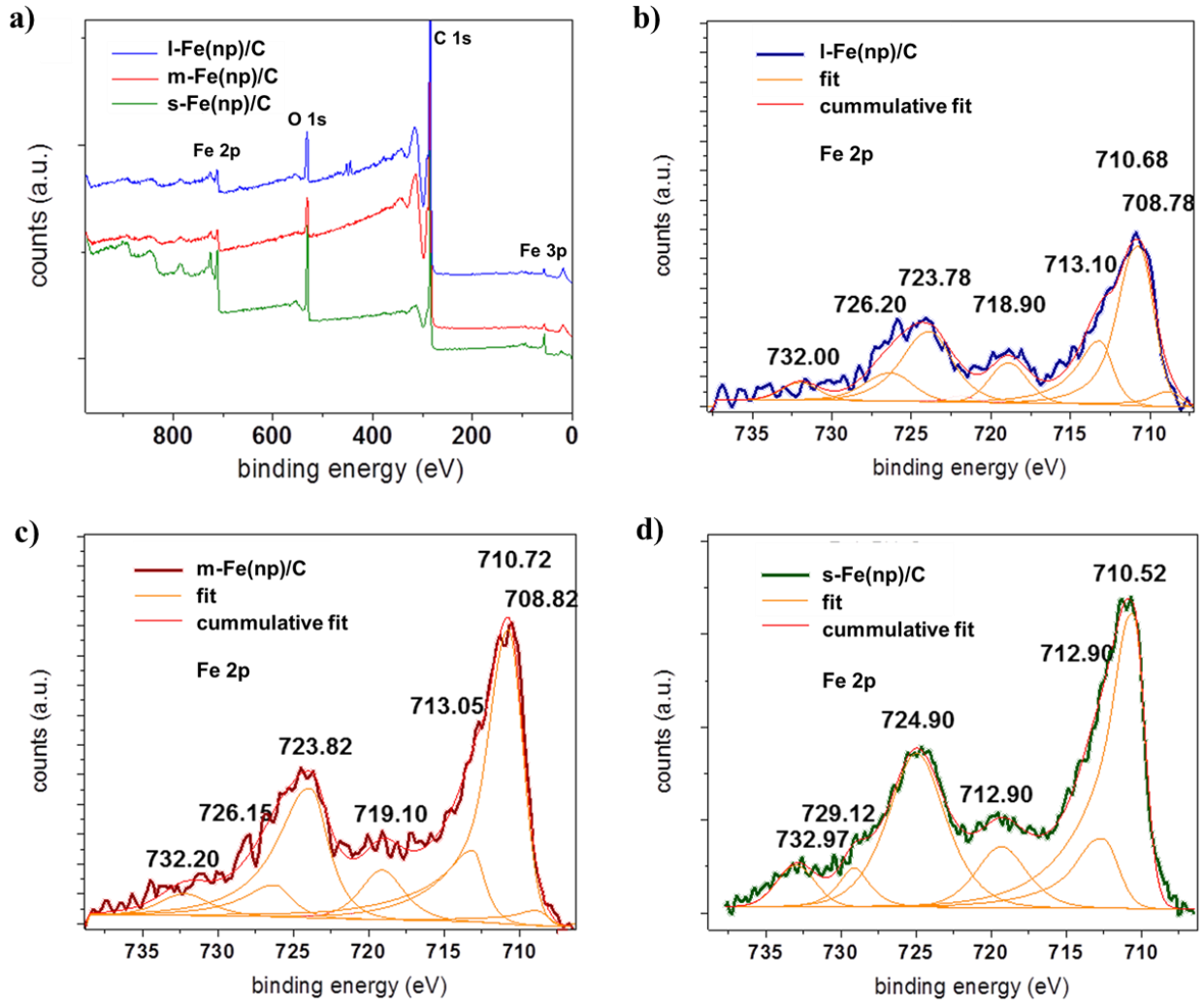

Figure 18 (a) XPS survey scan of the prepared Fe(np)/C composite materials. Fe 2p XPS spectra of (b) l-Fe(np)/C, (c) m-Fe(np)/C, and (d) s-Fe(np)/C, respectively.

The morphology information of the prepared composite materials was supplied by STEM images. As shown in Figure 19, the carbon layers and iron oxide nanoparticles can be clearly identified in Fe(np)/C composite materials, and nanoparticles were found to be attached to carbon layers, which is crucial to prevent catalyst active materials from leaching during electrocatalysis process. The chemical nature of the prepared materials was studied by Energy Dispersive X-Ray Spectroscopy (EDX), which revealed that iron species well distributed on carbon.

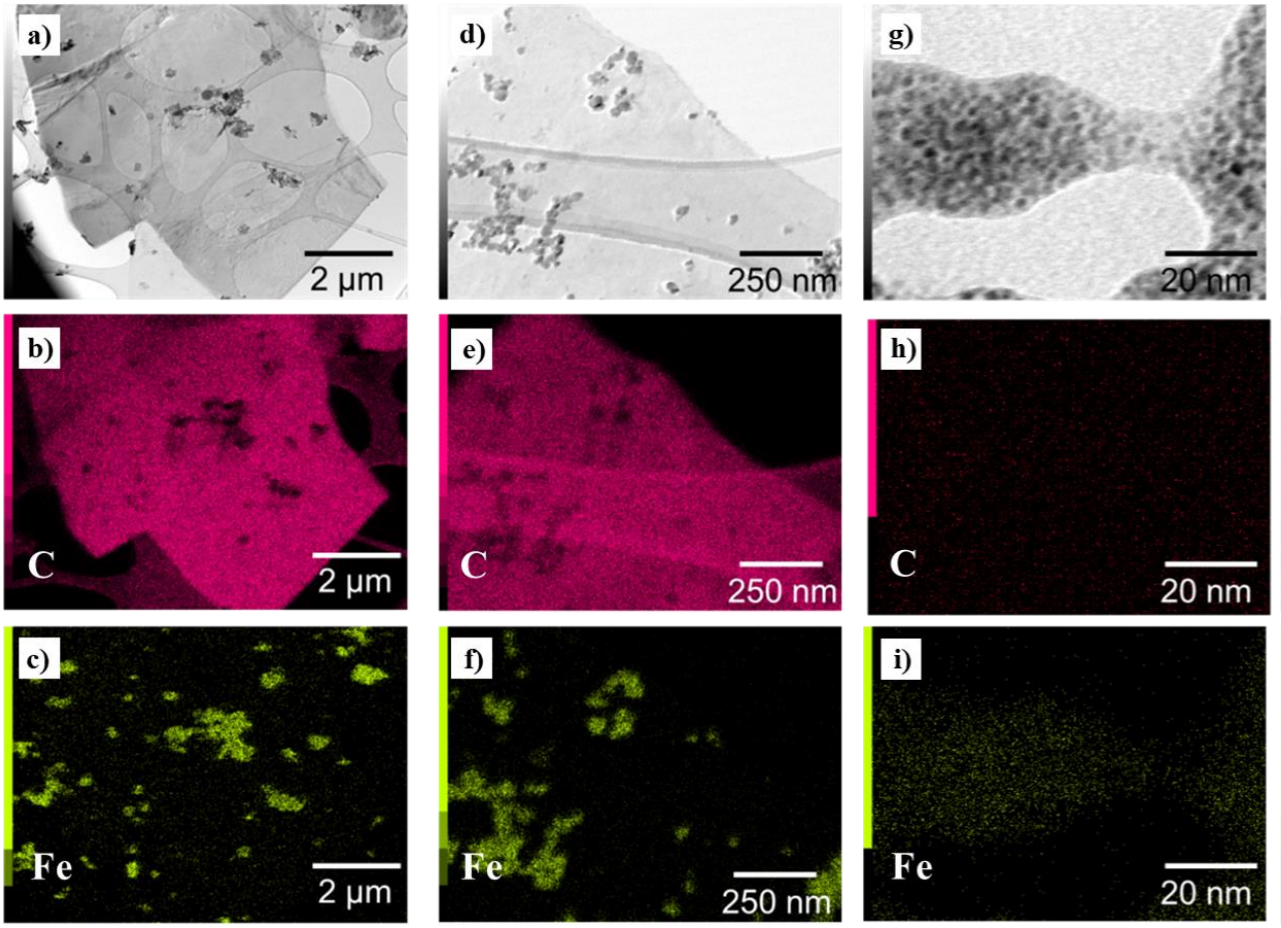

Figure 19 STEM images and EDX maps of carbon edge and iron edge of l-Fe(np)/C (a, b, and c), m-Fe(np)/C (d, e, and f), and s-Fe(np)/C (g, h, and i).

The size of carbon layers and iron oxide nanoparticles in the prepared Fe(np)/C composite materials were measured by the aid of TEM images (Figure 20 and Figure 21). For the l-Fe(np)/C sample, the carbon starting material of which was flake graphite, carbon layers up to about 10 μm were found and centred at about 2μm. For the m-Fe(np)/C sample, the carbon starting material of which was micro graphite, carbon layers were observed up to about 3 μm, and centred at about 0.7 μm. For the s-Fe(np)/C sample, the carbon starting material of which was graphitic nano carbon, the average dimension of the carbon layers was 50 nm. Meanwhile, the average size of the iron oxide nanoparticle was about 50 nm for the l-Fe(np)/C sample, 35 nm for the m-Fe(np)/C sample, and 3 nm for the s-Fe(np)/C sample. By correlating the area of carbon layer with the average nanoparticle size, a clear trend towards larger nanoparticle was found as the carbon layer dimension increased.

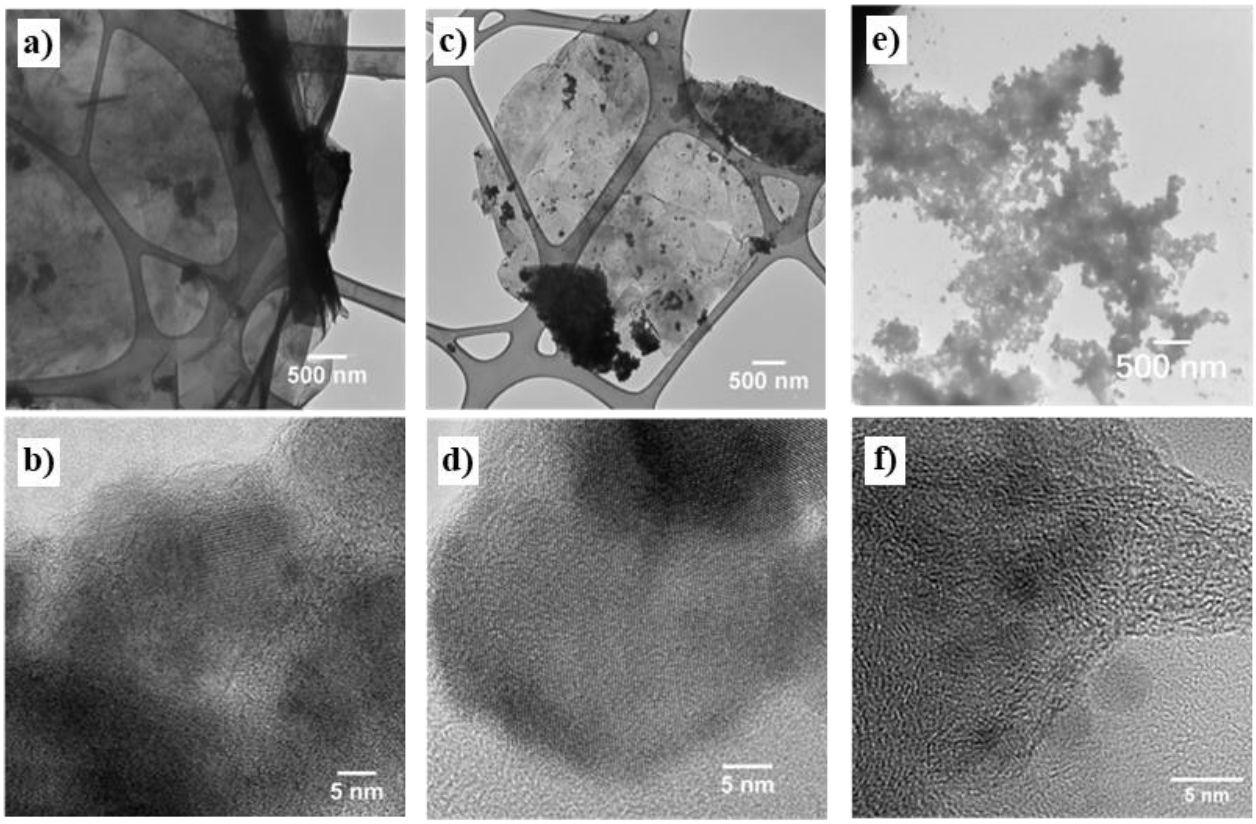

Figure 20 TEM images of l-Fe(np)/C (a, b), m-Fe(np)/C (c, d), and s-Fe(np)/C (e, f) at lower and higher magnifications.

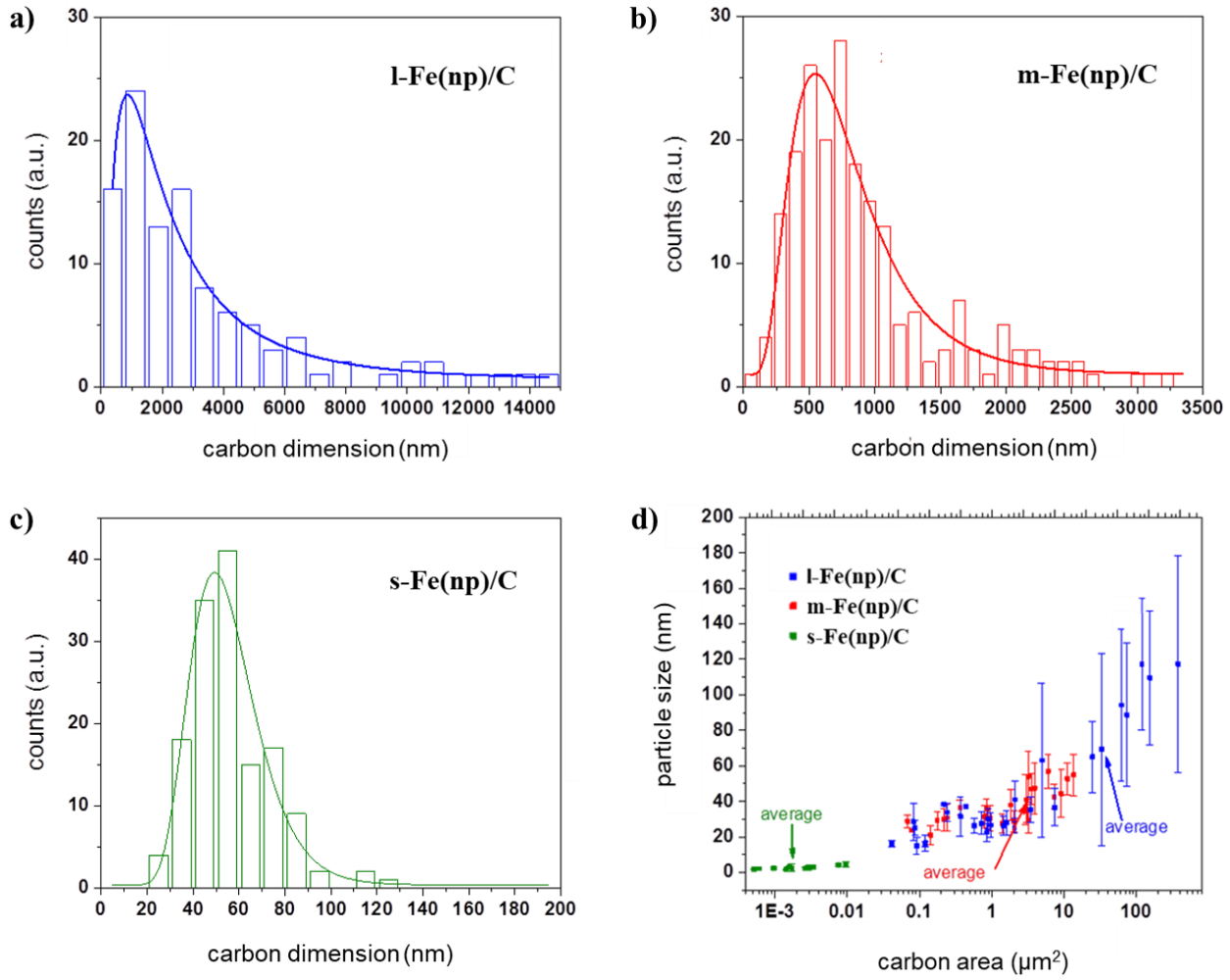

Figure 21 Histograms of the distribution of carbon layer dimension for (a) l-Fe(np)/C, (b) m-Fe(np)/C, and (c) s-Fe(np)/C based on over 200 individual counts in about 40 TEM images each. The histograms were fitted by a lognormal function. (d) Correlation between the area of carbon layer and the size of nanoparticle. The distribution of particle size was based on an average of 653, 574, and 127 counts for l-Fe(np)/C, m-Fe(np)/C, and s-Fe(np)/C, respectively.

In addition, the mass ratios of iron oxide nanoparticles in the Fe(np)/C composite materials were evaluated by TGA measurement in synthetic air. As shown in Figure 22, the values were between 15.4 wt% and 21.4 wt%.

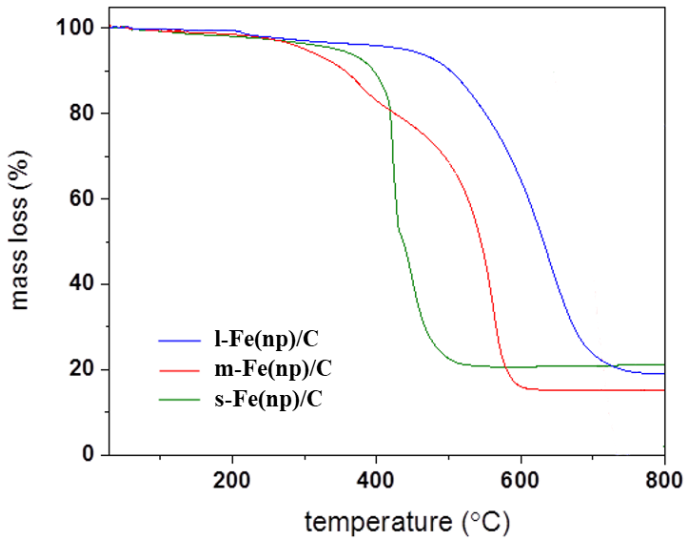

Figure 22 TGA measurements of the prepared Fe(np)/C composite materials in synthetic air (80% N_2, 20% O_2) between 30-800 °C.

Electrochemical measurements

From above physical characterizations, it can be confirmed that iron oxide nanoparticles with varying size supported on carbon composite materials were successfully prepared. The obtained Fe(np)/C materials were then utilized as electrocatalysts for ORR and OER in alkaline solution. The electrochemical measurement techniques and metrics involved are present in Appendix 1.

For investigating electrocatalytic activities of Fe(np)/Cs towards ORR, cyclic voltammetry (CV) was firstly performed within a potential range of about 0.4 V to 1.0 V (vs reversible hydrogen electrode, RHE) at a scan rate of 10 mV s^{-1} in an Ar and O_2 saturated 0.1 M aqueous KOH solution, respectively. As shown in Figure 23, in the case of electrolyte saturated with Ar, only capacitive current was presented, indicating that there was no redox occurring. In contrast, when the electrolyte was saturated

with O_2, the CV curves showed a substantial reduction process, which was resulted from oxygen reduction. And the s-Fe(np)/C sample exhibited a more positive onset potential for ORR, 0.79 V (vs RHE) than the m-Fe(np)/C sample, 0.75 V (vs RHE), and the l-Fe(np)/C sample, 0.73 V (vs RHE). Also, the ORR peak potential positions followed such a trend. Here, it can initially be identified that the prepared composite material with smaller iron oxide nanoparticle would show higher electrocatalytic activity for ORR. More experimental evidence will be shown below.

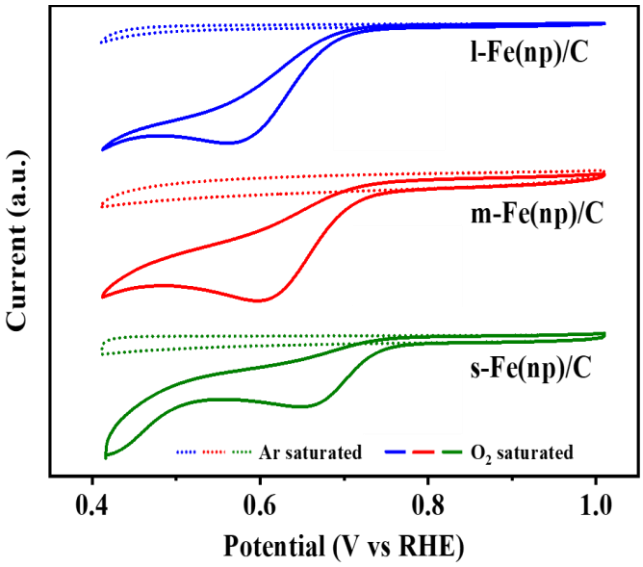

Figure 23 CV curves of l-Fe(np)/C, m-Fe(np)/C, and s-Fe(np)/C at a scan rate of 10 mV s^{-1} in an Ar saturated (dotted lines) and O_2 saturated (solid lines) 0.1 M aqueous KOH solution.

Then, CV curves were recorded using a rotating disk electrode (RDE) under different rotation speed (500 rpm, 900 rpm, 1600 rpm, and 2500 rpm, rpm refers to revolutions per minute) at a scan rate of 10 mV s^{-1} in an O_2 saturated 0.1 M KOH electrolyte.

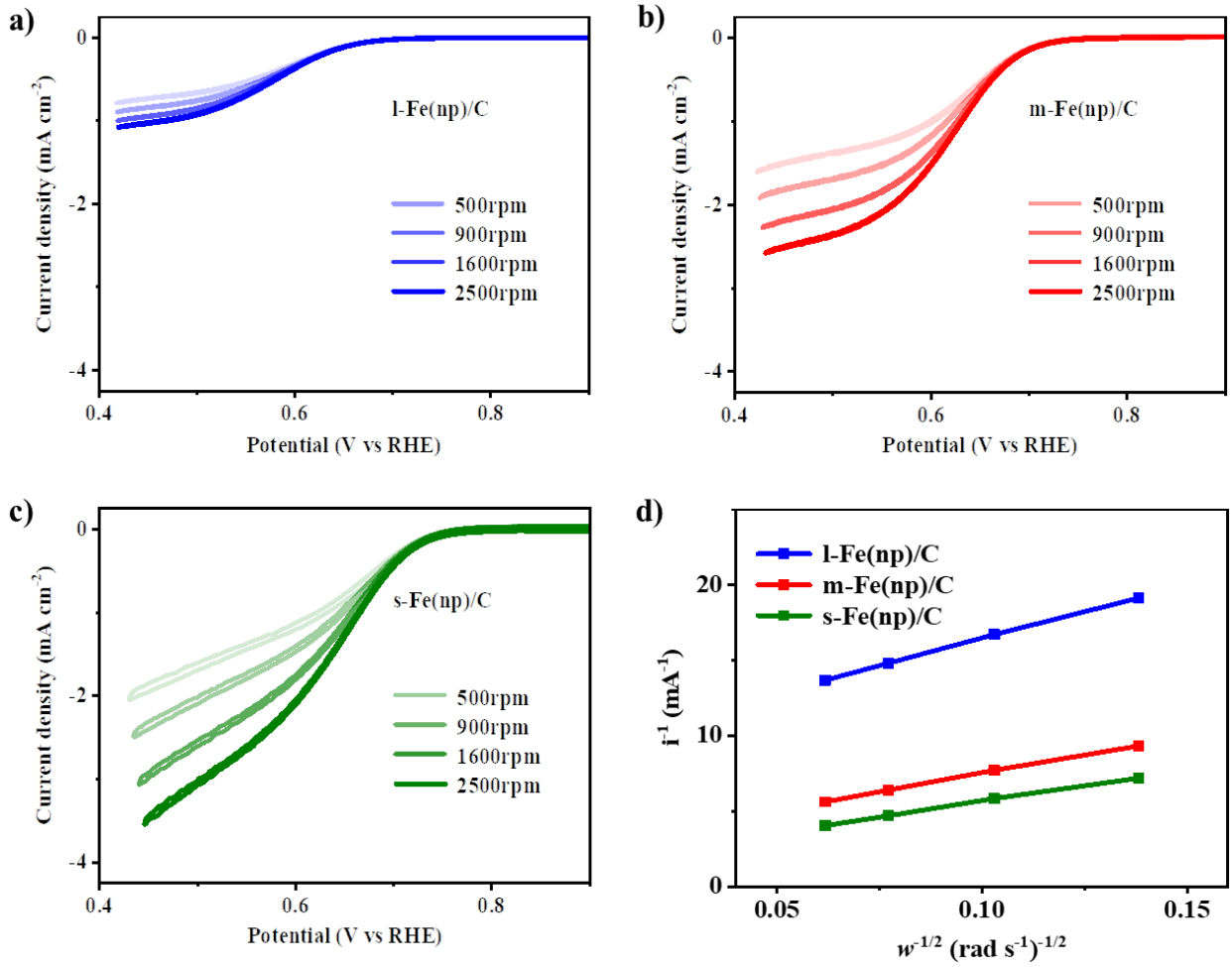

Figure 24 CV curves of (a) l-Fe(np)/C, (b) m-Fe(np)/C, and (c) s-Fe(np)/C under rotation speeds of 500 rpm, 900 rpm, 1600 rpm, and 2500 rpm at a scan rate of 10 mV s^{-1} in an O_2 saturated 0.1 M aqueous KOH solution. (d) Corresponding K-L plots at the potential of 0.45 V (vs RHE).

It can be seen from Figure 24 that due to the faster diffusion process in higher rotation, the mass transport current increases as the rotation speed increases, and the s-Fe(np)/C sample exhibited higher ORR current densities than the m-Fe(np)/C and l-Fe(np)/C samples under each rotation speed. Moreover, from the intercepts of Koutecký-Levich (K-L) plots (i^{-1} against $w^{-1/2}$), the kinetic current

densities (j_K) of Fe(np)/C materials for ORR can be achieved, which were 9.3 mA cm^{-2}, 5.4 mA cm^{-2}, and 1.5 mA cm^{-2} for s-Fe(np)/C, m-Fe(np)/C, and l-Fe(np)/C sample, respectively, at the potential of 0.45 V (vs RHE).

As explained before, there are generally two pathways for ORR, i.e., four-electron transfer pathway generating OH^- (in alkaline medium) or two-electron transfer pathway generating HO_2^- (in alkaline medium). In order to investigate the pathway of ORR on the electrode loaded with the prepared Fe(np)/C composite material, rotating ring disk electrode (RRDE) measurements were conducted. Current from the disk electrode due to oxygen reduction and current from the ring electrode duo to oxidation of HO_2^- intermediate generated during ORR were collected at the same time (see linear sweep voltammetry, LSV, curves in Figure 25). It can be seen that the values varied with the electrode potential, and as the potential was scanned negatively, s-Fe(np)/C came to display lower HO_2^- percentage and higher electron transfer number than m-Fe(np)/C and l-Fe(np)/C. For instance, the electron transfer numbers at the potential of 0.45 V (vs RHE) were 3.6, 3.37, and 2.96 for s-Fe(np)/C, m-Fe(np)/C, and l-Fe(np)/C, respectively, suggesting that the prepared composite material with smaller iron oxide nanoparticle would promote oxygen reduction in a more effective pathway. For comparation, ORR performance of commercial Pt/C was also tested, and shown in Figure 26. Not surprisingly, it displayed a close to four electron transfer number and low percentage of HO_2^- intermediate.

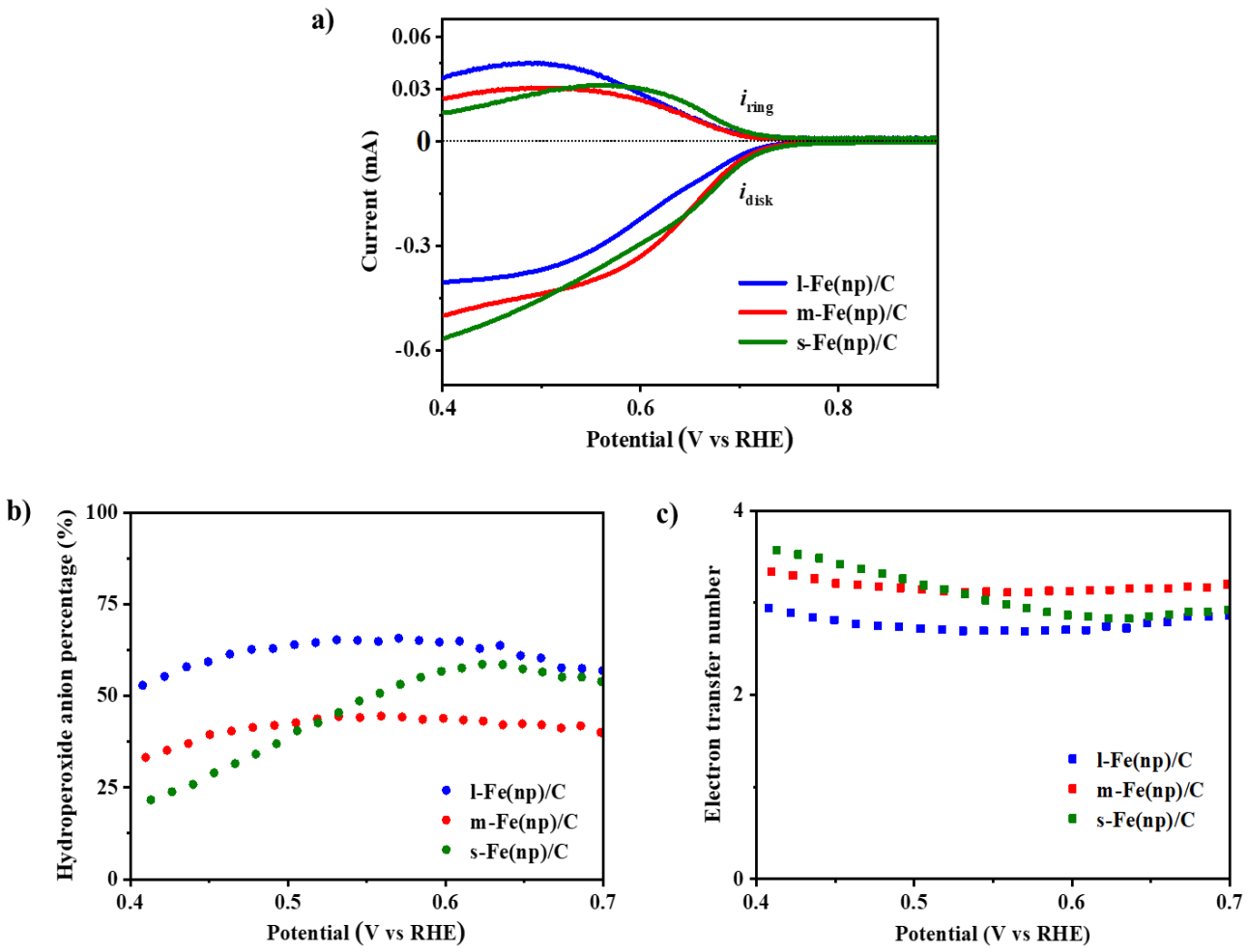

Figure 25 (a) LSV curves of Fe(np)/C samples from RRDE measurement under a rotation speed of 1600 rpm at a scan rate of 10 mV s^{-1} in an O_2 saturated 0.1 M KOH electrolyte. i_{ring} and i_{disk} refer to current from the ring electrode and disk electrode, respectively. (b) the percentage of hydroperoxide anion generated during ORR and (c) electron transfer number of ORR against electrode potential.

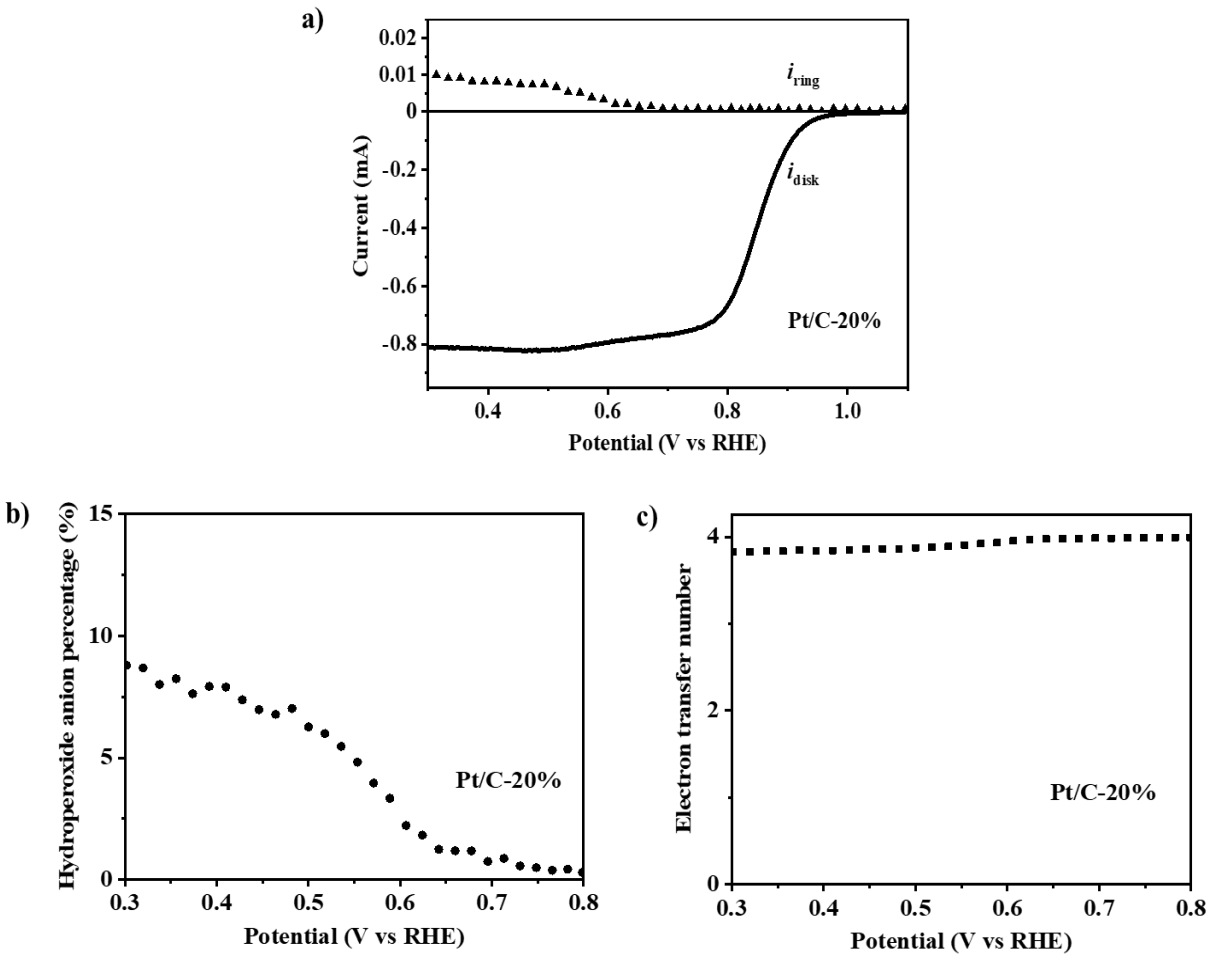

Figure 26 ORR performance of commercial Pt/C-20wt%: (a) LSV curves from RRDE measurement under a rotation speed of 1600 rpm at a scan rate of 10 mV s^{-1} in an O_2 saturated 0.1 M KOH electrolyte. i_{ring} and i_{disk} refer to current from the ring electrode and disk electrode, respectively. (b) the percentage of HO_2^- generated during ORR, and (c) electron transfer number against electrode potential.

In addition, the stability of the prepared Fe(np)/C materials for ORR was evaluated by means of chronoamperometric measurement at 0.7 V (vs RHE) in O_2 saturated 0.1 M aqueous KOH solution under a rotation speed of 1600 rpm. As shown in Figure 27, the s-Fe(np)/C sample showed a higher current retention (96%) after 2000 s, while m-Fe(np)/C and l-Fe(np)/C maintained 93% and 69% of the initial current, respectively. Moreover, the s-Fe(np)/C sample still kept a high current retention when the test continued up to 1.5 h.

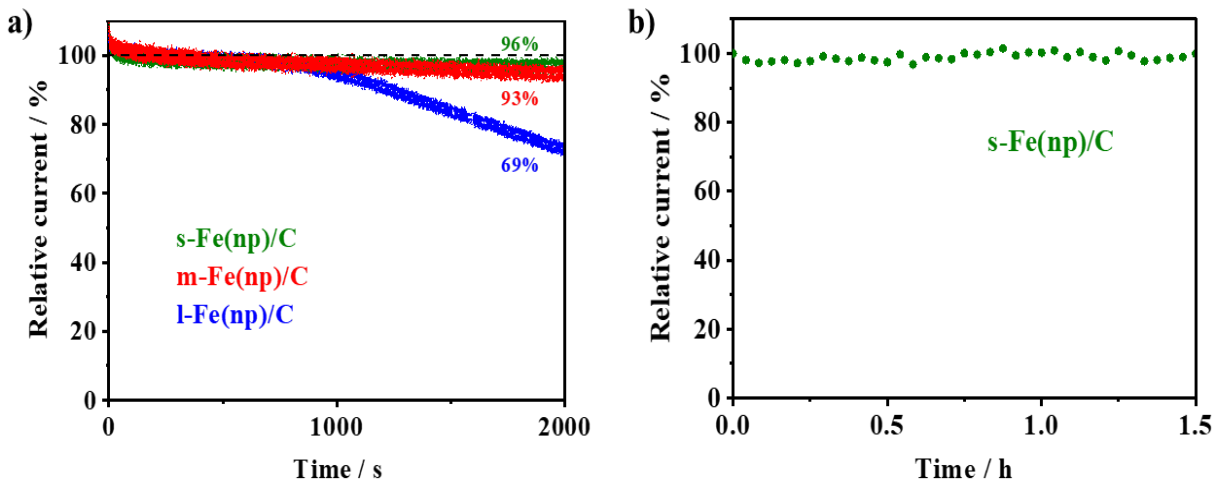

Figure 27 Chronoamperometric responses for ORR of Fe(np)/Cs until 2000 s (a) and of s-Fe(np)/C up to 1.5 h (b) at 0.7 V (vs RHE) in O_2 saturated 0.1 M aqueous KOH solution under a rotation speed of 1600 rpm.

On the other side, the electrocatalytic activities of Fe(np)/Cs towards OER were examined in an Ar saturated 0.1 M aqueous KOH solution using a RDE in order to remove oxygen generated on the electrode surface.

Firstly, cyclic voltammetry was performed at a scan rate of 10 mV s^{-1} under a rotation speed of 1600 rpm. As shown in Figure 28, the s-Fe(np)/C sample exhibited a lower onset potential (closer to the standard redox potential of O_2 / OH^-, 1.23 V (vs RHE) at room temperature) compared with m-Fe(np)/C and l-Fe(np)/C. And, to reach a current density of 1 mA cm^{-2}, the s-Fe(np)/C sample displayed an overpotential of 420 mV, while the overpotential needed by m-Fe(np)/C and l-Fe(np)/C were 450

mV and 460 mV, respectively. To reach a current density of 10 mA cm^{-2}, the s-Fe(np)/C sample showed an overpotential of 456 mV, which was much less than m-Fe(np)/C and l-Fe(np)/C. The corresponding Tafel plots (overpotential against logarithm of current density) were also present, and the Tafel slope of s-Fe(np)/C, m-Fe(np)/C, and l-Fe(np)/C were calculated to be 36 mV dec^{-1}, 77 mV dec^{-1}, and 84 mV dec^{-1}, respectively. The OER activity of RuO_2 was shown in Figure 29. As can be seen, though the onset potential of s-Fe(np)/C was more positive than RuO_2, at higher potentials the difference of activity between s-Fe(np)/C and RuO_2 became smaller. And, the Tafel slope of RuO_2 (68 mV dec^{-1}) was even larger than s-Fe(np)/C.

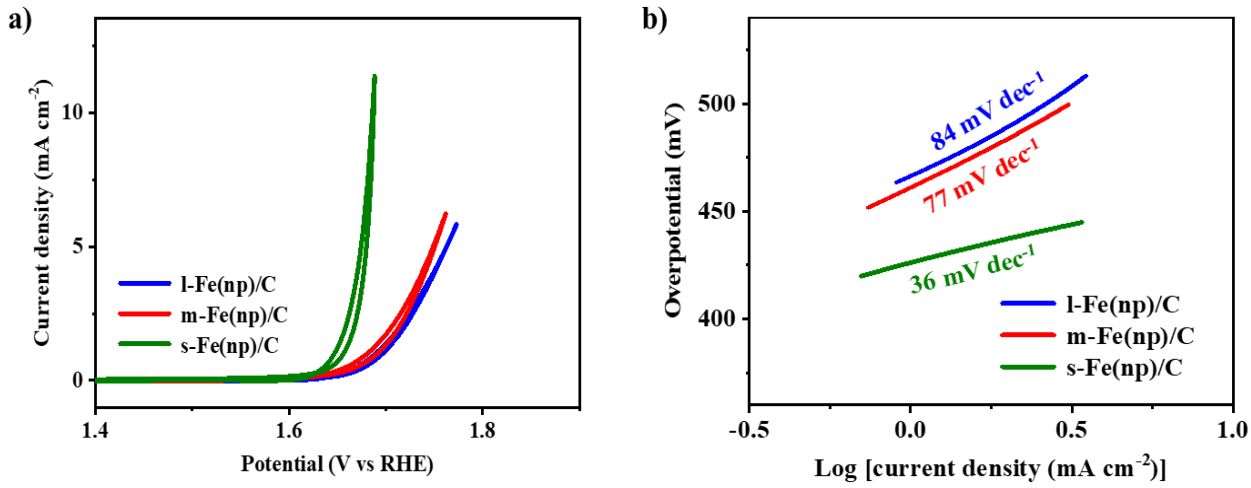

Figure 28 (a) CV curves of the Fe(np)/C samples for OER at a scan rate of 10 mV s^{-1} under a rotation speed of 1600 rpm in Ar saturated 0.1 M aqueous KOH solution. (b) corresponding Tafel plots.

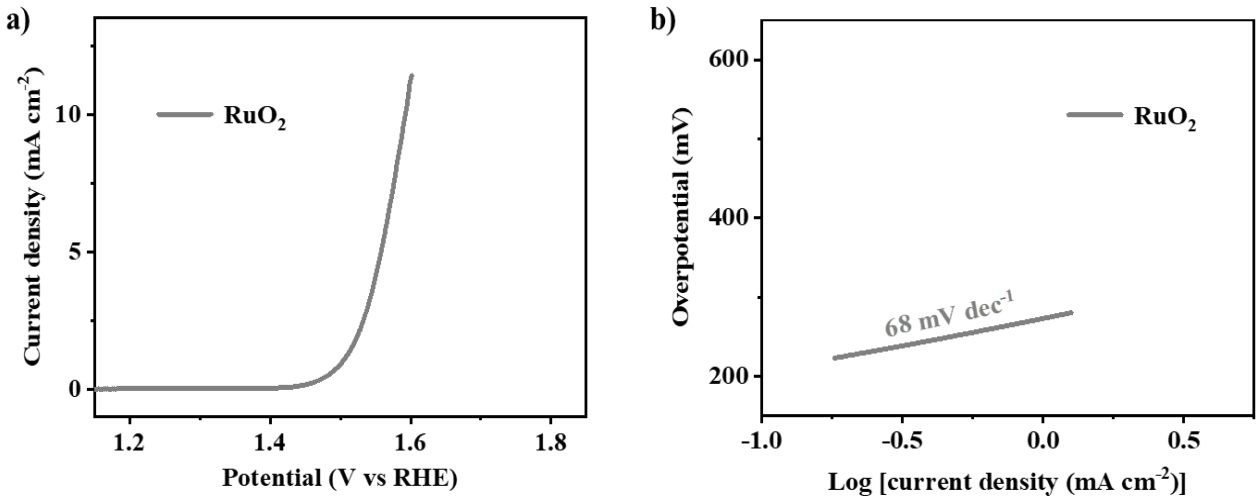

Figure 29 OER performance of RuO_2: (a) LSV curve from RDE measurement a scan rate of 10 mV s^{-1} under a rotation speed of 1600 rpm in Ar saturated 0.1 M aqueous KOH solution. (b) corresponding Tafel plot. Catalyst loading was 0.42 mg cm_{geo}^{-2}.

Besides, the stability of s-Fe(np)/C sample for OER was evaluated by means of chronoamperometric measurement at 1.68 V (vs RHE) in Ar saturated 0.1 M aqueous KOH solution under a rotation speed of 1600 rpm. As shown in Figure 30, the s-Fe(np)/C sample was able to maintain 92% of the initial current after 1.5 h electrocatalysis operation.

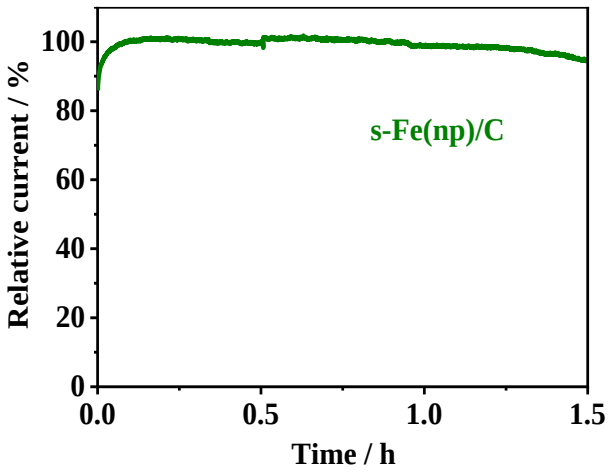

Figure 30 Chronoamperometric response of s-Fe(np)/C for OER up to 1.5 h at 1.68 V (vs RHE) in Ar saturated 0.1 M aqueous KOH solution under a rotation speed of 1600 rpm.

A brief review of non-precious transition metal oxide-based materials as electrocatalysts for OER and/or ORR was shown in Table 3. The catalytic activities of various materials are closely related to the composition, and may connect with mass loadings used for measurements as well. Basically, the prepared Fe(np)/C composite material, specially s-Fe(np)/C, showed good electrocatalytic activities towards OER and ORR, which can be attributed to: a) the very small size of iron oxide nanoparticle controlled by the amount of charge available in graphenide solution during the synthesis. b) the use of carbon support, which were assumed to be able to better disperse nanoparticle so that more surface area of catalyst could be exposed to the reactants, and improve the electron transfer rate between the electrode and the interface. c) the possible existence of synergetic chemical coupling effects between iron oxide nanoparticles and carbon layers.

Table 3 Catalytic parameters for non-precious transition metal oxide-based electrocatalysts for OER and/or ORR.

Catalyst	Electrolyte (aqueous KOH)	Loading amount (mg cm_{geo}^{-2})	OER Overpotential (mV) at 10 mA cm^{-2}	OER Tafel slope (mV dec^{-1})	ORR Onset potential (V vs RHE)	ORR Electron transfer number	Ref.
$CoFe_2O_4$/rGO	0.1 M	1	473	-	0.827	3.84-3.9 at 0.16-0.66 V vs RHE	[138]
Co_3O_4-$MnCo_2O_4$ / N-rGO	0.1 M	~0.12	-	-	~0.89	3.9-4.0 at 0.1-0.5 V vs RHE	[139]
Co_3O_4 nano octahedron	0.1 M	0.5	530	67	-	-	[140]
$CoCr_2O_4$/CNS	0.1 M	0.24	365	58	-	-	[59]

Catalyst	Electrolyte (aqueous KOH)	Loading amount (mg cm_{geo}^{-2})	OER Overpotential (mV) at 10 mA cm^{-2}	OER Tafel slope (mV dec^{-1})	ORR Onset potential (V vs RHE)	ORR Electron transfer number	Ref.
Commercial RuO_2	0.1 M	0.24	374	65	-	-	[59]
$CoFe_2O_4$/C	0.1 M	0.5	400	-	0.823	3.93-3.95 at 0.16-0.66 V vs RHE	[141]
$FeCo_2O_4$/G	0.1 M	1.0	~498	62	0.87	~3.9 at 0.15-0.55 V vs RHE	[142]
IrO_2	1 M	0.21	338	47	-	-	[64]
IrO_2/C	0.1 M	0.2	370	-	-	-	[143]
$ZnCo_2O_4$/N-CNT	0.1 M	0.2	420	70.6	0.95 (Pt/C, 1.05)	3.8 (Pt/C, 3.9) at 0.4-0.7 V vs RHE	[144]
Co_3O_4/N-rmGO	0.1 M	0.17	-	-	0.88	3.9 at 0.6-0.75 V vs RHE	[145]
FeNC sheets/NiO	0.1 M	0.24	390	76	-	-	[146]
$NiCo_2O_4$-rGO	0.1 M	0.4	-	-	0.87	3.8 at 0.36-0.51 V vs RHE	[147]
Co_3O_4@C-MWCNT	1 M	0.325	320	62	0.89	~3.9	[148]

Catalyst	Electrolyte (aqueous KOH)	Loading amount (mg cm_{geo}^{-2})	OER Overpotential (mV) at 10 mA cm^{-2}	OER Tafel slope (mV dec^{-1})	ORR Onset potential (V vs RHE)	ORR Electron transfer number	Ref.
					(0.1 M KOH)	at 0.35-0.75 V vs RHE (0.1 M KOH)	
$CoFe_2O_4$ nanofiber	0.1 M	0.42	410 at 5 mA cm^{-2}	82	-	-	[60]
Fe_2O_3 nanofiber	0.1 M	0.42	550 at 5 mA cm^{-2}	149	-	-	[60]
Mn_3O_4 nanoparticle	0.1 M	0.25	>600 at 3 mA cm^{-2}	60	-	-	[149]
s-Fe(np)/C	0.1 M	0.35	456	36	0.79	3.6 at 0.45 V vs RHE	This work

To conclude, in this chapter, the synthesis of iron oxide nanoparticles with varying size supported on carbon composite materials, Fe(np)/Cs, were explored. The small size nature and fine dispersion on carbon support of the prepared particles were characterized by a couple of methods, such as XRD, STEM-EDX, and TEM. And, the catalytic activities and stabilities of Fe(np)/Cs for OER and ORR were investigated by means of electrochemical techniques. The experimental results were analyzed and compared with other similar electrocatalysts. This work supplies a promising route to synthesize nanoparticles loaded on support materials for electrocatalysis of oxygen reactions.

Chapter 4 Carbon-supported noble metal-based nanomaterials for water electrocatalysis

4.1 Introduction

Hydrogen (H_2) is one of the promising sources of clean energy to replace fossil fuels in the future. Water electrocatalysis supplies a sustainable way for H_2 production. So far, Pt-based materials have shown the best electrocatalytic activities for hydrogen evolution reaction (HER), while Ir / Ru oxides are considered as benchmark electrocatalysts for oxygen evolution reaction (OER).

Rhodium (Rh) is a 4d transition metal on the top rank of the Pt-group metals. It has high catalytic activities for many reactions, such as photocatalytic carbon dioxide reduction, hydroformylation, and aromatic hydrogenation.[150–152] Recent studies show that Rh-based materials also can be quite effective for electrocatalytic reactions. For instance, Guo et al, reported a rhodium nanocrystal hybrid with single-walled carbon nanotubes (Rh/SWNTs), which showed excellent HER property with an overpotential of 48 mV at 10 mA cm^{-2}, and a Tafel slope of 27 mV dec^{-1} in 1 M KOH solution. Meanwhile, the Rh/SWNTs also displayed an OER activity, which was comparable to that of RuO_2. The high electrocatalytic performance was attributed to an electron polarization at the interface between Rh and SWNTs.[153]

In this chapter, to generalize the synthetic route explored in the Fe(np)/C work, noble metal species, such as Rh, were utilized during the preparation. Characterizations on morphology and composition of the obtained materials showed that noble metal (oxide) nanoparticles were also obtained with uniform dispersion on carbon layers. Their electrocatalytic performance for water electrocatalysis in alkaline medium was examined. This chapter was introduced with the permission from: M. Liu, F. Hof,

M. Moro, G. Valenti, F. Paolucci and A. Pénicaud. Carbon supported noble metal nanoparticles as efficient catalysts for electrochemical water splitting. Nanoscale, 2020, 12, 20165-20170.

4.2 Synthesis of materials

The synthesis of Rh and / or Pt-based nanomaterials was similar with the route to prepare Fe(np)/C, particularly the initial steps to produce graphenide solution. Figure 31 shows the step of reaction between graphenide solution and Rh and/or Pt salt(s) generating the final materials, denoted as Rh(np)/C, RhPt(np)/C, and Pt(np)/C, respectively. The "np" presents nanoparticle. The detailed synthetic process is explained in Appendix.

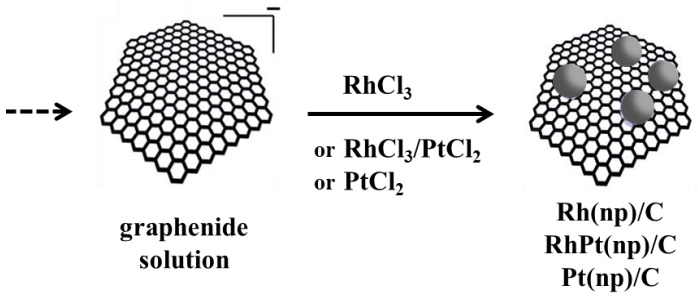

Figure 31 Scheme of the reaction between graphenide solution and Rh and/or Pt precursor(s)

4.3 Results and discussion

Physical characterizations

The crystalline nature of the prepared materials was shown by X-ray diffraction (XRD) patterns in Figure 32. Broad peaks at 26.1°, 39.9°, and 46.5° were displayed for the RhPt(np)/C and Pt(np)/C samples, which can be attributed to (002) plane of carbon, and (111) and (200) planes of metallic species. Although in the case of Rh(np)/C, only peak at 26.1° was visible, the existence of Rh species can be confirmed by other characterization techniques below.

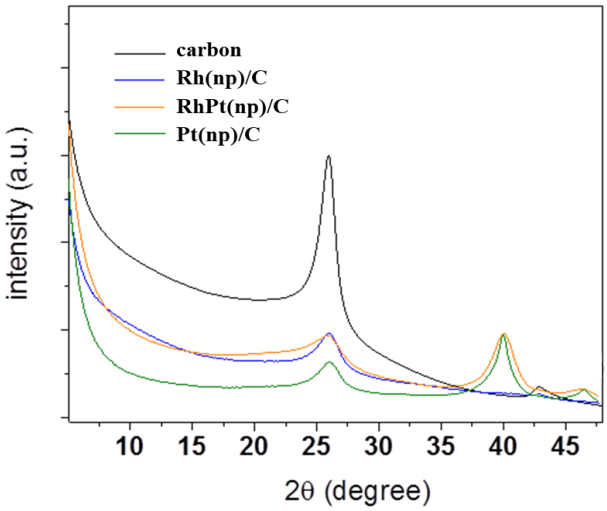

Figure 32 XRD patterns of carbon starting material (black trace), Rh(np)/C (blue trace), RhPt(np)/C (orange trace), and Pt(np)/C (green trace).

The presence of species of metallic nature in RhPt(np)/C and Pt(np)/C samples was further corroborated by X-ray photoelectron spectroscopy (XPS) measurements (Figure 33). In both cases, the peaks for metallic platinum were clearly visible with only a minor contribution of oxidized species. In contrast, for Rh(np)/C, peaks for Rh (III) were present, which can be attributed to Rh_2O_3. This observation might be explained by the less noble character of Rh metal and its oxidation in the work-up step.

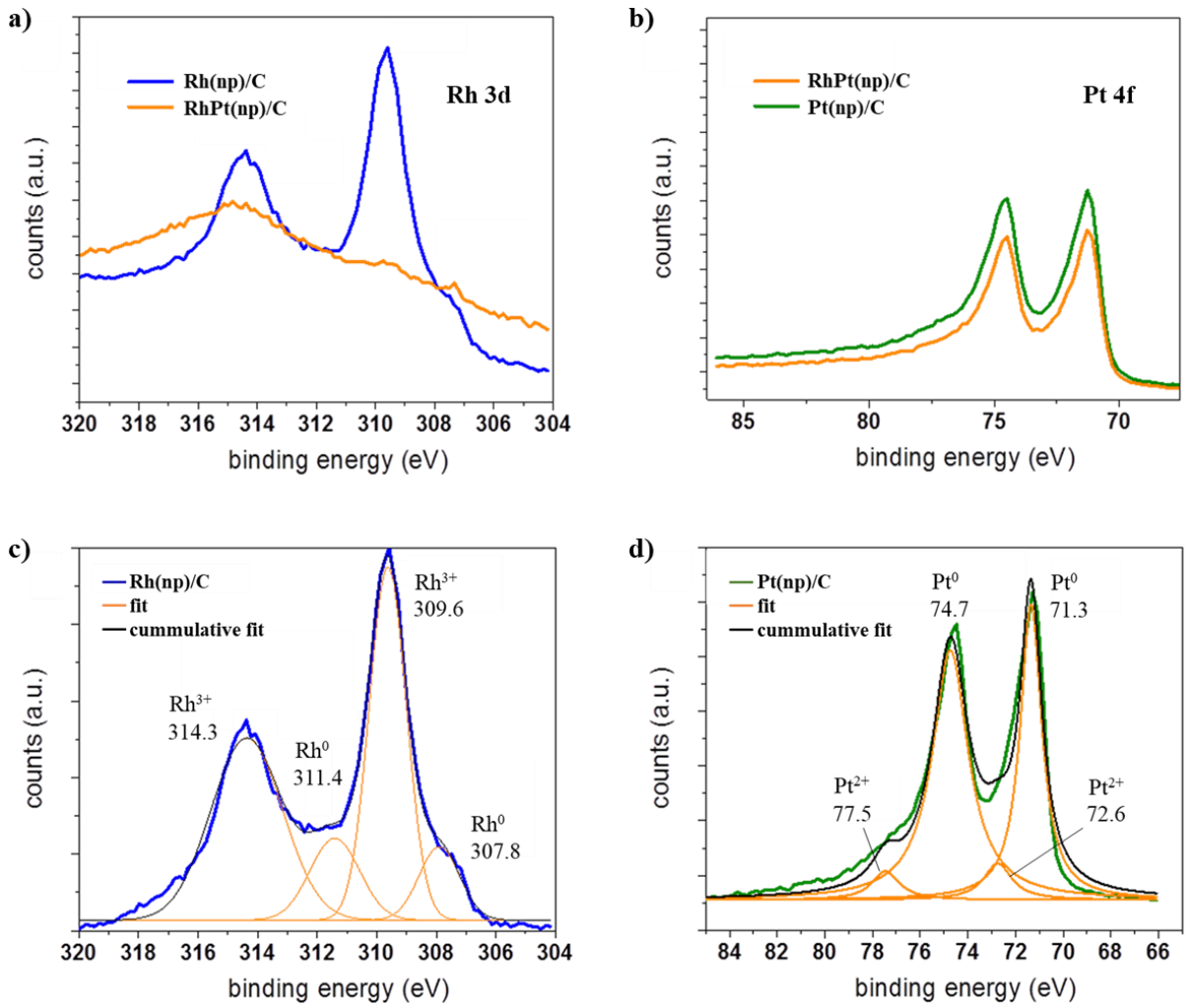

Figure 33 (a) Rh 3d XPS spectra of Rh(np)/C and RhPt(np)/C, and (c) corresponding fits. (b) Pt 4f XPS spectra of RhPt(np)/C and Pt(np)/C, and (d) corresponding fits.

Scanning Transmission Electron Microscopy (STEM) images supplied the morphology information of the prepared Rh(np)/C, RhPt(np)/C, and Pt(np)/C materials. As shown in Figure 34, nano size particles were finely distributed on carbon frameworks. And the corresponding Energy Dispersive X-Ray Spectroscopy (EDX) maps revealed that each metal element was detectable specially for the RhPt(np)/C considering that the presence of Rh was not very clear by XRD and XPS.

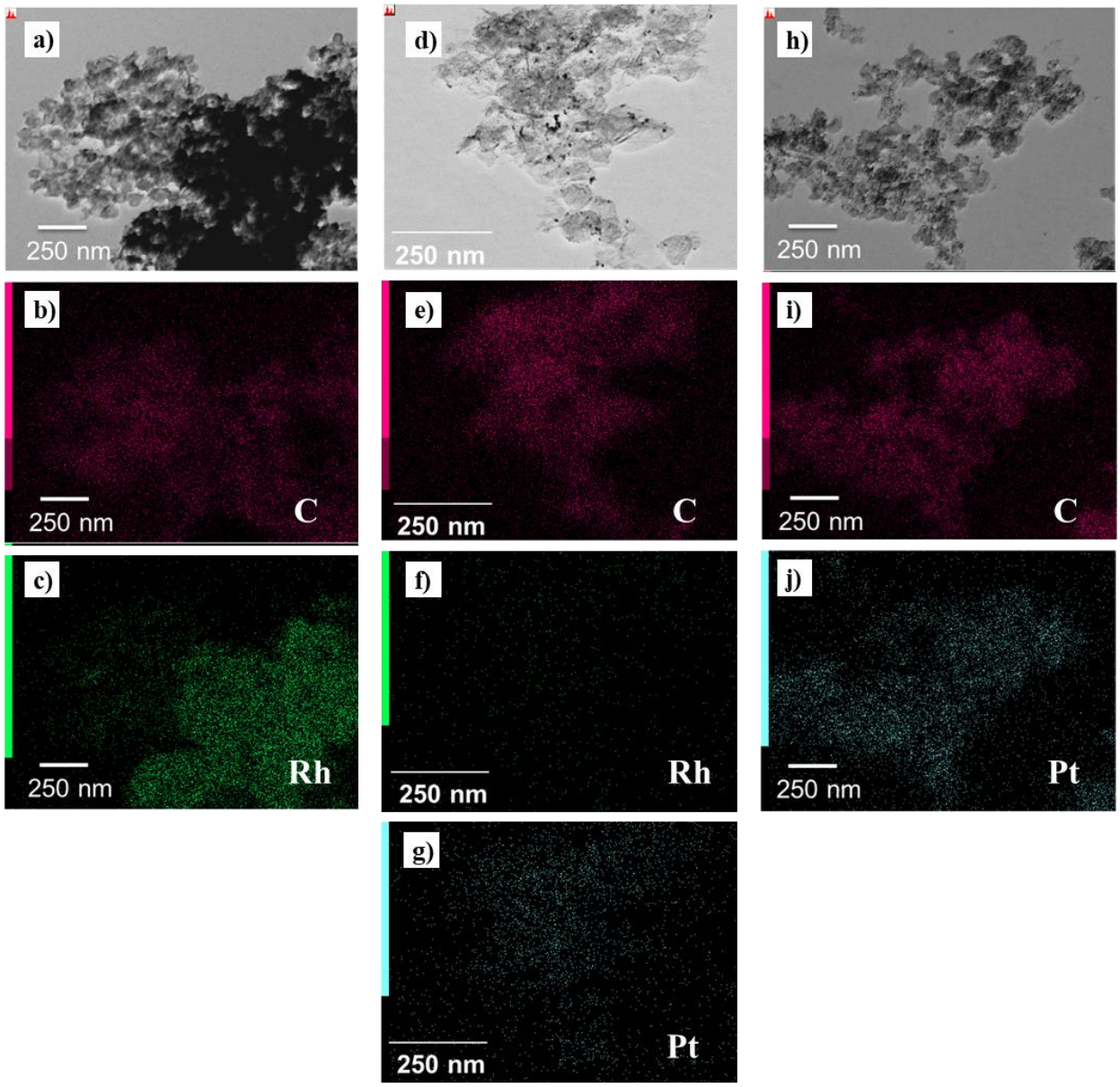

Figure 34 STEM images and corresponding EDX maps of Rh(np)/C (a, b, and c), RhPt(np)/C (d, e, f, and g), and Pt(np)/C (h, i, and j).

Transmission Electron Microscopy (TEM) images (Figure 35) further confirmed the crystalline nature of the nanoparticles. Moreover, from the TEM images, the size distribution of the nanoparticles was identified to be in a range between 2 and 3 nm (Figure 36). The size of nanoparticles in the RhPt(np)/C sample was assumed to be similar as XRD peak shapes of RhPt(np)/C and Pt(np)/C were quite close, and STEM images could also give some supporting information.

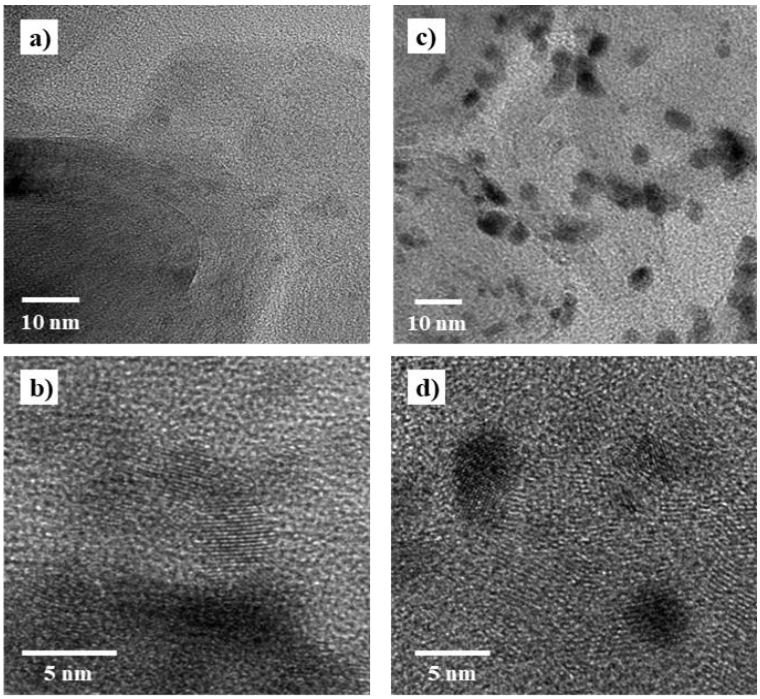

Figure 35 TEM images of Rh(np)/C (a, b) and Pt(np)/C (c, d) at lower and higher magnifications.

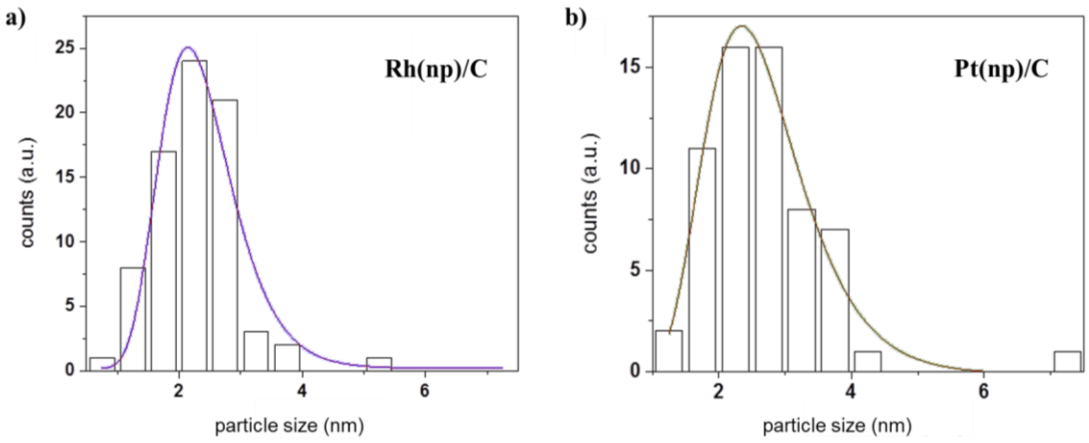

Figure 36 The distribution of nanoparticle size for (a) Rh(np)/C and (b) Pt(np)/C based on the analysis of about 20 TEM images, and the size measurements of 77 nanoparticles for the former and 62 nanoparticles for the latter case.

The metal contents in the obtained materials were examined by Thermogravimetric analysis (TGA). As can be seen in Figure 37, the remaining masses of Rh(np)/C, RhPt(np)/C, and Pt(np)/C samples were 26.9%, 22.1%, and 27.2%, respectively.

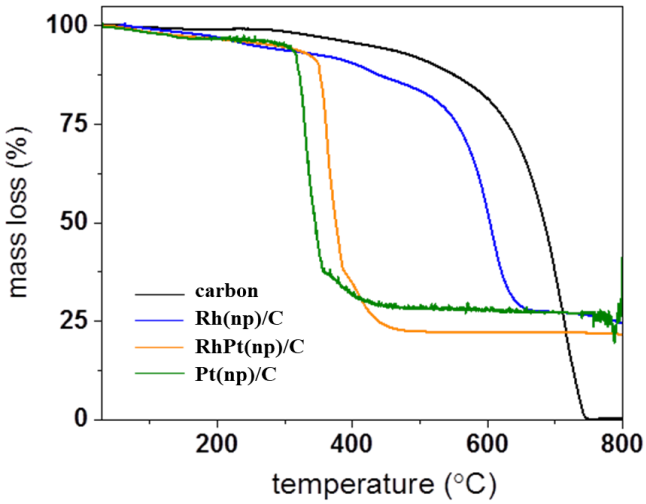

Figure 37 TGA measurements of the carbon starting material, Rh(np)/C, RhPt(np)/C, and Pt(np)/C in synthetic air (80% N_2, 20% O_2) between 50-800 °C with a heating ramp of 10 °C / min.

Electrochemical measurements

So far, it has been shown that by tuning the metal species from non-noble transition metal to Rh and / or Pt, very small size of Rh (oxide), RhPt, Pt nanoparticles finely dispersed on carbon frameworks were obtained. The prepared materials then were utilized as catalysts for electrochemical water splitting, i.e., oxygen evolution reaction (OER) and hydrogen evolution reaction (HER).

The electrocatalytic activities of Rh(np)/C, RhPt(np)/C, and Pt(np)/C for OER were tested in an Ar saturated 0.1 M aqueous KOH solution by loading materials on a rotating disk electrode (RDE) in order to remove O_2 generated on the electrode. As shown in the linear sweep voltammetry (LSV) curves (Figure 38), the onset potentials of Rh(np)/C and commercial RuO_2 were almost identical, clearly less positive than RhPt(np)/C and Pt(np)/C. And the activity of Rh(np)/C kept comparable to

RuO_2 as the anodic sweeping of electrode potential continued, while the activity of RhPt(np)/C was relatively inferior, and Pt(np)/C only showed weak catalytic activity. For instance, to reach a current density of 5 mA cm^{-2}, the required overpotentials for commercial RuO_2, Rh(np)/C, RhPt(np)/C, and Pt(np)/C were 328 mV, 330 mV, 414 mV, and 555 mV, respectively. To reach a current density of 10 mA cm^{-2}, the Rh(np)/C sample showed an overpotential of 371 mV, which was only 10 mV more than that of commercial RuO_2. Meanwhile, the Tafel slopes of commercial RuO_2, Rh(np)/C, RhPt(np)/C, and Pt(np)/C were 68 mV dec^{-1}, 88 mV dec^{-1}, 94 mV dec^{-1}, and 151 mV dec^{-1}, respectively.

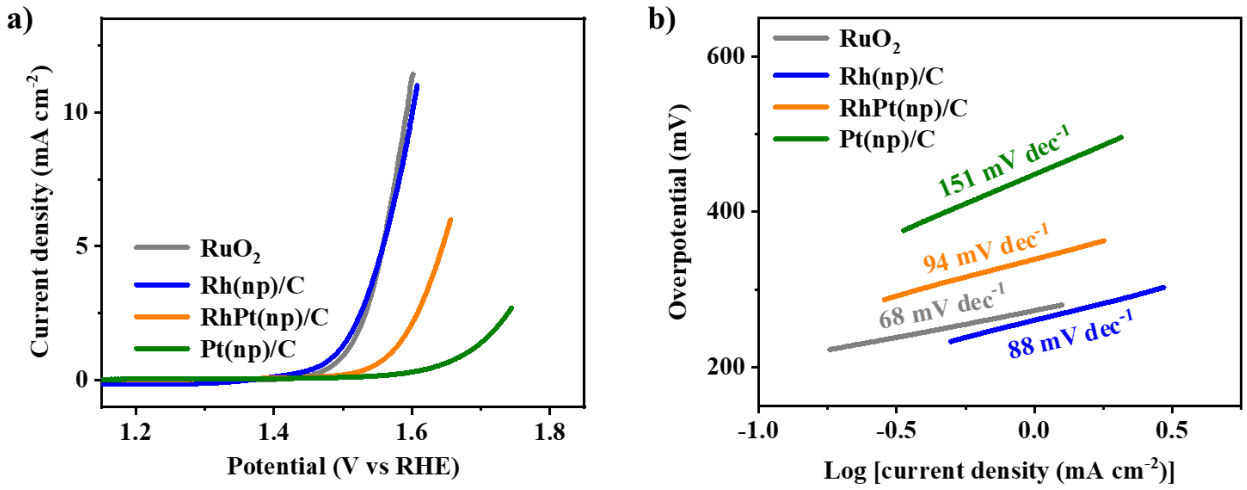

Figure 38 (a) LSV curves of commercial RuO_2, Rh(np)/C, RhPt(np)/C, and Pt(np)/C for OER at a scan rate of 5 mV s^{-1} under a rotation speed of 1600 rpm in Ar saturated 0.1 M aqueous KOH solution. (b) Corresponding Tafel plots.

Then, turnover frequency (TOF) values of the Rh(np)/C sample for OER at different overpotentials were investigated by performing several potential steps. The method was adapted from a former work of our research group.[154] The idea was that the charges transferred during each potential step could be converted to the moles of oxygen evolved, and TOF values were calculated accordingly assuming that every single metal atom was active. Thus, the obtained TOF values were the lower limits considering that not all of the sites actually were active and equally accessible to reactants. The

chronoamperometric responses were collected and shown in Figure 39. The TOF values were calculated to be 0.013 s^{-1}, 0.019 s^{-1}, and 0.026 s^{-1} at overpotentials of 318 mV, 336 mV, and 354 mV, respectively. A comparation of TOF values of several highly effective electrocatalysts for OER was shown in Table 4, which to some extent indicated that the prepared Rh(np)/C was very promising for OER electrocatalysis.

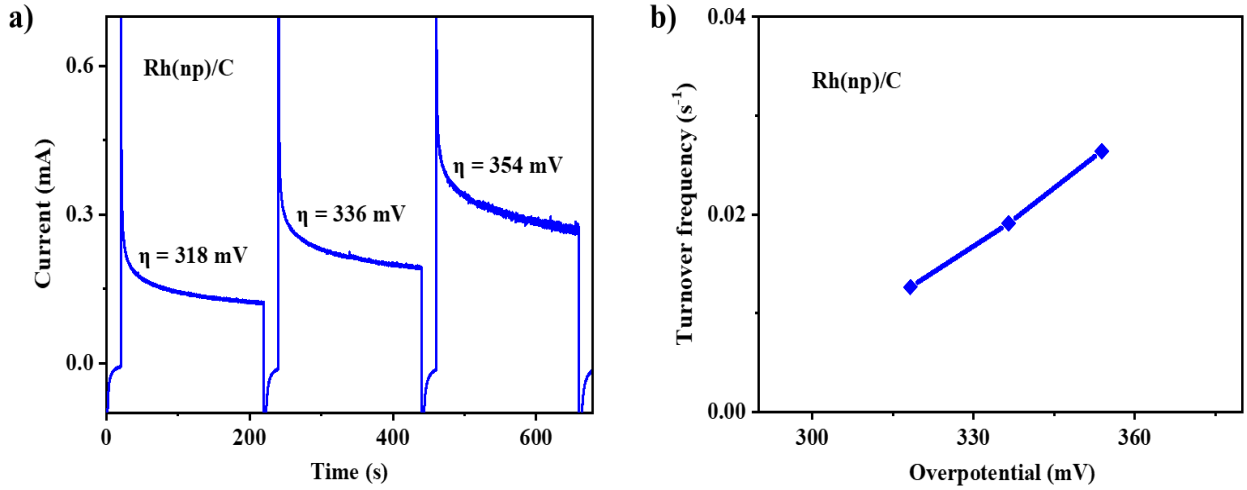

Figure 39 (a) chronoamperometric curves of Rh(np)/C for OER at overpotentials of 318 mV, 336 mV, and 354 mV, respectively. (b) corresponding TOF values.

Table 4 Comparison of TOF values of different electrocatalysts for OER

Catalyst	Electrolyte (aqueous KOH)	Loading amount (mg cm_{geo}^{-2})	OER TOF (s^{-1}) at specific overpotential	Ref.
RuO_2	0.1	0.24	0.013 at 365 mV	[59]
$CoCr_2O_4$/CNS	0.1	0.24	0.031 at 365 mV	[59]
IrO_2	1.0	0.21	0.01 at 300 mV	[64]
NiFe LDHs	1.0	0.07	0.05 at 300 mV	[64]
RuO_2	0.1	0.2	0.01 at 350 mV	[155]

Catalyst	Electrolyte (aqueous KOH)	Loading amount (mg cm_{geo}^{-2})	OER TOF (s^{-1}) at specific overpotential	Ref.
α-$Ni(OH)_2$	0.1	0.2	0.036 at 350 mV	[155]
RuO_2	0.1	0.24	0.01 at 350 mV	[146]
Fe_1Co_1-ONS	0.1	0.36	0.022 at 350 mV	[156]
Rh(np)/C	0.1	0.42	0.026 at 354 mV	This work

Besides, the stabilities of commercial RuO_2, the prepared Rh(np)/C, RhPt(np)/C, and Pt(np)/C for OER were investigated by conducting chronopotentiometry measurements at a current density of 2 mA cm^{-2} in Ar saturated 0.1 M aqueous KOH solution under a rotation speed of 1600 rpm. As shown in Figure 40, all the samples did not show much increase of the electrode potential after 2000 seconds OER electrocatalysis. Unfortunately, the stability test was limited to that long because the O_2 generated on the electrode surface could not be timely removed even though the electrode was already under rotation.

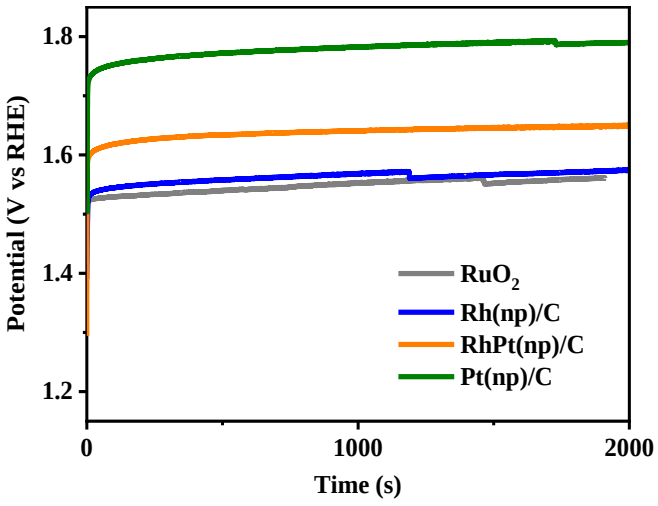

Figure 40 Chronopotentiometry curves of commercial RuO_2, Rh(np)/C, RhPt(np)/C, and Pt(np)/C for OER at a current density of 2 mA cm^{-2} in Ar saturated 0.1 M aqueous KOH solution under a rotation speed of 1600 rpm.

On the other side, the electrocatalytic activities of the prepared Rh(np)/C, RhPt(np)/C, and Pt(np)/C for hydrogen evolution reaction (HER) were evaluated in Ar saturated 0.1 M aqueous KOH solution by loading the material on a glassy carbon electrode while keeping stirring the solution with a magnetic stirrer. As shown in the linear sweep voltammetry (LSV) curves (Figure 41), although the onset potentials for all the samples were almost identical, the current densities came to separate as the potential swept negatively. To reach a current density of 2 mA cm^{-2}, the required overpotentials of the Rh(np)/C, RhPt(np)/C, Pt(np)/C, and commercial Pt/C were 44, 48, 82 mV, and 90 mV, respectively. And, to reach a current density of 10 mA cm^{-2}, the overpotential needed for Rh(np)/C was 71 mV. Based on the LSV curves, Tafel slopes were calculated in order to study the kinetics of HER, which were 50 mV dec^{-1}, 52 mV dec^{-1}, 84 mV dec^{-1}, and 88 mV dec^{-1} for Rh(np)/C, RhPt(np)/C, Pt(np)/C, and commercial Pt/C (20wt%), respectively, indicating that HER went through Volmer-Heyrovsky steps on the catalyst surface. Some selected metal-carbon composite materials as electrocatalysts for HER were present in Table 5.

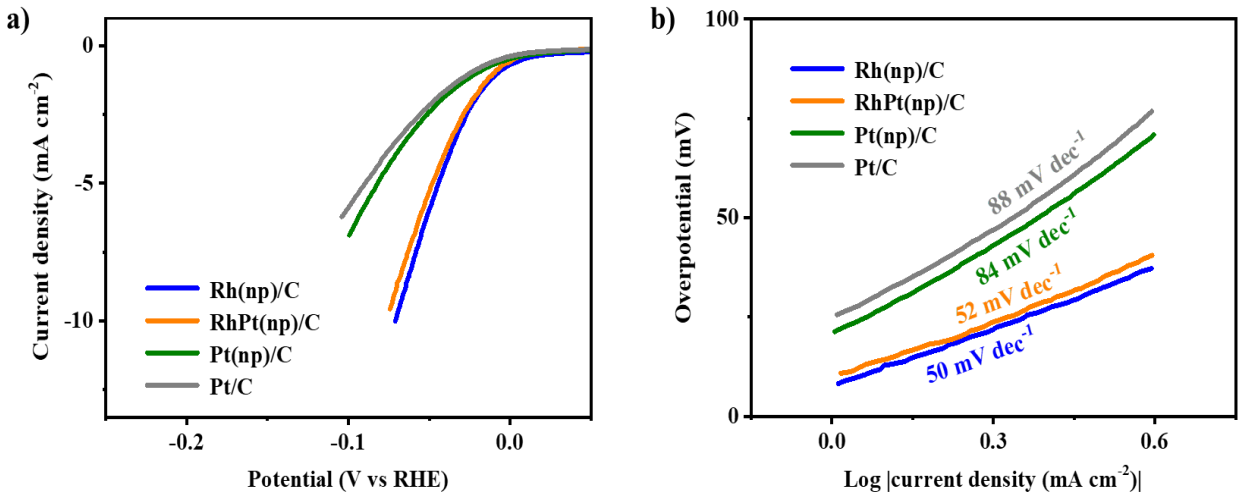

Figure 41 (a) LSV curves of Rh(np)/C, RhPt(np)/C, Pt(np)/C, and commercial Pt/C (20wt%) a scan rate of 5 mV s^{-1} in Ar saturated 0.1 M aqueous KOH solution. (b) Corresponding Tafel plots.

Table 5 Selected summary of metal-carbon composite materials as electrocatalysts for HER in alkaline medium.

Catalyst	Electrolyte (aqueous KOH)	Loading amount (mg cm_{geo}^{-2})	HER Overpotential (mV) at 10 mA cm^{-2}	HER Tafel slope (mV dec^{-1})	Ref.
RuCo/NC	1 M	0.28	28	31	[28]
NiO/Ni-CNT	1 M	0.4	80	82	[157]
Mo_2C@N-C	1 M	0.28	60	-	[158]
CoP/rGO-400	1 M	0.28	150	38	[70]
RuPx@NPC	1 M	0.2	74	70	[159]
Co@Ir/NC-10%	1 M	0.2	121	97.6	[160]
IrCo@NC-500	1 M	0.28	45	80	[161]
5.0% F-Ru@PNC-800	0.1 M	0.28	30	28.5	[162]
CoRu@NCs	1 M	0.273	45	66	[163]
$FePSe_3$/NC	1 M	0.212	118	88	[164]
Co/β-Mo_2C@N-CNT	1 M	0.2	170	92	[165]
Fe_2O_3/Fe@CN	1 M	0.28	330	114	[166]
Rh(np)/C	0.1 M	0.42	71	50	This work

In addition, a facile two-electrode water electrolyzer was set up using Rh(np)/C (loaded on glassy carbon electrode) as both anode and cathode to investigate the whole water splitting in Ar saturated 0.1 M aqueous KOH solution. As shown in Figure 42, for this water electrolyzer with Rh(np)/C || Rh(np)/C couple electrodes, the voltage required to achieve a current density of 10 mA cm^{-2} was 1.68 V, which matched well with the potential difference between HER and OER obtained in three-electrode system.

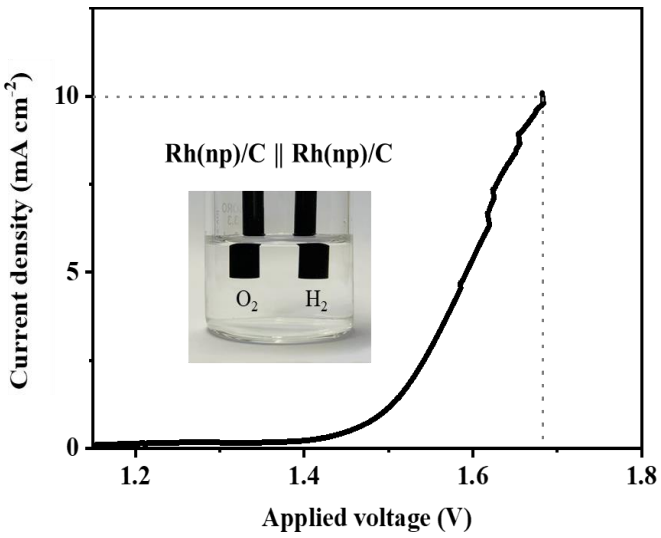

Figure 42 LSV curves of a facile two-electrode water electrolyzer with RhPt(np)/C couple electrodes (both anode and cathode) a scan rate of 5 mV s^{-1} in Ar saturated 0.1 M aqueous KOH solution. The inset showed an optical photograph of the two-electrode system.

Moreover, to better understand the RhPt(np)/C sample, Rh(np)/C and Pt(np)/C were physically mixed together (with a ratio of 1:1), and the electrocatalytic performances of this Rh-Pt mixture for OER and HER were investigated. As shown in Figure 43, though the onset potentials of RhPt(np)/C and Rh-Pt mixture for OER were very similar, Rh-Pt mixture displayed lower current densities at same overpotentials and larger Tafel slope than RhPt(np)/C. This result was also found when they were used for HER electrocatalysis (Figure 44). The increased performance of RhPt(np)/C over Rh-Pt mixture

counterpart suggested that there might be a combination between Rh and Pt species inside the RhPt(np)/C sample.

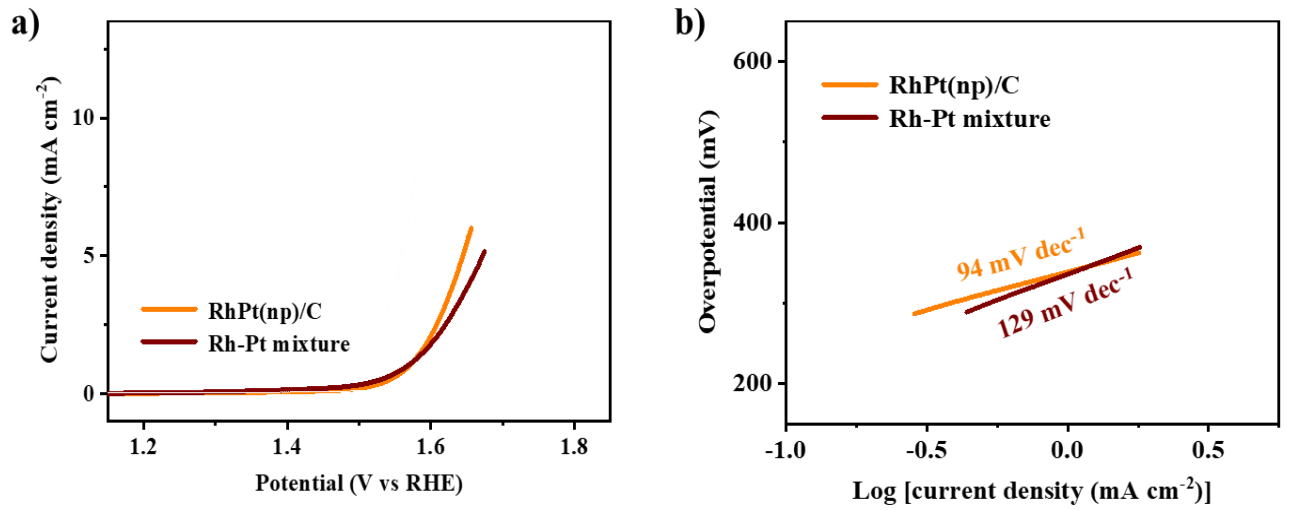

Figure 43 (a) LSV curves of RhPt(np)/C and Rh-Pt mixture for OER at a scan rate of 5 mV s^{-1} under a rotation speed of 1600 rpm in Ar saturated 0.1 M aqueous KOH solution. (b) Corresponding Tafel plots.

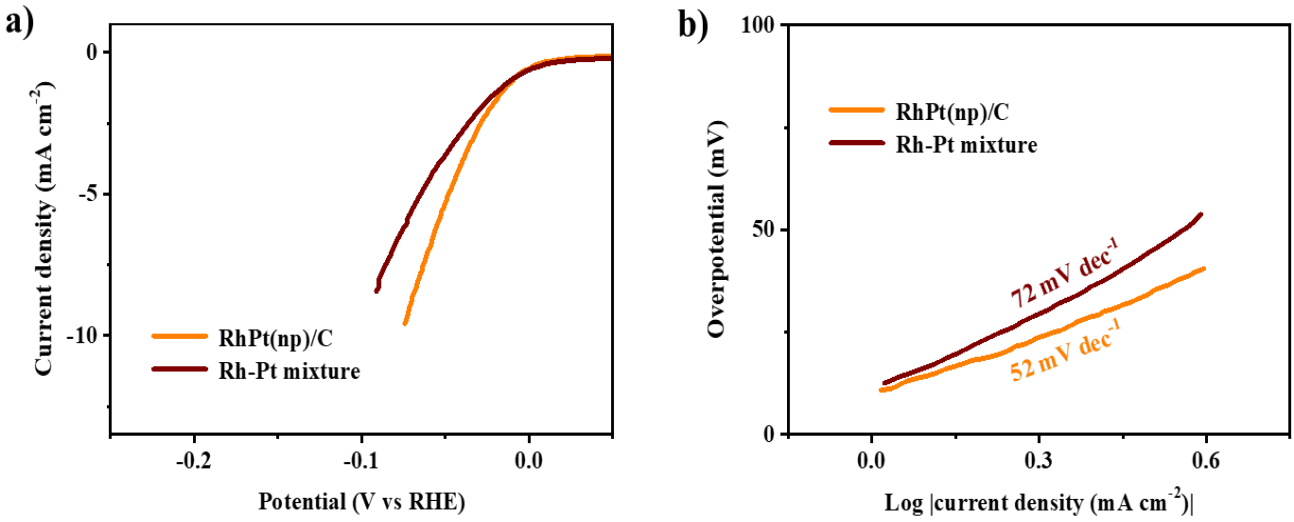

Figure 44 (a) LSV curves of RhPt(np)/C and Rh-Pt mixture for HER a scan rate of 5 mV s^{-1} in Ar saturated 0.1 M aqueous KOH solution. (b) Corresponding Tafel plots.

To conclude, noble metal-based nanomaterials, including Rh (oxide), RhPt, and Pt nanoparticles / carbon composite materials, were synthesized, and dispersed well on carbon supports. Therefore, the synthetic route used was demonstrated to be a general process of preparing carbon supported nanomaterials. In terms of electrocatalytic performance for water splitting in alkaline solution, Rh(np)/C displayed excellent OER activity, which was comparable to commercial RuO_2, while all the three samples especially Rh(np)C showed better HER activity than benchmark catalyst Pt/C. The good catalytic performance can be attributed to: a) improved numbers of active sites due to the small size of catalysts and good dispersion of nanoparticles on carbon supports, and b) the synergetic chemical coupling effects between catalysts and supports.

Chapter 5 Carbon-supported noble metal and non-noble metal mixed nanoparticles for electrocatalysis of HER

5.1 Introduction

Hydrogen fuel is considered as one of the alternatives to fossil fuels for future energy supply. Electrocatalytic hydrogen evolution reaction (HER) has been the subject of extensive studies over the past decade. Pt group metal-based materials are known as the most efficient catalysts for HER due to their optimum hydrogen binding energy.[167] However, the high cost and low abundance of Pt group metals restrict their wide application to produce H_2. Hence, reducing noble metal loading and/or replacing them with earth abundant and non-noble metal alternatives with high catalytic properties and stabilities is of great importance for developing the hydrogen economy.

One of the approaches is alloying noble metal with earth abundant metals. For instance, Pt-Co alloy nanoparticles encapsulated in the matrix of carbon nanofibers with a low Pt loading (~5 wt%) were prepared by the aid of an electrospinning and carbonization strategy, and the obtained catalyst demonstrated a high catalytic activity toward HER, almost comparable to Pt/C.[21] 3D Pt-Co nanoparticles encapsulated in carbon nanorod arrays (Pt_2Co_8/N-C) have been prepared on carbon cloth by a facile galvanic replacement reaction route, and reported to possess high catalytic activity due to the lattice contraction and downshift of d-band center.[26] Markovic et al. have reported a controlled arrangement of nanometer scale $Ni(OH)_2$ clusters on Pt, where $Ni(OH)_2$ was supposed to have a synergistic effect with Pt to cleave the HO-H bond.[168]

Although some catalysts have already showed similar HER activity to commercial Pt/C, it is still challenging to surpass that. A synthesis of phase and interface-engineered Pt-Ni nanowires through a

simple post annealing strategy under a controlled atmosphere has been reported, which exhibited a quite low overpotential of 40 mV at the current density of 10 mA cm^{-2} in 1.0 M KOH. The authors discovered that unfilled d-orbitals of Ni^{x+} could lead to a stronger electrostatic affinity with OH^- than Pt, and thus the NiO_x could accelerate the water dissociation generating H_2. The extraordinary activity benefited from the tailored interfaces and phases between Pt_3Ni and NiO_x.[24] Moreover, the catalytic activity and stability of noble metal-based catalysts can be further improved by forming core-shell structures, which generally can be obtained by chemical leaching or electrochemical dealloying of the non-noble element in a catalyst, or by electrochemical deposition techniques, such as galvanic displacement.[169,170]

In the former chapters, it has already been identified that either non-noble metal or noble metal nanoparticles could be obtained through the synthetic route explored in this thesis. Then it would be expected if that works with mixed metal precursors of noble and non-noble metals so that the amount of noble metal in the catalyst can be reduced. In this chapter, carbon supported bimetallic NiPt nanoparticles composite material and its Ni and Pt nanoparticles counterparts were prepared by the same synthetic route. Electrocatalytic activity of the obtained nanomaterials for HER in alkaline solution was investigated.

5.2 Synthesis of materials

The synthesis of carbon supported NiPt bimetallic nanoparticles and Ni nanoparticles composite materials was similar with the route used to prepare Fe(np)/C, Rh(np)/C, etc., as shown in Figure 45.

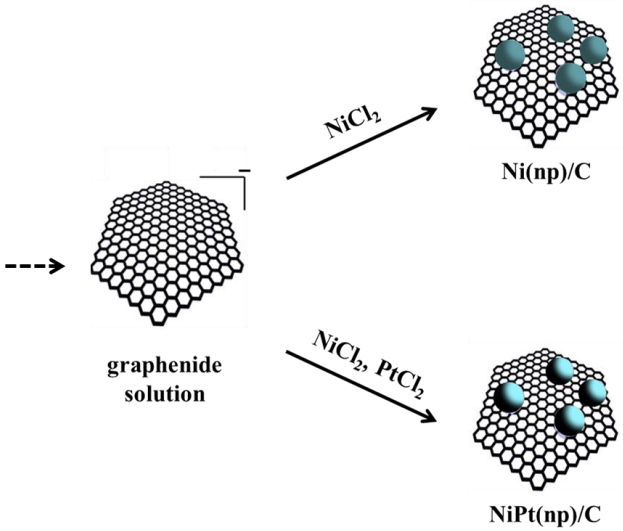

Figure 45 Scheme of the synthesis of carbon supported Ni and NiPt nanoparticles composite materials.

5.3 Results and discussion

Physical characterizations

The crystalline structures of the prepared Ni(np)/C and NiPt(np)/C composite materials were demonstrated by XRD patterns. As shown in Figure 46, for the Ni(np)/C sample, diffraction peaks corresponded to the (111) and (220) planes of NiO, and the (001), (100), and (101) planes of $Ni(OH)_2$, respectively, can be identified[136], indicating the state of Ni(II) in the composite materials. For the NiPt(np)/C sample, only diffraction peaks associated with Pt was clear, but it would not be pure Pt component, which will be confirmed by electrochemical measurement result. In addition, the mass ratios of metal (oxide) in the composite materials were evaluated by TGA in synthetic air. The values were 22.6 wt% for Ni(np)/C, and 27 wt% NiPt(np)/C, respectively.

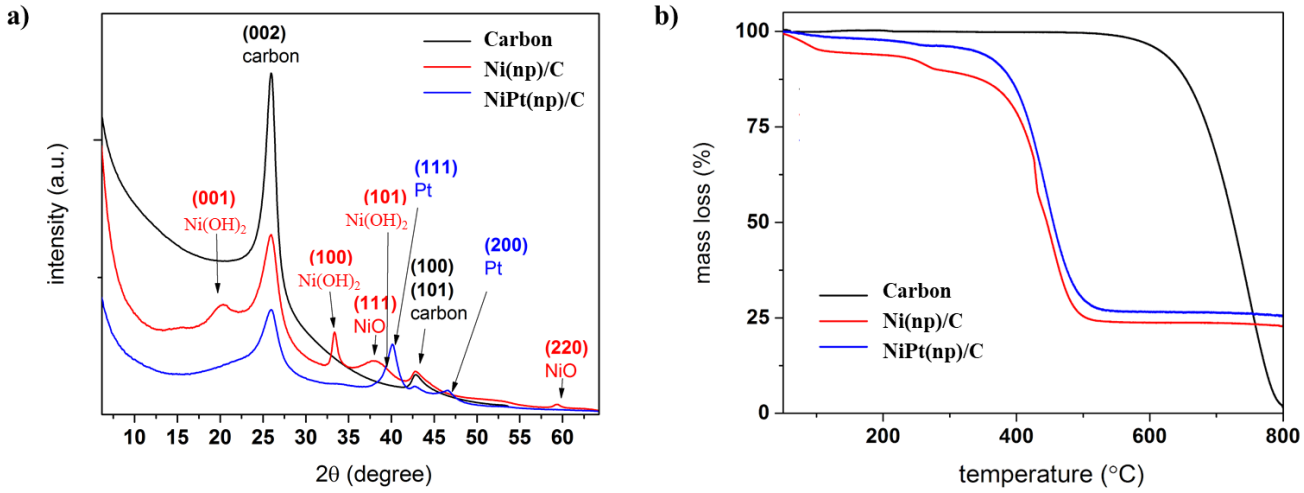

Figure 46 a) XRD patterns, b) TGA measurements in synthetic air (80% N_2, 20% O_2) between 30-800 °C for starting carbon, Ni(np)/C, and NiPt(np)/C.

Electrochemical measurements

Firstly, CVs at different potential scan rates were performed. As shown in Figure 47, peak associated with Ni^{2+}/Ni^{3+} redox can be clearly seen, which confirmed that the prepared material, NiPt(np)/C, was not pure Pt component. The cathodic peak current was correlated with the scan rate by:

$$i_p = \frac{FQ}{4RT}v$$

where F is the Faraday constant, Q is charge transferred, R is the ideal gas constant, T is room temperature, and v is scan rate.

According to calculation, the value of mole of Ni in the deposition (25 μg) was 13.02 nmol. Notice that for the quantification of Ni, the material fully reduced during cathodic scan was considered.

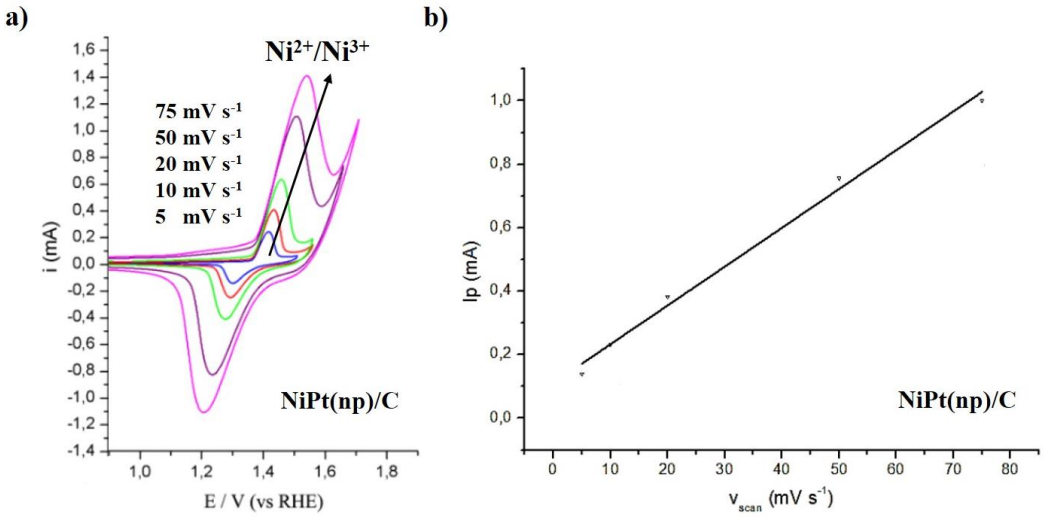

Figure 47 (a) CV curves of NiPt(np)/C at scan rates of 5, 10, 20, 50, and 75 mV s^{-1} in 0.1 M KOH solution. Peaks around 1.2 V to 1.5 V (vs RHE) were assumed to be Ni^{2+}/Ni^{3+} redox. (b) linear relationship between cathodic peak current and scan rate.

The electrocatalytic activities of the prepared Ni(np)/C and NiPt(np)/C for HER were evaluated in Ar saturated 0.1 M aqueous KOH solution. As shown in the linear sweep voltammetry curves (Figure 48), for Ni(np)/C sample, HER occurred at a potential of ~150 mV, while NiPt(np)/C showed a negligible onset potential, which is characteristic for noble metal-based materials. To reach a current density of 10 mA cm^{-2}, the required overpotentials of Ni(np)/C and NiPt(np)/C were >450 mV and 230 mV, respectively. Meanwhile, the Tafel slope of NiPt(np)/C was slightly lower than Ni(np)/C. A comparation with Pt(np)/C (the HER performance of which has been present in Chapter 4) was shown in Table 6. It can be seen that the electrocatalytic activity of NiPt(np)/C was significantly improved towards Pt(np)/C. Note that the prepared NiPt(np)/C owned an advantage of lower amount of Pt.

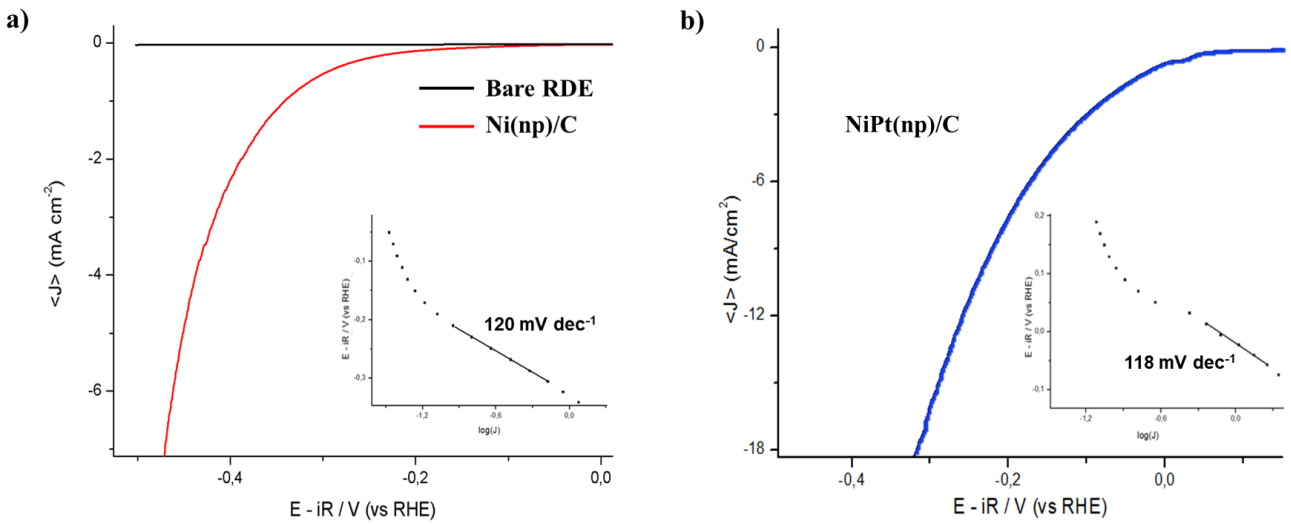

Figure 48 LSV curves at a scan rate of 5 mV s^{-1} in Ar saturated 0.1 M aqueous KOH solution (and corresponding Tafel plots, the inset) of (a) Ni(np)/C, and (b) NiPt(np)/C.

Table 6 Comparation of electrocatalytic HER performance of nanomaterials studied in this thesis.

Catalyst	Electrolyte pH	Loading amount (mg cm_{geo}^{-2})	HER Overpotential (mV) at 10 mA cm^{-2}	HER Tafel slope (mV dec^{-1})
Ni(np)/C	13	0.35	>450	120
NiPt(np)/C	13	035	~230	118
Pt(np)/C	13	0.42	~125	84

In addition, the stabilities of Ni(np)/C and NiPt(np)/C for HER were investigated by conducting chronoamperometry measurements at overpotentials of 330 mV and 50 mV, respectively, in Ar saturated 0.1 M aqueous KOH solution. The corresponding current density would be around 1 mA cm^{-2}. As shown in Figure 49, the current did not show much decrease for both samples after around 1 h HER electrocatalysis.

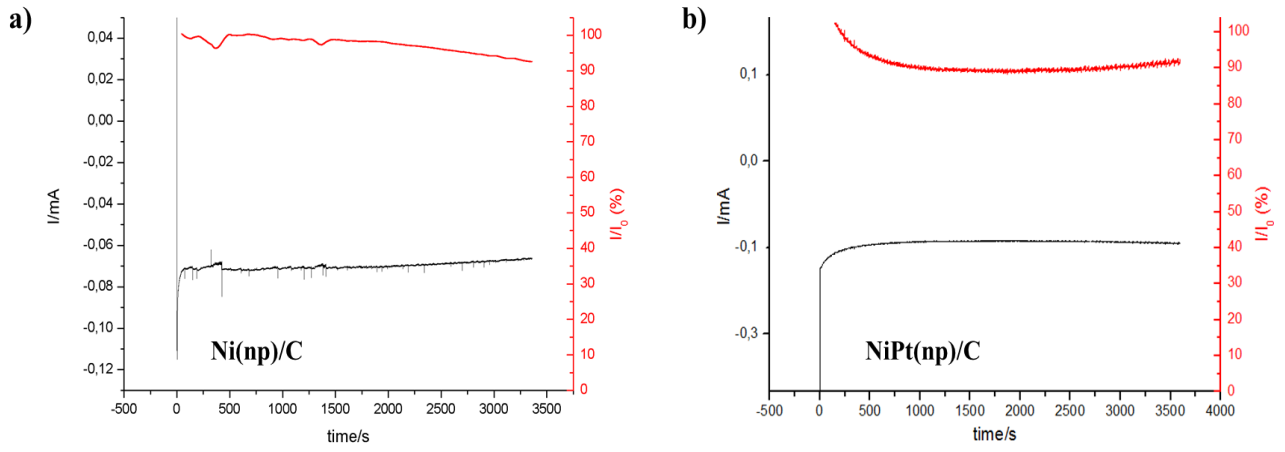

Figure 49 Chronoamperometry curves of (a) Ni(np)/C and (b) NiPt(np)/C for HER in Ar saturated 0.1 M aqueous KOH solution at overpotentials of 330 mV and 50 mV, respectively. (In this case, the current density was kept around 1 mA cm^{-2} for both)

The above results showed that compared with non-noble metal (Ni)-based nanomaterial, introducing noble metal to forming bimetallic (NiPt) nanoparticle indeed greatly improved the electrocatalytic performance. Although the NiPt / carbon composite still could not reach or pass the activity of Pt alone, which needs more efforts in the future to better understand, it is promising since the amount of noble metal in the catalyst was decreased.

So far, a systematic investigation of a general synthetic route for preparing carbon-supported nanomaterials and their application in electrocatalysis has been performed. Beside these works, during my third year of PhD, I visited Prof. Asefa's research laboratory at Rutgers University, USA for three months under Marco Polo program. Some initial work on the synthesis of nanoporous carbon-supported metal nanoparticles was conducted.

Porous carbon materials generally can be classified as macroporous (pore size > 50 nm), mesoporous (2 nm ≤ pore size ≤ 50 nm), microporous (pore size ≤ 2 nm), and hierarchically porous carbons with ordered/disordered porosities and graphitic/amorphous textures. Due to significant properties like large specific surface areas and pore volumes, unique morphologies, controllable porous structures, and excellent chemical stabilities, porous carbon materials have been attractive in environmental and energy-related fields, such as water purification, gas adsorption and separation, energy conversion and storage, catalysis.[171–174] There are many reports suggesting the application of porous materials for catalysis. Depending on their structures/chemical compositions, some of them may directly be used as heterogeneous catalysts, while others can serve as host materials for catalytic active species. For ORR electrocatalysis, abundant micropores supply large specific surface areas that enable the exposure of active sites, while mesopores and macropores facilitate the transport of ORR-related species in the catalyst layer. It has been confirmed that suitable incorporation of heteroatoms (such as N, S, B, and P) in carbon materials can create active sites by means of changing the composition, microstructure, surface electrochemical property, and electronic structure.[175] For example, pyridinic N doped at the edge of graphitic C can reduce energy barrier for oxygen adsorption, and promote rate-limiting first electron transfer.[176] Multiple heteroatoms doping could further facilitate the electrocatalytic activity thanks to the synergistic effects of different heteroatoms on the charge density of carbon.[177]

Porous carbon materials with large specific surface area can also be used as supports for loading metals in order to achieve better ORR performance.[178] For example, Fe, N-doped and Co, N-doped porous carbon catalysts have been investigated.[179] And, it is promising to modify physicochemical properties of porous carbons to make them comparable to Pt/C or even better, therefore accelerating the practical applications in energy conversion and storage. Transition metal-based materials, such as nitrides, phosphides, sulfides, and selenides, have been studied as promising electrocatalysts. However, they are still left behind in activity and durability compared with noble metal-based catalysts. Transition metal-based particles generally suffer from aggregation and thus loss of surface area and active sites. A typical solution is to load transition metal particles on carbon materials. Porous materials enable the synthesis of catalytically active supported metallic nanoparticles within their pores. Meanwhile, they allow the nanoparticles confined in their pores to remain stable (not aggregate or lose their catalytic activities).

As shown in Figure 50, the synthesis involved firstly deposition of metal nanoparticles on silica colloidal crystals. Then, polyaniline (PANI) was filled in the interstice of silica, followed by carbonization at high temperature. Afterwards, the silica templates were etched off to obtain the final materials. (Detailed information on synthesis was shown in appendix part). Silica nanoparticles were used as templates in order to render the carbon support materials high porosity and large surface area so that the catalysts can have better diffusion pathways for the reactants, and thus display better catalytic activity. PANI was purposely chosen as carbon precursor since it has a high N/C atomic ratio, and can generate a relatively high yield of N-dopant species in the carbon materials upon pyrolysis.

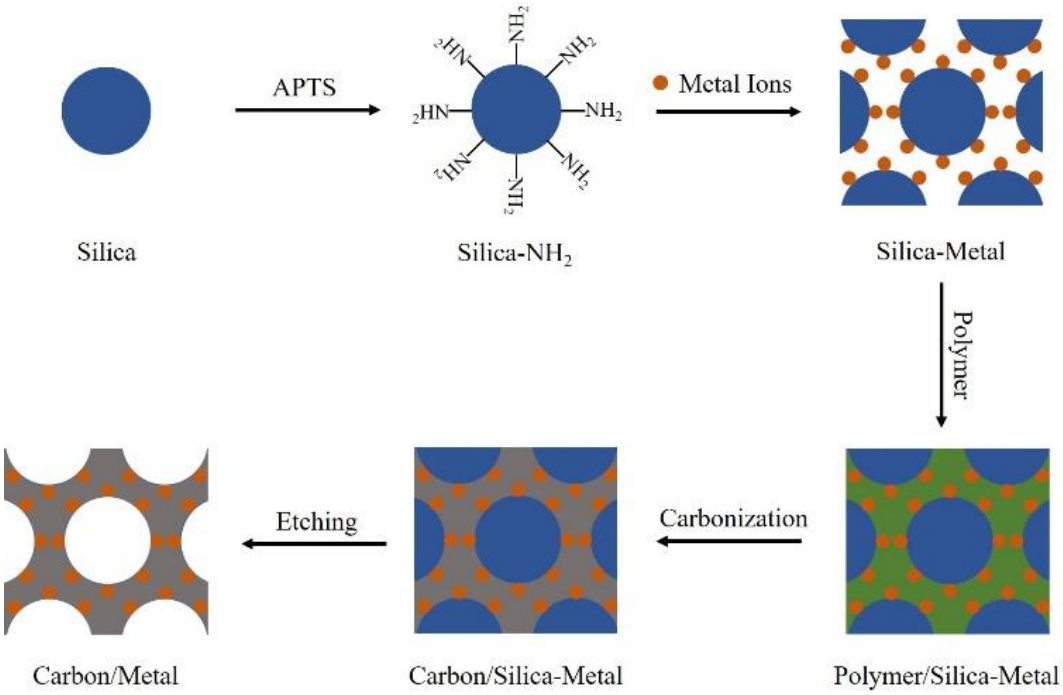

Figure 50 Synthetic procedure of nanoporous carbon-supported metal nanoparticles

More works are needed to be done: first, the optimum approach of synthesis is required to be further explored. For instance, some experimental factors, such as silica size, metal species, polymer amount, and carbonization temperature, which may have effects on the final product, and thus affect electrocatalytic properties, are needed to be studied. Second, to confirm what exactly have been prepared and what the morphologies would be like, physical characterizations, such as XRD, TGA, SEM, and N_2-adsorption/desorption experiments, are required. Moreover, the electrocatalytic performance towards electrochemical reactions, such as OER and HER, needs to be measured.

Conclusion

This PhD project focused on exploring effective electrocatalysts for reactions during energy conversion processes, particularly in alkaline water electrocatalysis and fuel cells.

Nanomaterials combining with carbon supports caught the attentions since they benefit from increased number of active sites. Therefore, a synthetic route of preparing carbon-supported nanoparticles was explored based on the reaction between graphenide solution and metal precursors, where graphenide solution produced from potassium intercalation into graphite worked as reduction agent. It was revealed that the size of nanoparticles could be controlled by using different starting graphite materials, and had a significant effect on the electrocatalytic activities.

More importantly, the synthetic route was demonstrated to be a general approach, i.e., the metal precursor can be flexibly tuned, from non-noble metal to noble metal and from single metal to bimetals. In each case, nanoparticles with a diameter of several nanometers were obtained and finely dispersed on carbon supports. This renders the prepared materials a couple of advantages, such as enhanced specific surface area, synergetic chemical coupling effects, and improved stability. Depending on the type of metal species in the composite materials, they displayed promising electrocatalytic activities towards specific electrochemical reactions, i.e., Fe(np)/C for oxygen reactions, Rh(np)/C for water splitting, and NiPt(np)/C for HER.

It is believed that by means of this synthetic route, electrocatalysts with specific morphologies and furtherly enhanced catalytic activities can be obtained.

Appendix

Appendix 1 Parameters for evaluating electrocatalytic performance and corresponding electrochemical techniques

Some important parameters for evaluating catalytic performance of electrocatalysts are introduced here, as well as the corresponding electrochemical techniques.

Parameters for evaluating electrocatalytic performance

The following parameters are widely used for evaluating the catalytic performance of various electrocatalysts towards hydrogen- and oxygen-involving reactions.

Overpotential. Overpotential (η) is one of the most important descriptors to evaluate the electrocatalytic performance. At an ideal condition, the applied potential to drive an electrochemical reaction should be equal to the equilibrium potential of the reaction. In fact, it is usually larger than

that duo to the kinetic barriers. The difference between the applied potential and equilibrium potential to achieve a specific current density is defined as η. It can refer to a more oxidative potential for an oxidation reaction, or a more reductive potential for a reduction reaction. Good electrocatalysts display high current densities at low overpotentials.

Tafel slope. The relationship between current density (j) and overpotential (η) for an electrochemical reaction can be described by the Butler-Volmer equation:[180]

$$j = j_0 \left[\exp\left(\frac{\alpha_a n F \eta}{RT}\right) - \exp\left(-\frac{\alpha_c n F \eta}{RT}\right) \right]$$

where j_0 is the exchange current density, n is the electron transfer number, F is the Faraday constant, R is the ideal gas constant, T is the temperature, α_a and α_c are the charge transfer coefficients of anodic and cathodic reaction, respectively.

When the anodic overpotential is large enough, the cathodic current becomes negligible. The equation then can be simplified into:

$$j = j_0 \exp\left(\frac{\alpha_a n F \eta}{RT}\right)$$

Its logarithm form is the Tafel equation:

$$\eta = a + b \log j$$

$$a = \frac{-2.303RT}{\alpha n F} \log j_0 \quad ; \quad b = \frac{2.303RT}{\alpha n F}$$

The value of b indicates Tafel slop, which tells the required increment of overpotential in order to increase the current density by ten-fold. A good electrocatalyst would display a low Tafel slope. And for a multi-step electrochemical reaction, Tafel slope may provide important information for understanding the reaction mechanism.

Exchange current density. Exchange current density (j_0) represents the intrinsic catalytic activity of

an electrocatalyst at equilibrium potential. It can also be deduced from Tafel equation when overpotential is assumed to be zero. An effective electrocatalyst would show a high exchange current density.

Stability. Stability is another important parameter used to evaluate the catalytic performance. In general, there are two methods for measuring the stability: voltammetric method and galvanostatic (or potentiostatic) method. The voltammetric method compares the change of overpotential before and after multiple cycles of electrocatalysis. And a smaller change indicates that the electrocatalyst is more stable. The galvanostatic (or potentiostatic) method records the change of potential (or current density) with time at a constant current density (or potential) during the electrocatalysis. A longer duration with a smaller change of potential (or current density) suggests better stability of the catalyst. Common problems of stability tests involve material exfoliation by intense bubbling and degradation at harsh pH conditions.

Electrochemical Active Surface Area. Since a catalytic process basically occurs at surface active sites, it is important to know the value of electrochemical active surface area (ECSA) of the catalyst. Also, by measuring the loss of active area, the stability of the catalyst during its operation can be examined. Some methods have been adopted for determining the active area of a catalyst, such as hydrogen adsorption, surface oxide reduction, double layer capacitance, adsorbed carbon monoxide stripping, and underpotential deposition of metals.[181] Here the discussion is focused on the hydrogen adsorption method for the active area of noble metal electrodes and their alloys.

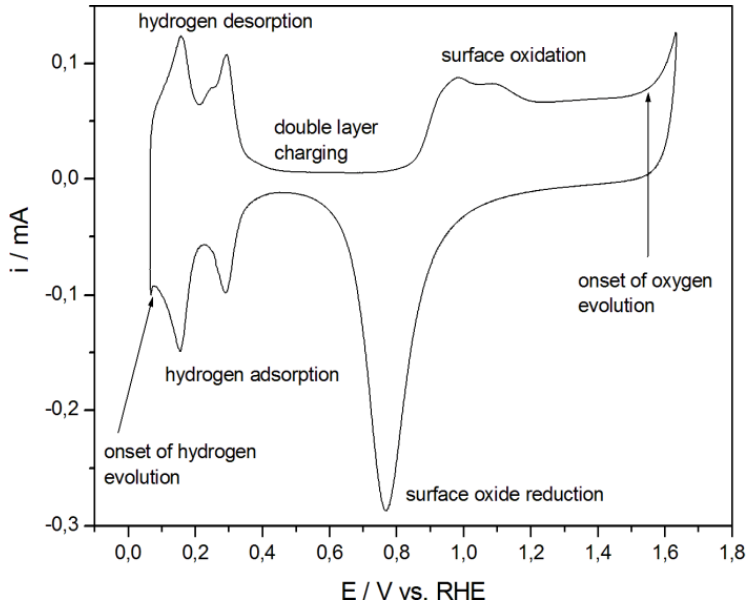

Figure A1.1 Cyclic voltammogram (scan rate 0.1 V s^{-1}) recorded for a polycrystalline Pt electrode in 0.5 M H_2SO_4 (temperature 298 K). Reprinted with permission from reference [182]. Copyright © 2016 The Authors. Published by ESG.

The ECSA generally can be calculated from the charge due to the anodic process of hydrogen desorption (Figure A1.1) using the following equation:[182]

$$\mathrm{ECSA} = \frac{\mathrm{Q}}{0.21\mathrm{M}}$$

where Q is the charge exchanged during desorption of hydrogen, mC cm^{-2}; M represents the noble metal loading on the electrode, mg cm^{-2}; and 0.21 (mC cm^{-2}) is the charge density needed to oxidize a monolayer of hydrogen molecules on Pt, which would be 0.221 mC cm^{-2} for Rh.

Turnover frequency. Turnover frequency (TOF) is used to evaluate the intrinsic catalytic activity of an active site. It is defined as the total number of moles of product per catalytic site per time unit at a given potential. The TOF values can be obtained based on the equation:[183]

$$\mathrm{TOF} = \mathrm{j\ A} / 4\mathrm{nF}$$

where j is the current density at the given overpotential, A is the surface area of working electrode, n

is the number of moles of the active materials, and F is the faraday constant.

In fact, it is very difficult to determine the true active sites of catalysts. A more practical way to calculate TOF is to consider all metal sites as active ones. Although the values obtained in this way represent only a lower limit of the true TOFs, they still enable a consistent comparison of various catalysts.

Typical electrochemical measurement techniques

Three-electrode electrochemical system. A three-electrode electrochemical system is consisted of a working electrode, a reference electrode, and a counter electrode, which generally are connected with a potentiostat (Figure A1.2). The working electrode is loaded with catalyst to be tested. The reference electrode is used to compare the potential applied to the working electrode. The counter electrode is responsible for electron transfer. The potentiostat controls the potential of the working electrode with respect to the reference electrode by means of adjusting the current through the counter electrode.

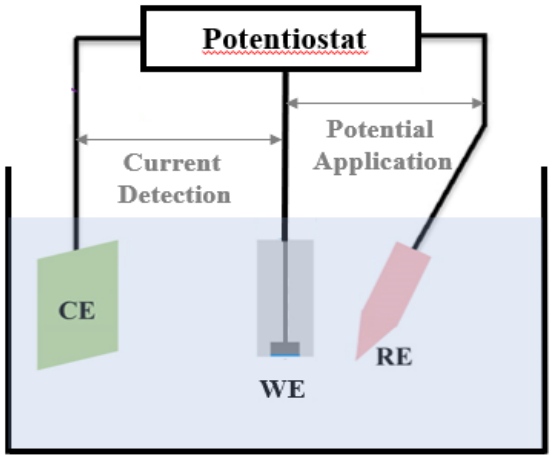

Figure A1.2 Three-electrode electrochemical system. WE, RE, and CE refer to the working electrode, reference electrode, and counter electrode, respectively.

Materials in powder form generally are deposited on conducting substrates, such as glassy carbon electrodes, forming a catalyst layer. The substrate and catalyst together serve as the working electrode. Free-standing materials can be used directly as the working electrode. Different reference electrodes can be used and a commonly used one is the saturated calomel electrode, which is based on the reaction between elemental mercury and mercury(I) chloride. A platinum wire is typically used as the counter electrode due to its chemical stability.

Linear sweep and cyclic voltammetry. The potential sweep technique refers to changing the applied potential to the working electrode over time while measuring the resulting current. If the sweep is from an initial potential to an end potential only in one direction, it is called linear sweep voltammetry (LSV). If the sweep continues in a reverse direction, it is called cyclic voltammetry (CV) (Figure A1.3).

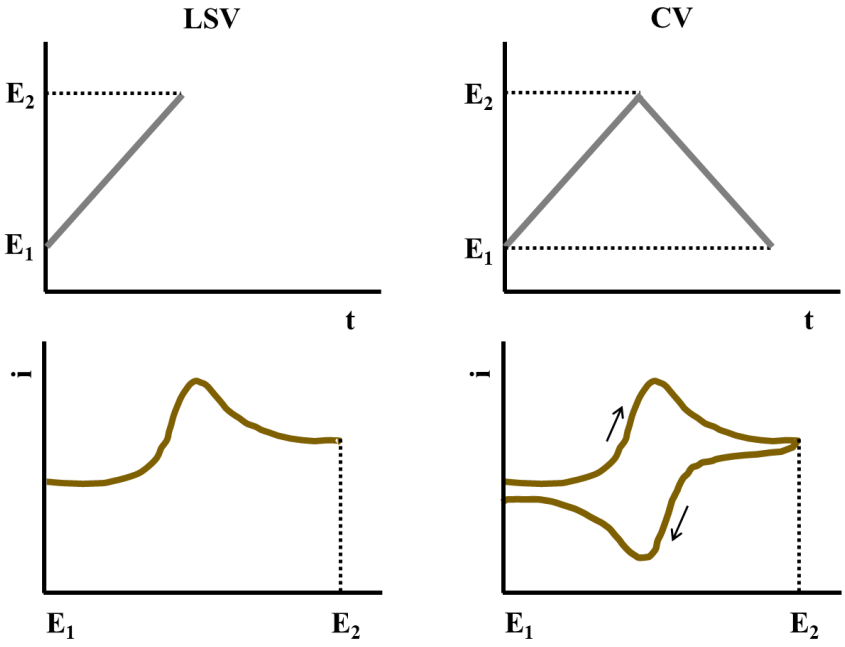

Figure A1.3 Potential waveforms and the resulting voltammograms for linear sweep and cyclic voltammetry.

The results are generally displayed as current-potential curves (voltammograms). The current at a specific overpotential and overpotential for a specific current for an electrochemical reaction can be

readily obtained from voltammograms. In addition, Tafel plots also can be derived from voltammograms.

Rotating disk electrode and rotating ring disk electrode. Common tools for evaluating the ORR activity of an electrocatalyst are rotating disk electrode (RDE) and rotating ring disk electrode (RRDE). See Figure A1.4.

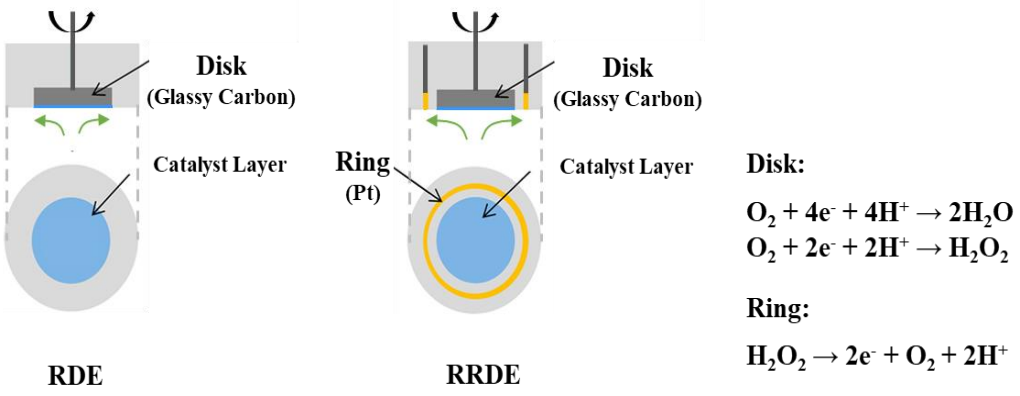

Figure A1.4 Schemes of RDE and RRDE. The catalyst is loaded on the embedded glassy carbon disk of RDE or RRDE forming a layer. Adapted from reference [184]. Copyright © 2015 American Chemical Society

RDE method involves the examination of the whole current due to ORR by a disk electrode at different rotation rates. From RDE polarization curves, some ORR performance indicators, such as onset potential and mass transport current density can be obtained. The RDE method also supplies a way to calculate electron transfer number (n) of ORR based on the Koutecký-Levich (K-L) equation:[185]

$$\frac{1}{j} = \frac{1}{j_L} + \frac{1}{j_K} = \frac{1}{Bw^{1/2}} + \frac{1}{j_K}$$

$$B = 0.62nFC_0{D_0}^{2/3}{v_0}^{-1/6}$$

where j is the measured current density, j_L is the mass transport current density, j_K is the kinetic current density, w is the angular rotation speed (rad s^{-1}), B is the Levich constant, n is the electron transfer

number, F is the Faraday constant, C_0 is the concentration of O_2 in the bulk electrolyte, D_0 is the diffusion coefficient of O_2 in electrolyte, v is the kinematic viscosity of the electrolyte.

By plotting the inverse measured current density versus the inverse square root of the rotation speed, the electron transfer number can be calculated from the slope of the linear part, and the inverse of the kinetic current density can be obtained by extrapolating the formed line to the ordinate. It has been reported that the n values obtained from K-L equation sometimes exceed theoretical limit.[185] Therefore, in this thesis RRDE measurement is preferred to acquire the n values of ORR.

RRDE method records not only the current due to ORR by a disk electrode, but also the current from oxidation of ORR intermediates (H_2O_2 or HO_2^-) by a ring electrode. With the aid of RRDE measurement, the percentages of the generated intermediates and the electron transfer number during ORR can be obtained according to the following equations:

$$H_2O_2\% = \frac{200 i_R/N}{i_D + i_R/N}$$

$$n = \frac{4 i_D}{i_D + i_R/N}$$

where i_R is the ring current, i_D is the disk current, and N is the collection efficiency (25.8% for the RRDE used in the thesis).

Appendix for Chapter 2

(a) Synthesis of potassium-graphite intercalation compound.

120 mg (10.00 mmol) of graphite material was placed in a vial together with 48.8 mg (1.25 mmol) of cleaned potassium (stoichiometry KC_8) inside an argon-filled glove box, and the mixture was heated

for 5 hours at 180 °C on a heating plate under occasional stirring. Then, the vial was allowed to cool down to room temperature. The potassium-intercalated compound was collected.

(Safety remark: The possible users of the presented synthetic protocol are reminded of the specific danger related to the use of potassium metal. Safety precaution is advised for storage, handling, and waste treatment. Potassium metal is extremely dangerous when in contact with water or moistures, releasing hydrogen with sufficient heat to cause ignition or explosion. Peroxide formation may occur in containers that have been opened and remained in storage. It may produce corrosive solutions in contact with water.)

(b) Synthesis of ternary intercalation compound $KC_{24}(THF)x$.

150 mg of the obtained K-intercalated compound was mixed with 150 mL of absolute THF in a 250 mL Erlenmeyer flask under inert condition. The solvent was exposed to the intercalation compound for 48 h. Afterwards, the dispersion was centrifuged in the glove box (4000 rpm / 20 min), and the supernatant was removed. The samples have been redispersed in THF followed by another centrifugation step (4000 rpm / 20 min), and the final ternary intercalation compound was isolated.

(c) Synthesis of the iron inclusion compound.

The as prepared ternary intercalation compound $KC_{24}(THF)_x$ has been used directly as reduction agent, generating FeIC. 50 mL of anhydrous THF was added to the Ternary intercalation compound $KC_{24}(THF)_x$. Equimolar amount of recrystallized metal(II) chloride dissolved in 100 mL of absolute THF was added dropwise to the mixture in a 250 mL Erlenmeyer flask inside an argon filled glove box. After complete addition, the respective mixture was stirred for 48 hours. Afterwards, the dispersion was centrifuged in the glove box (4000 rpm / 20 min) and the supernatant was removed.

The sample has been redispersed in THF followed by another centrifugation step (4000 rpm / 20 min). Afterwards the sample has been removed from the glove box and 20 mL of distilled water was added. The sample has been added to a separation funnel with 20 mL of cyclohexane and has been extracted 3 times with distilled water. The iron inclusion compound FeIC has been collected via filtration (0.4 µm filter membranes) and dried in vacuum.

Appendix for Chapter 3

A.3.1 Fe(np)/C preparation

Chemicals

Graphite materials. Graphitic nano carbon was obtained from FGV, Cambrige Nanosystems, Grade CamGraph® G1. The nono carbon is of synthetic origin. The carbon content is more than 95%, and no inorganic impurity was found by means of Thermogravimetric Analysis (TGA). Micro graphite was obtained from Nacional de grafite grade micrograf 99503UJ. The carbon content is 99.5%, and the ash content is less than 0.1%. Natural and crystalline flake graphite was obtained from Asbury Carbons Grade 3061 (mesh 50+). The carbon content is more than 99%, and the ash content is less than 0.1%. Iron (II) tetrafluoroborate, $Fe(BF_4)_2$, was recrystallized twice inside the glove box prior to use. Tetrahydrofuran (THF) was purified prior to use by means of Pure Solv 400-4-MD solvent purification system, which is directly attached to the glove box. Potassium hydroxide, KOH, pellets were obtained from Sigma Aldrich (99.99% purity).

Synthetic route

(a) Synthesis of potassium-graphite intercalation compounds.

120 mg (10.00 mmol) of each graphite starting materials (flake graphite, micro graphite, and graphitic nano carbon) was placed in a vial together with 48.8 mg (1.25 mmol) of cleaned potassium (stoichiometry KC_8) inside an argon-filled glove box, and the mixture was heated for 5 hours at 180 °C on a heating plate under occasional stirring. Then, the vial was allowed to cool down to room temperature. The potassium-intercalated compound was collected.

(b) Dispersing K-intercalated compound and isolating graphenide solution.

150 mg of the obtained K-intercalated compound was mixed with 150 mL of absolute THF in a 250 mL Erlenmeyer flask under inert condition, and stirred for 3 days with the aid of a glass-coated magnetic stirring bar. Then, the dispersion was centrifuged at 3500 rpm for 30 minutes under inert condition, and the faint yellowish upper solution was retained. The obtained graphenide solution was assumed to possess negatively charged carbon layers.

(c) Synthesis of the iron oxide nanoparticle supported on carbon composite materials.

Equimolar amount of recrystallized $Fe(BF_4)_2$ was dissolved in 10 mL of absolute THF, and added dropwise to 100 mL of the obtained graphenide solution in a 250 mL Erlenmeyer flask inside the argon-filled glove box. Here, the graphenide solution was used directly as reduction agent. After 5 to 15 minutes, aggregation and precipitation occurred. The dispersion was stirred for 24 hours, and then centrifuged inside the glove box (4000 rpm, 20 minutes). Afterwards, the sample was removed from the glove box and 20 mL of distilled water was added. Then the sample was added to a separation funnel with 20 mL of cyclohexane and was extracted 3 times with distilled water. Finally, the sample was collected by filtration and dried in vacuum.

A.3.2 Characterization

Physical characterizations

X-ray diffraction (XRD). The XRD patterns were collected on a Rigaku Nanoviewer (XRF microsource generator, MicroMax007HF) with a 1200W rotating anode coupled to a confocal Max-Flux Osmic Mirror (Applied Rigaku Technologies, Austin, USA) and a MAR345 image plate detector (MARResearch, Norderstedt, Germany). The samples were filled into glass capillaries and exposed to the X-ray beam, and the detector was placed at a distance of 156 mm providing access to 2 theta angles in the range between 0.9° and 48°.

X-ray photoelectron spectroscopy (XPS). A Thermo Fisher Scientific K-ALPHA spectrometer was used for surface analysis with a monochromatized AlKα source (hν = 1486.6 eV) and a 200 microns spot size. A pressure of 10^{-7} Pa was maintained in the chamber during analysis. The full spectra (0-1150 eV) were obtained with constant pass energy of 200 eV and high-resolution spectra at constant pass energy of 40 eV. Charge neutralization was applied for all samples. High resolution spectra were fitted and quantified using the AVANTAGE software provided by Thermo Fisher Scientific and the Scofield sensitivity factors available from the internal database.

Transmission electron microscopy (TEM). TEM measurements were performed on a TEM-FEG HR (JEOL 2200FS). TEM grids have been prepared by drop casting 20 µl of nanocomposite dispersion in THF directly onto SF400-CU (silicon monoxide membranes on 400 mesh copper grid, Electron microscopy science) or S166-3 Lacey carbon film (300 mesh copper grid, Agar Scientific) TEM grids.

Thermogravimetric Analysis (TGA). TGA measurement was performed on a TA Q50 TGA. About 6-8 mg of composite sample was weighed in a Pt-crucible. The measurements were performed under

synthetic air (N_2 80%, O_2 20%) between 30-800 °C with a heating rate of 10 °C / min.

Electrochemical measurements

A rotating disk electrode (RDE, 3 mm in diameter, 0.071 cm^2 geometric surface area) was polished with 0.3 μm and 0.05 μm alumina slurry, and sonicated in ethanol and DI water before each experiment. Each catalyst ink (5 mg mL^{-1}) was prepared by mixing 5 mg Fe(np)/C sample, 950 μL H_2O and isopropanol (with a volume ratio of 3:1), and 50 μL 5% Nafion solution (as a binder to keep catalyst stable on the surface of electrode) and sonicating for 30 minutes. 5 μL catalyst ink was pipetted onto the tip of RDE and dried to form a catalyst layer (0.35 mg cm_{geo}^{-2}, normalized to the geometric surface area) at room temperature. For measuring the electron transfer number of ORR, a rotating ring disk electrode (RRDE, 5 mm in diameter, 0.196 cm^2 geometric surface area area) was used. The preparing process was quite similar.

The electrochemical measurements were performed within a typical three-electrode system coupled to a SP-300 bipotentiostat (Biologic Instruments) electrochemistry workstation. The three-electrode system consists of a RDE (loaded with catalyst) as working electrode, a saturated calomel electrode (SCE, Hg/Hg_2Cl_2/saturated KCl) as reference electrode, and a Pt wire as counter electrode. 0.1 M KOH aqueous solution was used as the electrolyte. Before ORR test, O_2 was bubbled inside the solution to get it O_2-saturated, and during ORR test, O_2 was bubbled over the surface of the solution. For OER test, the solution was saturated with Ar. Before each experiment, uncompensated resistance was measured by Electrochemical Impedance Spectroscopy (EIS) from 200 kHz to 100 mHz at open circuit potential. Cyclic voltammetry (CV) and linear sweep voltammetry (LSV) measurements were carried out at a scan rate of 10 mV s^{-1}. All potentials were corrected for uncompensated resistance and given

relative to the reversible hydrogen electrode (RHE) using the equation: $E_{RHE} = E_{SCE} + 0.242 + 0.059*$ pH - iR, where E_{RHE} is the potential calibrated against RHE, E_{SCE} is the potential measured against SCE, i is the measured current, R is the uncompensated resistance. Current densities were calculated using the geometric surface area.

Appendix for Chapter 4

A.4.1 Rh(np)/C, RhPt(np)/C, and Pt(np)/C preparation

Synthetic route

For the first and second steps, readers can refer A.3.1. (a) synthesis of potassium-graphite intercalation compounds, and (b) dispersing K-intercalated compound and isolating graphenide solution.

The next step was: (c) Synthesis of the Rhodium-based nanomaterials. Equimolar amount of anhydrous $RhCl_3$ and/or $PtCl_2$ chloride (specified in Table A4.1) was dissolved in 10 mL of absolute THF, and added dropwise to 50 mL of the obtained graphenide solution in a 250 mL Erlenmeyer flask inside an argon-filled glove box. Here, the graphenide solution was used directly as reduction agent. After 5 to 15 minutes, aggregation and precipitation occurred. The dispersion was stirred for 24 hours. Afterwards, the sample was removed from the glove box, and 100 mL of distilled water was added. Then the sample was purified by repeated centrifugation and re-dispersing steps (4 times, 1 h at 10000 rpm). The final materials were isolated by freeze drying.

Table A4.1 Amounts of the reactants used for the preparation of Rh / Pt-based nanomaterials

Sample	Metal salt	Weight of metal salt (mg)	Amount of metal salt (μmol)	Volume of graphenide solution (mL)	Weight of intercalation compound (mg)
Rh(np)/C	$RhCl_3$	12.9	61.6	50	25
RhPt(np)/C	$RhCl_3$, $PtCl_2$	6.4 ($RhCl_3$), 12.3 ($PtCl_2$)	30.8 ($RhCl_3$), 46.2 ($PtCl_2$)	50	25
Pt(np)/C	$PtCl_2$	24.6	92.5	50	25

A.4.2 Characterization

Physical characterizations

As reported in A.3.2.

Electrochemical measurements

A rotating disk electrode (RDE, 3 mm in diameter, 0.071 cm^2 geometric surface area) or glassy caron electrode (GC, 3 mm in diameter, 0.071 cm^2 geometric surface area) was polished with 0.3 μm and 0.05 μm alumina slurry, and sonicated in ethanol and DI water before each experiment. Each catalyst ink (1 mg mL^{-1}) was prepared by mixing 1 mg material, 950 μL dimethylformamide (DMF), and 50 μL 5% Nafion solution (as a binder to keep catalyst stable on the surface of electrode), and sonicating for 30 minutes. 30 μL catalyst ink was pipetted onto the tip of RDE / GC, and dried to form a catalyst layer (0.42 mg cm_{geo}^{-2}, normalized to the geometric surface area) at room temperature. Commercial RuO_2 and Pt/C (20 wt%) were used as reference catalysts for OER and HER, respectively, and prepared for measurement in the same way.

The electrochemical measurements were performed within a typical three-electrode system coupled to a SP-300 bipotentiostat (Biologic Instruments) electrochemistry workstation. The three-electrode system consists of a RDE / GC (loaded with catalyst) as working electrode, a saturated calomel electrode (SCE, Hg/Hg_2Cl_2/saturated KCl) as reference electrode, and a Pt wire as counter electrode. 0.1 M KOH aqueous solution was used as the electrolyte. The prepared GC electrode was used for HER measurement, while the solution was stirred with the aid of a magnetic stirrer in order to remove the produced H_2 from the electrode surface. The prepared RDE electrode was used for OER measurement, and kept at a specific rotation speed during the test to remove O_2. The electrolyte was saturated with Ar gas.

Before each experiment, uncompensated resistance was measured by Electrochemical Impedance Spectroscopy (EIS) from 200 kHz to 100 mHz at open circuit potential. Linear sweep voltammetry (LSV) measurements were carried out at a scan rate of 5 mV s^{-1}. The turnover frequency (TOF) measurement was performed by a sequence of potential steps (200 seconds for each) under different overpotentials. The electrochemical active surface area (ECSA) measurements were investigated by cyclic voltammetry (CV) within a potential range of 0 V to 1.0 V (vs RHE) at a scan rate of 50 mV s^{-1}. The electrocatalytic stability test for OER was conducted by chronopotentiometry at a specific current density. All potentials were corrected for uncompensated resistance, and given relative to the reversible hydrogen electrode (RHE) using the equation: $E_{RHE} = E_{SCE} + 0.242 + 0.059\ pH - iR$, where E_{RHE} is the potential calibrated against RHE, E_{SCE} is the potential measured against SCE, i is the measured current, and R is the uncompensated resistance. Current densities were calculated using the geometric surface area.

The electrochemical active surface areas (ECSAs) of Rh(np)/C, RhPt(np)/C, and Pt(np)/C were examined by means of cyclic voltammetry (CV) at a scan rate of 50 mV s^{-1} within a potential range of 0 V to 1.0 V (vs RHE) in Ar saturated 0.1 M aqueous KOH solution. As shown in Figure A4.1, the hydrogen desorption regions (shaded regions) were integrated after subtracting the double-layer currents, and the resulting coulombic charges were normalized to the corresponding metal loading on the electrode, with charge densities of 221 μC cm^{-2} for Rh and 210 μC cm^{-2} for Pt. The ECSAs of Rh(np)/C, RhPt(np)/C, and Pt(np)/C were calculated to be 7.7, 17.5, and 22.2 m^2 g^{-1}, respectively. This result was actually undesirable considering that Rh(np)/C displayed better electrocatalytic activities. Here, further understanding is needed.

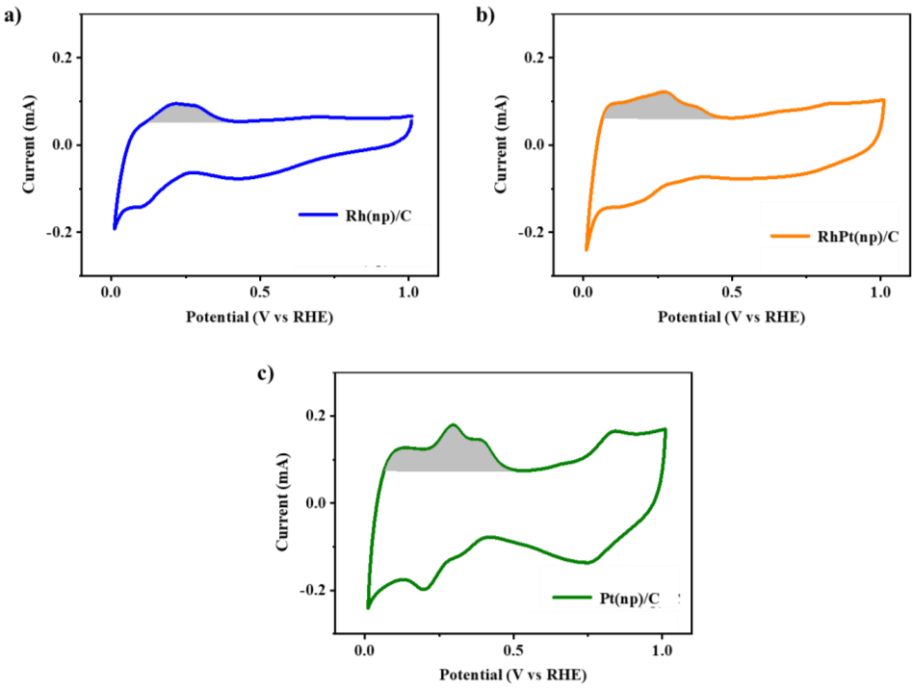

Figure A4.1 CV curves of Rh(np)/C, RhPt(np)/C, and Pt(np)/C at a scan rate 50 mV s^{-1} in Ar saturated 0.1 M aqueous KOH solution. The shaded areas, which referred to hydrogen desorption, were used for the calculation of ECSAs.

The effect of catalyst loading on ORR performance. When investigating the catalytic properties of newly developed materials, it is important to study the effect of catalyst loading on the performance. Therefore, different loadings of Fe(np)/C were measured by means of RDE. As shown in Figure A4.2, the current density of ORR increases as the Fe(np)/C loading increases from 70 μg cm^{-2}, over 140 μg cm^{-2}, to 350 μg cm^{-2}. And the numbers of electron transferred during ORR are 3.6, 4.1, and 4.1, respectively, according to K-L equation. Therefore, to achieve high current density and constant numbers of electron transferred, the loading of Fe(np)/C was decided to be 350 μg cm^{-2}.

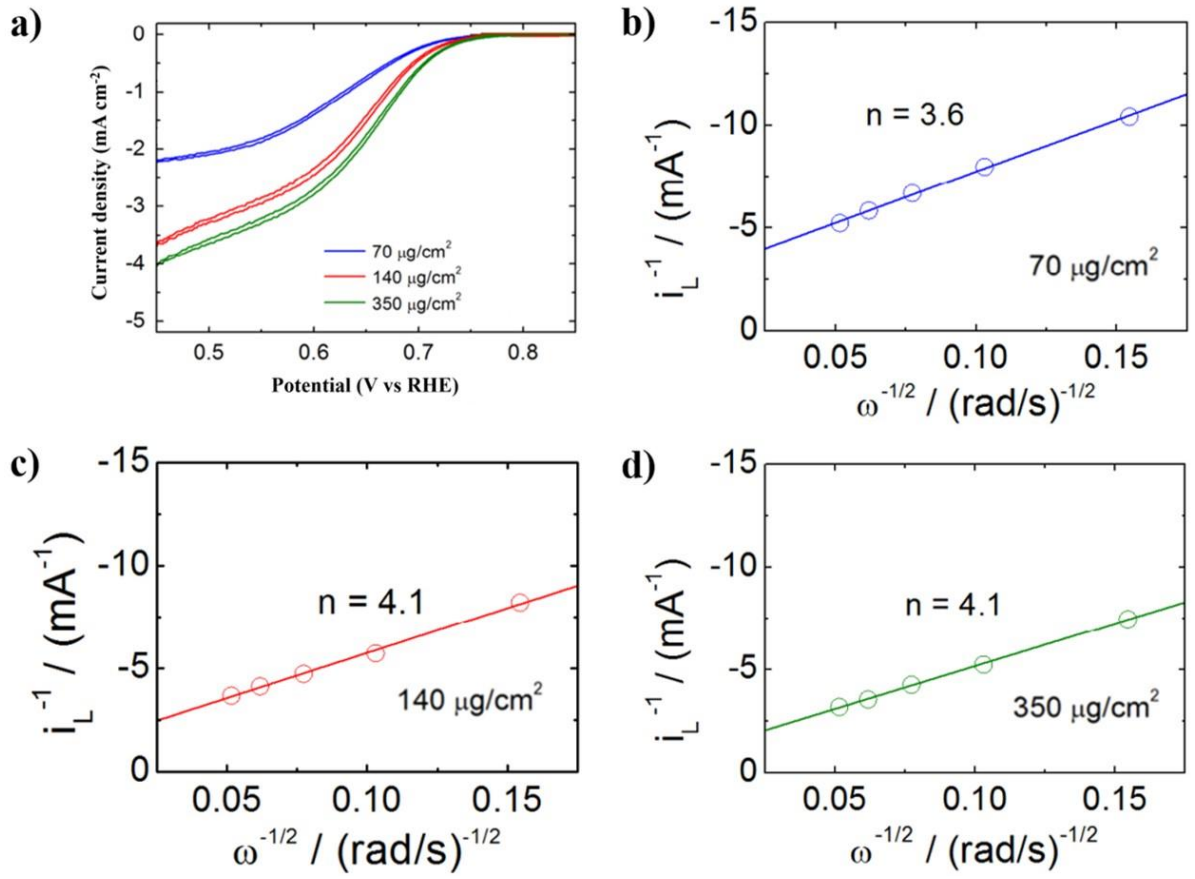

Figure A4.2 (a) CV curves of s-Fe(np)/C with different loadings (70, 140, and 350 μg cm^{-2}) under rotation speed of 1600 rpm at a scan rate of 10 mV s^{-1} in an O_2 saturated 0.1 M aqueous KOH solution. (b), (c), and (d) Corresponding K-L plots at the potential of 0.55 V (vs RHE).

Appendix for Chapter 5

A.5.1 Ni(np)/C and NiPt(np)/C preparation

Physical characterizations

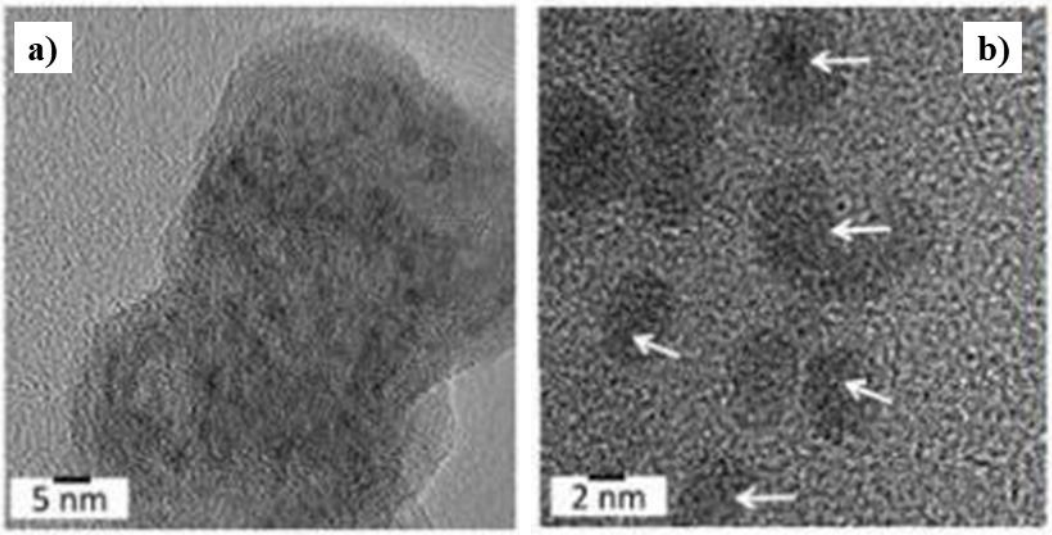

Figure A5.1 TEM images of Ni(np)/C.

Transmission Electron Microscopy (TEM) images (Figure A5.1) showed that Ni oxide nanoparticles were well dispersed on carbon layers, and the size of Ni oxide nanoparticles was around 3 nm. This was identical to what has been observed from Fe(np)/C, Rh(np)/C, etc.

A.5.2 Co/C preparation

Synthetic route

Synthesis of silica-supported cobalt nanoparticles

First, silica nanospheres were synthesized following the Stöber method. Typically, 6.2 mL tetraethyl orthosilicate (TEOS) was added to a solution of 6.5 mL ammonium hydroxide, 100 mL ethanol, and

7.1 mL water. After stirring for 15 h, a colloidal solution of silica nanospheres with a diameter of 250 nm was obtained.

Then, 1 g silica nanospheres were added to a mixture of 180 mL isopropanol and 1.5 mL 3-aminopropyltriethoxysilane (APTS), and stirred for 2 h at 80 ºC to functionalize the surface of silica with amino groups. Silica-supported cobalt nanoparticles were achieved by adding 0.5 g -NH_2 modified silica nanospheres to 0.1 M cobalt nitrate solution and stirring for 15 minutes at room temperature.

Synthesis of nanoporous carbon-supported cobalt nanoparticles

Polyaniline (PANI) was synthesized by oxidative polymerization of aniline in the presence of ammonium persulfate. Typically, 1 mL aniline was added to 60 mL 1 M HCl solution under stirring at a temperature between 0 and 5 ºC. And 12 mL 1 M HCl solution containing 2.5 g ammonium persulfate was added to the above solution. After stirring for 8 h, PANI was obtained.

Then, the prepared silica-supported cobalt nanoparticles and PANI were dispersed in water respectively, and mixed together followed by filtration, forming a composite of silica-supported cobalt nanoparticles and PANI, PANI/Silica-Co. This composite material went through a process of pyrolysis at 900 ºC under Ar atmosphere for 3 h. To remove the silica template, the resulting product was treated with 1 M NaOH solution in an autoclave at 100 ºC for 18 h, after which nanoporous carbon-supported cobalt nanoparticles (C/Co) were prepared.

References

1 S. Chu and A. Majumdar, *Nature*, 2012, **488**, 294–303.

2 D. Larcher and J. M. Tarascon, *Nat. Chem.*, 2015, **7**, 19–29.

3 G. Zhao, K. Rui, S. X. Dou and W. Sun, *Adv. Funct. Mater.*, 2018, **28**, 1–26.

4 A. Ursua, P. Sanchis and L. M. Gandia, *Proc. IEEE*, 2012, **100**, 410–426.

5 M. David, C. Ocampo-Martínez and R. Sánchez-Peña, *J. Energy Storage*, 2019, **23**, 392–403.

6 M. Carmo, D. L. Fritz, J. Mergel and D. Stolten, *Int. J. Hydrogen Energy*, 2013, **38**, 4901–4934.

7 F. M. Sapountzi, J. M. Gracia, C. J. (Kee. J. Weststrate, H. O. A. Fredriksson and J. W. (Hans. Niemantsverdriet, *Prog. Energy Combust. Sci.*, 2017, **58**, 1–35.

8 J. Wang, Y. Gao, H. Kong, J. Kim, S. Choi, F. Ciucci, Y. Hao, S. Yang, Z. Shao and J. Lim, *Chem. Soc. Rev.*, 2020, 9154–9196.

9 A. Ali and P. K. Shen, *Carbon Energy*, 2020, **2**, 99–121.

10 J. Wei, M. Zhou, A. Long, Y. Xue, H. Liao, C. Wei and Z. J. Xu, *Nano-Micro Lett.*, 2018, **10**, 1–15.

11 J. K. Nørskov, T. Bligaard, A. Logadottir, J. R. Kitchin, J. G. Chen, S. Pandelov and U. Stimming, *J. Electrochem. Soc.*, 2005, **152**, J23.

12 E. Skúlason, V. Tripkovic, M. E. Björketun, S. Gudmundsdóttir, G. Karlberg, J. Rossmeisl, T. Bligaard, H. Jónsson and J. K. Nørskov, *J. Phys. Chem. C*, 2010, **114**, 18182–18197.

13 L. Ji, J. Wang, S. Zuo and Z. Chen, *J. Phys. Chem. C*, 2017, **121**, 8923–8930.

14 L. Zhang, L. Han, H. Liu, X. Liu and J. Luo, *Angew. Chemie - Int. Ed.*, 2017, **56**, 13694–13698.

15 N. Cheng, S. Stambula, D. Wang, M. N. Banis, J. Liu, A. Riese, B. Xiao, R. Li, T. K. Sham, L. M. Liu, G. A. Botton and X. Sun, *Nat. Commun.*, 2016, **7**, 1–9.

16 J. Chen, B. Lim, E. P. Lee and Y. Xia, *Nano Today*, 2009, **4**, 81–95.

17 A. Zalineeva, S. Baranton, C. Coutanceau and G. Jerkiewicz, *Sci. Adv.*, 2017, **3**, 1–11.

18 S. Liu, X. Mu, H. Duan, C. Chen and H. Zhang, *Eur. J. Inorg. Chem.*, 2017, **2017**, 535–539.

19 Y. Xu, S. Yin, C. Li, K. Deng, H. Xue, X. Li, H. Wang and L. Wang, *J. Mater. Chem. A*, 2018, **6**, 1376–1381.

20 J. Hu, C. Fang, X. Jiang, D. Zhang and Z. Cui, *Inorg. Chem. Front.*, 2020, 4377–4386.

21 T. T. Yang, H. Zhu, M. Wan, L. Dong, M. Zhang and M. L. Du, *Chem. Commun.*, 2016, **52**, 990–993.

22 Y. Luo, X. Luo, G. Wu, Z. Li, G. Wang, B. Jiang, Y. Hu, T. Chao, H. Ju, J. Zhu, Z. Zhuang, Y. Wu, X. Hong and Y. Li, *ACS Appl. Mater. Interfaces*, 2018, **10**, 34147–34152.

23 X. Zhong, L. Wang, Z. Zhuang, X. Chen, J. Zheng, Y. Zhou, G. Zhuang, X. Li and J. Wang, *Adv. Mater. Interfaces*, , DOI:10.1002/admi.201601029.

24 P. Wang, K. Jiang, G. Wang, J. Yao and X. Huang, *Angew. Chemie - Int. Ed.*, 2016, **55**, 12859–12863.

25 Z. Cao, Q. Chen, J. Zhang, H. Li, Y. Jiang, S. Shen, G. Fu, B. A. Lu, Z. Xie and L. Zheng, *Nat. Commun.*, 2017, **8**, 15131.

26 W. Ren, W. Zang, H. Zhang, J. Bian, Z. Chen, C. Guan and C. Cheng, *Carbon*, 2019, **142**, 206–216.

27 S. Bai, C. Wang, M. Deng, M. Gong, Y. Bai, J. Jiang and Y. Xiong, *Angew. Chemie - Int. Ed.*, 2014, **53**, 12120–12124.

28 J. Su, Y. Yang, G. Xia, J. Chen, P. Jiang and Q. Chen, *Nat. Commun.*, 2017, **8**, 1–10.

29 B. K. Barman, D. Das and K. K. Nanda, *Sustain. Energy Fuels*, 2017, **1**, 1028–1033.

30 T. Bhowmik, M. K. Kundu and S. Barman, *ACS Catal.*, 2016, **6**, 1929–1941.

31 J. Mahmood, F. Li, S. M. Jung, M. S. Okyay, I. Ahmad, S. J. Kim, N. Park, H. Y. Jeong and J. B. Baek, *Nat. Nanotechnol.*, 2017, **12**, 441–446.

32 G. Valenti, A. Boni, M. Melchionna, M. Cargnello, L. Nasi, G. Bertoni, R. J. Gorte, M. Marcaccio, S. Rapino, M. Bonchio, P. Fornasiero, M. Prato and F. Paolucci, *Nat. Commun.*, 2016, **7**, 1–8.

33 D. V. Esposito, S. T. Hunt, A. L. Stottlemyer, K. D. Dobson, B. E. McCandless, R. W. Birkmire and J. G. Chen, *Angew. Chemie - Int. Ed.*, 2010, **49**, 9859–9862.

34 Y. Zhang, J. Tan, F. Wen, Z. Zhou, M. Zhu, S. Yin and H. Wang, *Int. J. Hydrogen Energy*, 2018, **43**, 6167–6176.

35 J. Zhang, P. Liu, G. Wang, P. P. Zhang, X. D. Zhuang, M. W. Chen, I. M. Weidinger and X. L. Feng, *J. Mater. Chem. A*, 2017, **5**, 25314–25318.

36 B. Liu, B. He, H. Q. Peng, Y. Zhao, J. Cheng, J. Xia, J. Shen, T. W. Ng, X. Meng, C. S. Lee and W. Zhang, *Adv. Sci.*, 2018, **5**, 1–7.

37 H. Li, P. Wen, Q. Li, C. Dun, J. Xing, C. Lu, S. Adhikari, L. Jiang, D. L. Carroll and S. M. Geyer, *Adv. Energy Mater.*, , DOI:10.1002/aenm.201700513.

38 T. Zheng, W. Sang, Z. He, Q. Wei, B. Chen, H. Li, C. Cao, R. Huang, X. Yan, B. Pan, S. Zhou and J. Zeng, *Nano Lett.*, 2017, **17**, 7968–7973.

39 J. Miao, Z. Lang, X. Zhang, W. Kong, O. Peng, Y. Yang, S. Wang, J. Cheng, T. He, A. Amini, Q. Wu, Z. Zheng, Z. Tang and C. Cheng, *Adv. Funct. Mater.*, ,

DOI:10.1002/adfm.201805893.

40 S. Jing, J. Lu, G. Yu, S. Yin, L. Luo, Z. Zhang, Y. Ma, W. Chen and P. K. Shen, *Adv. Mater.*, , DOI:10.1002/adma.201705979.

41 C. Wan, Y. N. Regmi and B. M. Leonard, *Angew. Chemie - Int. Ed.*, 2014, **53**, 6407–6410.

42 H. Park, A. Encinas, J. P. Scheifers, Y. Zhang and B. P. T. Fokwa, *Angew. Chemie - Int. Ed.*, 2017, **56**, 5575–5578.

43 J. Hu, B. Huang, C. Zhang, Z. Wang, Y. An, D. Zhou, H. Lin, M. K. H. Leung and S. Yang, *Energy Environ. Sci.*, 2017, **10**, 593–603.

44 F. Haque, A. Zavabeti, B. Y. Zhang, R. S. Datta, Y. Yin, Z. Yi, Y. Wang, N. Mahmood, N. Pillai, N. Syed, H. Khan, A. Jannat, N. Wang, N. Medhekar, K. Kalantar-Zadeh and J. Z. Ou, *J. Mater. Chem. A*, 2019, **7**, 257–268.

45 Y. Liang, Q. Liu, A. M. Asiri, X. Sun and Y. Luo, *ACS Catal.*, 2014, **4**, 4065–4069.

46 M. A. Lukowski, A. S. Daniel, F. Meng, A. Forticaux, L. Li and S. Jin, *J. Am. Chem. Soc.*, 2013, **135**, 10274–10277.

47 J. Tian, Q. Liu, A. M. Asiri and X. Sun, *J. Am. Chem. Soc.*, 2014, **136**, 7587–7590.

48 Q. Gong, Y. Wang, Q. Hu, J. Zhou, R. Feng, P. N. Duchesne, P. Zhang, F. Chen, N. Han, Y. Li, C. Jin, Y. Li and S. T. Lee, *Nat. Commun.*, , DOI:10.1038/ncomms13216.

49 C. N. R. Rao and M. Chhetri, *Adv. Mater.*, , DOI:10.1002/adma.201803668.

50 Y. Jiao, Y. Zheng, K. Davey and S. Z. Qiao, *Nat. Energy*, , DOI:10.1038/nenergy.2016.130.

51 V. Vij, S. Sultan, A. M. Harzandi, A. Meena, J. N. Tiwari, W. G. Lee, T. Yoon and K. S. Kim, *ACS Catal.*, 2017, **7**, 7196–7225.

52 M. García-Mota, M. Bajdich, V. Viswanathan, A. Vojvodic, A. T. Bell and J. K. Nørskov, *J.*

Phys. Chem. C, 2012, **116**, 21077–21082.

53 I. C. Man, H. Y. Su, F. Calle-Vallejo, H. A. Hansen, J. I. Martínez, N. G. Inoglu, J. Kitchin, T. F. Jaramillo, J. K. Nørskov and J. Rossmeisl, *ChemCatChem*, 2011, **3**, 1159–1165.

54 Y. Lee, J. Suntivich, K. J. May, E. E. Perry and Y. Shao-Horn, *J. Phys. Chem. Lett.*, 2012, **3**, 399–404.

55 S. Cherevko, S. Geiger, O. Kasian, N. Kulyk, J. P. Grote, A. Savan, B. R. Shrestha, S. Merzlikin, B. Breitbach, A. Ludwig and K. J. J. Mayrhofer, *Catal. Today*, 2016, **262**, 170–180.

56 J. Suntivich, K. J. May, H. A. Gasteiger, J. B. Goodenough, Y. Shao-horn, F. Calle-vallejo, A. D. Oscar, M. J. Kolb, M. T. M. Koper, J. Suntivich, K. J. May, H. A. Gasteiger, J. B. Goodenough and Y. Shao-horn, *Science*, 2011, **334**, 2010–2012.

57 S. Yagi, I. Yamada, H. Tsukasaki, A. Seno, M. Murakami, H. Fujii, H. Chen, N. Umezawa, H. Abe, N. Nishiyama and S. Mori, *Nat. Commun.*, 2015, **6**, 1–6.

58 A. Vojvodic and J. K. Nørskov, *Science*, 2011, **334**, 1355–1356.

59 M. Al-Mamun, X. Su, H. Zhang, H. Yin, P. Liu, H. Yang, D. Wang, Z. Tang, Y. Wang and H. Zhao, *Small*, 2016, **12**, 2866–2871.

60 M. Li, Y. Xiong, X. Liu, X. Bo, Y. Zhang, C. Han and L. Guo, *Nanoscale*, 2015, **7**, 8920–8930.

61 X. Long, J. Li, S. Xiao, K. Yan, Z. Wang, H. Chen and S. Yang, *Angew. Chemie*, 2014, **126**, 7714–7718.

62 R. Subbaraman, D. Tripkovic, K. C. Chang, D. Strmcnik, A. P. Paulikas, P. Hirunsit, M. Chan, J. Greeley, V. Stamenkovic and N. M. Markovic, *Nat. Mater.*, 2012, **11**, 550–557.

63 H. Liang, F. Meng, M. Cabán-Acevedo, L. Li, A. Forticaux, L. Xiu, Z. Wang and S. Jin, *Nano Lett.*, 2015, **15**, 1421–1427.

64 F. Song and X. Hu, *Nat. Commun.*, , DOI:10.1038/ncomms5477.

65 Z. Lu, H. Wang, D. Kong, K. Yan, P. C. Hsu, G. Zheng, H. Yao, Z. Liang, X. Sun and Y. Cui, *Nat. Commun.*, 2014, **5**, 1–7.

66 Y. R. Zheng, M. R. Gao, Q. Gao, H. H. Li, J. Xu, Z. Y. Wu and S. H. Yu, *Small*, 2015, **11**, 182–188.

67 X. Xu, F. Song and X. Hu, *Nat. Commun.*, 2016, **7**, 1–7.

68 D. Li, H. Baydoun, C. N. Verani and S. L. Brock, *J. Am. Chem. Soc.*, 2016, **138**, 4006–4009.

69 Y. Liu, H. Cheng, M. Lyu, S. Fan, Q. Liu, W. Zhang, Y. Zhi, C. Wang, C. Xiao, S. Wei, B. Ye and Y. Xie, *J. Am. Chem. Soc.*, 2014, **136**, 15670–15675.

70 L. Jiao, Y. X. Zhou and H. L. Jiang, *Chem. Sci.*, 2016, **7**, 1690–1695.

71 L. A. Stern, L. Feng, F. Song and X. Hu, *Energy Environ. Sci.*, 2015, **8**, 2347–2351.

72 P. Chen, K. Xu, Z. Fang, Y. Tong, J. Wu, X. Lu, X. Peng, H. Ding, C. Wu and Y. Xie, *Angew. Chemie*, 2015, **127**, 14923–14927.

73 C. Xia, Q. Jiang, C. Zhao, M. N. Hedhili and H. N. Alshareef, *Adv. Mater.*, 2016, **28**, 77–85.

74 Y. J. Wang, J. Qiao, R. Baker and J. Zhang, *Chem. Soc. Rev.*, 2013, **42**, 5768–5787.

75 G. Merle, M. Wessling and K. Nijmeijer, *J. Memb. Sci.*, 2011, **377**, 1–35.

76 A. Kulkarni, S. Siahrostami, A. Patel and J. K. Nørskov, *Chem. Rev.*, 2018, **118**, 2302–2312.

77 J. K. Nørskov, J. Rossmeisl, A. Logadottir, L. Lindqvist, J. R. Kitchin, T. Bligaard and H. Jónsson, *J. Phys. Chem. B*, 2004, **108**, 17886–17892.

78 M. Zhao, X. Wang, X. Yang, K. D. Gilroy, D. Qin and Y. Xia, *Adv. Mater.*, 2018, **30**, 1–17.

79 M. Zhou, H. Wang, A. O. Elnabawy, Z. D. Hood, M. Chi, P. Xiao, Y. Zhang, M. Mavrikakis and Y. Xia, *Chem. Mater.*, 2019, **31**, 1370–1380.

80 H. Zhang, M. Jin and Y. Xia, *Chem. Soc. Rev.*, 2012, **41**, 8035–8049.

81 X. Tian, J. Luo, H. Nan, H. Zou, R. Chen, T. Shu, X. Li, Y. Li, H. Song, S. Liao and R. R. Adzic, *J. Am. Chem. Soc.*, 2016, **138**, 1575–1583.

82 H. Lv, D. Li, D. Strmcnik, A. P. Paulikas, N. M. Markovic and V. R. Stamenkovic, *Nano Energy*, 2016, **29**, 149–165.

83 Y. Tong, P. Chen, T. Zhou, K. Xu, W. Chu, C. Wu and Y. Xie, *Angew. Chemie - Int. Ed.*, 2017, **56**, 7121–7125.

84 G. Wu, J. Wang, W. Ding, Y. Nie, L. Li, X. Qi, S. Chen and Z. Wei, *Angew. Chemie - Int. Ed.*, 2016, **55**, 1340–1344.

85 S. Dou, L. Tao, J. Huo, S. Wang and L. Dai, *Energy Environ. Sci.*, 2016, **9**, 1320–1326.

86 K. P. Singh, E. J. Bae and J. S. Yu, *J. Am. Chem. Soc.*, 2015, **137**, 3165–3168.

87 M. Xiao, J. Zhu, L. Feng, C. Liu and W. Xing, *Adv. Mater.*, 2015, **27**, 2521–2527.

88 J. Guo, Z. Mao, X. Yan, R. Su, P. Guan, B. Xu, X. Zhang, G. Qin and S. J. Pennycook, *Nano Energy*, 2016, **28**, 261–268.

89 X. L. Tian, L. Wang, B. Chi, Y. Xu, S. Zaman, K. Qi, H. Liu, S. Liao and B. Y. Xia, *ACS Catal.*, 2018, **8**, 8970–8975.

90 J. Luo, X. Tian, J. Zeng, Y. Li, H. Song and S. Liao, *ACS Catal.*, 2016, **6**, 6165–6174.

91 J. Ortiz-Medina, Z. Wang, R. Cruz-Silva, A. Morelos-Gomez, F. Wang, X. Yao, M. Terrones and M. Endo, *Adv. Mater.*, 2019, **31**, 1–16.

92 B. Y. Xia, Y. Yan, N. Li, H. Bin Wu, X. W. D. Lou and X. Wang, *Nat. Energy*, 2016, **1**, 1–8.

93 Z. Duan and G. Henkelman, *J. Phys. Chem. C*, 2020, **124**, 12016–12023.

94 S. K. Singh, K. Takeyasu and J. Nakamura, *Adv. Mater.*, 2019, **31**, 1–17.

95 L. Yang, X. Zeng, W. Wang and D. Cao, *Adv. Funct. Mater.*, 2018, **28**, 1–21.

96 K. H. Wu, D. W. Wang, D. S. Su and I. R. Gentle, *ChemSusChem*, 2015, **8**, 2772–2788.

97 S. Yang, J. Kim, Y. J. Tak, A. Soon and H. Lee, *Angew. Chemie - Int. Ed.*, 2016, **55**, 2058–2062.

98 Y. Chen, S. Ji, C. Chen, Q. Peng, D. Wang and Y. Li, *Joule*, 2018, **2**, 1242–1264.

99 Z. Yang, Y. Wang, M. Zhu, Z. Li, W. Chen, W. Wei, T. Yuan, Y. Qu, Q. Xu, C. Zhao, X. Wang, P. Li, Y. Li, Y. Wu and Y. Li, *ACS Catal.*, 2019, **9**, 2158–2163.

100 S. Wei, A. Li, J. C. Liu, Z. Li, W. Chen, Y. Gong, Q. Zhang, W. C. Cheong, Y. Wang, L. Zheng, H. Xiao, C. Chen, D. Wang, Q. Peng, L. Gu, X. Han, J. Li and Y. Li, *Nat. Nanotechnol.*, 2018, **13**, 856–861.

101 J. D. Yi, R. Xu, Q. Wu, T. Zhang, K. T. Zang, J. Luo, Y. L. Liang, Y. B. Huang and R. Cao, *ACS Energy Lett.*, 2018, **3**, 883–889.

102 Z. W. She, J. Kibsgaard, C. F. Dickens, I. Chorkendorff, J. K. Nørskov and T. F. Jaramillo, *Science*, , DOI:10.1126/science.aad4998.

103 L. Trotochaud, S. L. Young, J. K. Ranney and S. W. Boettcher, *J. Am. Chem. Soc.*, 2014, **136**, 6744–6753.

104 K. A. Stoerzinger, W. Seok Choi, H. Jeen, H. N. Lee and Y. Shao-Horn, *J. Phys. Chem. Lett.*, 2015, **6**, 487–492.

105 J. Wang and F. Ciucci, *Small*, 2017, **13**, 1–15.

106 Y. Zhu, S. Murali, W. Cai, X. Li, J. W. Suk, J. R. Potts and R. S. Ruoff, *Adv. Mater.*, 2010,

22, 3906–3924.

107 J. K. Zak, E. Negro, I. A. Rutkowska, B. Dembinska, V. Di Noto and P. J. Kulesza, *Encycl. Interfacial Chem. Surf. Sci. Electrochem.*, 2018, 651–659.

108 J. Luo, D. A. Vermaas, D. Bi, A. Hagfeldt, W. A. Smith and M. Grätzel, *Adv. Energy Mater.*, 2016, **6**, 1–7.

109 H. Fei, J. Dong, D. Chen, T. Hu, X. Duan, I. Shakir, Y. Huang and X. Duan, *Chem. Soc. Rev.*, 2019, **48**, 5207–5241.

110 J. Zhu, A. Holmen and D. Chen, *ChemCatChem*, 2013, **5**, 378–401.

111 F. Davodi, E. Mühlhausen, M. Tavakkoli, J. Sainio, H. Jiang, B. Gökce, G. Marzun and T. Kallio, *ACS Appl. Mater. Interfaces*, 2018, **10**, 31300–31311.

112 G. Valenti, A. Boni, M. Melchionna, M. Cargnello, L. Nasi, G. Bertoni, R. J. Gorte, M. Marcaccio, S. Rapino, M. Bonchio, P. Fornasiero, M. Prato and F. Paolucci, *Nat. Commun.*, 2016, **7**, 13549.

113 M. S. Dresselhaus and G. Dresselhaus, *Adv. Phys.*, 2002, **51**, 1–186.

114 G. C. Ri, C. J. Yu, J. S. Kim, S. N. Hong, U. G. Jong and M. H. Ri, *J. Power Sources*, 2016, **324**, 758–765.

115 R. Matsumoto and Y. Okabe, *Synth. Met.*, 2016, **212**, 62–68.

116 N. V. Maksimova, N. E. Sorokina, O. N. Shornikova and V. V. Avdeev, *J. Phys. Chem. Solids*, 2004, **65**, 177–180.

117 T. Rozmanowski and P. Krawczyk, *Electrochim. Acta*, 2019, **297**, 735–741.

118 L. Xiaomeng, W. Xuanjun and L. Xia, *Mater. Lett.*, 2017, **189**, 279–281.

119 J. M. Skowroński, P. Krawczyk, T. Rozmanowski and J. Urbaniak, *Energy Convers. Manag.*,

2008, **49**, 2440–2446.

120 J. Zhao, J. H. Dumont, U. Martinez, J. Macossay, K. Artyushkova, P. Atanassov and G. Gupta, *ACS Appl. Mater. Interfaces*, 2020, **12**, 42678–42685.

121 F. Beguin, R. Setton, F. Beguin, R. Setton, A. Hamwi and P. Touzain, *Mater. Sci. Eng.*, 1979, **40**, 167–173.

122 H. Schäfer-Stahl, D. Braga, A. Ripamonti, D. Savoia, C. Trombini and A. Umani-Ronchi, *J. Chem. Soc., Dalt. Trans.*, 1981, 328–330.

123 G. Wu, A. Santandreu, W. Kellogg, S. Gupta, O. Ogoke, H. Zhang, H. L. Wang and L. Dai, *Nano Energy*, 2016, **29**, 83–110.

124 K. B. Ibrahim, M. C. Tsai, S. A. Chala, M. K. Berihun, A. W. Kahsay, T. A. Berhe, W. N. Su and B. J. Hwang, *J. Chinese Chem. Soc.*, 2019, **66**, 829–865.

125 J. Yin, P. Zhou, L. An, L. Huang, C. Shao, J. Wang, H. Liu and P. Xi, *Nanoscale*, 2016, **8**, 1390–1400.

126 L. Han, X. Y. Yu and X. W. (David) Lou, *Adv. Mater.*, 2016, **28**, 4601–4605.

127 H. Shi and G. Zhao, *J. Phys. Chem. C*, 2014, **118**, 25939–25946.

128 A. Kumar and S. Bhattacharyya, *ACS Appl. Mater. Interfaces*, 2017, **9**, 41906–41915.

129 Q. Wang, K. Dastafkan and C. Zhao, *Curr. Opin. Electrochem.*, 2018, **10**, 16–23.

130 F. Moureaux, P. Stevens and M. Chatenet, *Electrocatalysis*, 2013, **4**, 123–133.

131 P. Li and H. C. Zeng, *Adv. Funct. Mater.*, , DOI:10.1002/adfm.201606325.

132 J. Guan, Z. Zhang, J. Ji, M. Dou and F. Wang, *ACS Appl. Mater. Interfaces*, 2017, **9**, 30662–30669.

133 T. Ma, C. Li, X. Chen, F. Cheng and J. Chen, *Inorg. Chem. Front.*, 2017, **4**, 1628–1633.

134 Y. Liang, Y. Li, H. Wang, J. Zhou, J. Wang, T. Regier and H. Dai, *Nat. Mater.*, 2011, **10**, 780–786.

135 J. J. Chen, J. B. Tan, C. F. Li, L. F. Gu, X. F. Lu and G. R. Li, *J. Phys. Chem. C*, 2020, **124**, 13036–13044.

136 S. Arumugam, Y. Toku and Y. Ju, *Sci. Rep.*, 2020, **10**, 1–11.

137 M. C. Biesinger, B. P. Payne, A. P. Grosvenor, L. W. M. Lau, A. R. Gerson and R. S. C. Smart, *Appl. Surf. Sci.*, 2011, **257**, 2717–2730.

138 W. Bian, Z. Yang, P. Strasser and R. Yang, *J. Power Sources*, 2014, **250**, 196–203.

139 X. He, F. Yin, S. Yuan, N. Liu and X. Huang, *ChemElectroChem*, 2016, **3**, 1107–1115.

140 Z. Chen, C. X. Kronawitter and B. E. Koel, *Phys. Chem. Chem. Phys.*, 2015, **17**, 29387–29393.

141 S. Liu, W. Bian, Z. Yang, J. Tian, C. Jin, M. Shen, Z. Zhou and R. Yang, *J. Mater. Chem. A*, 2014, **2**, 18012–18017.

142 W. Yan, Z. Yang, W. Bian and R. Yang, *Carbon*, 2015, **92**, 74–83.

143 Y. Zhao, R. Nakamura, K. Kamiya, S. Nakanishi and K. Hashimoto, *Nat. Commun.*, 2013, **4**, 2–8.

144 Z. Q. Liu, H. Cheng, N. Li, T. Y. Ma and Y. Z. Su, *Adv. Mater.*, 2016, **28**, 3777–3784.

145 Y. Liang, Y. Li, H. Wang, J. Zhou, J. Wang, T. Regier and H. Dai, *Nat. Mater.*, 2011, **10**, 780–786.

146 J. Wang, K. Li, H. Zhong, D. Xu, Z. Wang, Z. Jiang, Z. Wu and X. Zhang, *Angew. Chemie*, 2015, **127**, 10676–10680.

147 G. Zhang, B. Y. Xia, X. Wang and X. W. Lou, *Adv. Mater.*, 2014, **26**, 2408–2412.

148 X. Li, Y. Fang, X. Lin, M. Tian, X. An, Y. Fu, R. Li, J. Jin and J. Ma, *J. Mater. Chem. A*, 2015, **3**, 17392–17402.

149 S. Hirai, S. Yagi, A. Seno, M. Fujioka, T. Ohno and T. Matsuda, *RSC Adv.*, 2016, **6**, 2019–2023.

150 M. B. Chambers, X. Wang, N. Elgrishi, C. H. Hendon, A. Walsh, J. Bonnefoy, J. Canivet, E. A. Quadrelli, D. Farrusseng, C. Mellot-Draznieks and M. Fontecave, *ChemSusChem*, 2015, **8**, 603–608.

151 X. Wang and S. L. Buchwald, *J. Am. Chem. Soc.*, 2011, **133**, 19080–19083.

152 T. Harada, S. Ikeda, Y. H. Ng, T. Sakata, H. Mori, T. Torimoto and M. Matsumura, *Adv. Funct. Mater.*, 2008, **18**, 2190–2196.

153 W. Zhang, X. Zhang, L. Chen, J. Dai, Y. Ding, L. Ji, J. Zhao, M. Yan, F. Yang, C.-R. Chang and S. Guo, *ACS Catal.*, 2018, **8**, 8092–8099.

154 G. Valenti, A. Boni, M. Melchionna, M. Cargnello, L. Nasi, G. Bertoni, R. J. Gorte, M. Marcaccio, S. Rapino, M. Bonchio, P. Fornasiero, M. Prato and F. Paolucci, *Nat. Commun.*, 2016, **7**, 1–8.

155 M. Gao, W. Sheng, Z. Zhuang, Q. Fang, S. Gu, J. Jiang and Y. Yan, *J. Am. Chem. Soc.*, 2014, **136**, 7077–7084.

156 L. Zhuang, L. Ge, Y. Yang, M. Li, Y. Jia, X. Yao and Z. Zhu, *Adv. Mater.*, , DOI:10.1002/adma.201606793.

157 M. Gong, W. Zhou, M. C. Tsai, J. Zhou, M. Guan, M. C. Lin, B. Zhang, Y. Hu, D. Y. Wang, J. Yang, S. J. Pennycook, B. J. Hwang and H. Dai, *Nat. Commun.*, 2014, **5**, 1–6.

158 Y. Liu, G. Yu, G. D. Li, Y. Sun, T. Asefa, W. Chen and X. Zou, *Angew. Chemie - Int. Ed.*,

2015, **54**, 10752–10757.

159 J. Q. Chi, W. K. Gao, J. H. Lin, B. Dong, K. L. Yan, J. F. Qin, B. Liu, Y. M. Chai and C. G. Liu, *ChemSusChem*, 2018, **11**, 743–752.

160 D. Li, Z. Zong, Z. Tang, Z. Liu, S. Chen, Y. Tian and X. Wang, *ACS Sustain. Chem. Eng.*, 2018, **6**, 5105–5114.

161 P. Jiang, J. Chen, C. Wang, K. Yang, S. Gong, S. Liu, Z. Lin, M. Li, G. Xia, Y. Yang, J. Su and Q. Chen, *Adv. Mater.*, 2018, **30**, 1–10.

162 X. Chen, J. Zheng, X. Zhong, Y. Jin, G. Zhuang, X. Li, S. Deng and J. G. Wang, *Catal. Sci. Technol.*, 2017, **7**, 4964–4970.

163 Y. Xu, Y. Li, S. Yin, H. Yu, H. Xue, X. Li, H. Wang and L. Wang, *Nanotechnology*, , DOI:10.1088/1361-6528/aab6c1.

164 J. Yu, W. J. Li, H. Zhang, F. Zhou, R. Li, C. Y. Xu, L. Zhou, H. Zhong and J. Wang, *Nano Energy*, 2019, **57**, 222–229.

165 T. Ouyang, Y. Q. Ye, C. Y. Wu, K. Xiao and Z. Q. Liu, *Angew. Chemie - Int. Ed.*, 2019, **58**, 4923–4928.

166 D. Su, J. Wang, H. Jin, Y. Gong, M. Li, Z. Pang and Y. Wang, *J. Mater. Chem. A*, 2015, **3**, 11756–11761.

167 J. Zhu, L. Hu, P. Zhao, L. Y. S. Lee and K. Y. Wong, *Chem. Rev.*, 2020, **120**, 851–918.

168 R. Subbaraman, D. Tripkovic, D. Strmcnik, K. C. Chang, M. Uchimura, a P. Paulikas, V. Stamenkovic and N. M. Markovic, *Science*, 2011, **334**, 1256–1260.

169 P. Strasser, S. Koh, T. Anniyev, J. Greeley, K. More, C. Yu, Z. Liu, S. Kaya, D. Nordlund, H. Ogasawara, M. F. Toney and A. Nilsson, 2010, **2**, 454–460.

170 A. Sarkar and A. Manthiram, 2010, 4725–4732.

171 N. Balahmar, A. C. Mitchell and R. Mokaya, *Adv. Energy Mater.*, 2015, **5**, 1500867.

172 Y. Song, W. Chen, C. Zhao, S. Li, W. Wei and Y. Sun, *Angew. Chemie - Int. Ed.*, 2017, **56**, 10840–10844.

173 C. Zhu, H. Li, S. Fu, D. Du and Y. Lin, *Chem. Soc. Rev.*, 2016, **45**, 517–531.

174 W. Tian, H. Zhang, Z. Qian, T. Ouyang, H. Sun, J. Qin, M. O. Tadé and S. Wang, *Appl. Catal. B Environ.*, 2018, **225**, 76–83.

175 Q. Ren, H. Wang, X. F. Lu, Y. X. Tong and G. R. Li, *Adv. Sci.*, 2018, **5**, 1700515.

176 T. Ikeda, M. Boero, S. F. Huang, K. Terakura, M. Oshima and J. I. Ozaki, *J. Phys. Chem. C*, 2008, **112**, 14706–14709.

177 Y. Zheng, Y. Jiao, L. Ge, M. Jaroniec and S. Z. Qiao, *Angew. Chemie*, 2013, **125**, 3192–3198.

178 Y. Nie, L. Li and Z. Wei, *Chem. Soc. Rev.*, 2015, **44**, 2168–2201.

179 H. Liang, W. Wei, Z. Wu and X. Feng, *J. Am. Chem. Soc.*, 2013, **135**, 16002−16005.

180 F. Song, L. Bai, A. Moysiadou, S. Lee, C. Hu, L. Liardet and X. Hu, *J. Am. Chem. Soc.*, 2018, **140**, 7748–7759.

181 C. Wei, S. Sun, D. Mandler, X. Wang, S. Z. Qiao and Z. J. Xu, *Chem. Soc. Rev.*, 2019, **48**, 2518–2534.

182 M. Lukaszewski, M. Soszko and A. Czerwiński, *Int. J. Electrochem. Sci.*, 2016, **11**, 4442–4469.

183 H. Jin, C. Guo, X. Liu, J. Liu, A. Vasileff, Y. Jiao, Y. Zheng and S. Z. Qiao, *Chem. Rev.*, 2018, **118**, 6337–6408.

184 X. Ge, A. Sumboja, D. Wuu, T. An, B. Li, F. W. T. Goh, T. S. A. Hor, Y. Zong and Z. Liu,

ACS Catal., 2015, **5**, 4643–4667.

185 R. Zhou, Y. Zheng, M. Jaroniec and S. Z. Qiao, *ACS Catal.*, 2016, **6**, 4720–4728.

Acknowledgements

I would like to express my deepest gratitude to my supervisor Prof. Francesco Paolucci for giving me such a precious opportunity to study in his research group, for his very kind and beneficial guidance, for his continuous support, and for supplying an open and enjoyable research environment.

I would like to give my sincere gratitude to Dr. Giovanni Valenti. I very much appreciate his significant efforts in moving this project forward. I am grateful to him for teaching me a lot around laboratory, for very helpful discussions about the experiments, and for many times of correcting my reports, manuscripts, and thesis. I specially thank him for his understanding.

I would like to thank Dr. Ferdinand Hof and Prof. Alain Pénicaud from the University of Bordeaux, France. They supplied the materials for this project, and have been very supportive in manuscript submissions.

I would like to thank all the EMFM group members, Dr. Matteo lurlo, Dr. Alessandra Zanut (previous member), Miriam Moro, Sara Rebeccani, Jacopo Isopi, Prof. Massimo Marcaccio, Pavlos Nikolaou, for their very kind help not only for the research but also for my stay in Bologna. I would also like to thank master and bachelor students that I worked with during this period.

I would like to thank all the other colleagues, particularly guys from Prof. Stefania Rapino's research group. They made my stay more enjoyable.

I would like to thank Prof. Asefa at Rutgers University, USA for giving me a chance to visit his laboratory during my third year of PhD.

I would like to gratefully acknowledge the financial support from the China Scholarship Council (CSC) for my PhD study.

I would like to thank my family and friends for their love and encouragement.